Fall 2014

Structure and activity relationships of bimetallic catalysts for aqueous phase reforming and the water-gas shift reaction

Fred Gerald Sollberger
Purdue University

Graduate School Form 30
(Revised 08/14)

PURDUE UNIVERSITY
GRADUATE SCHOOL
Thesis/Dissertation Acceptance

This is to certify that the thesis/dissertation prepared

By Fred Gerald Sollberger

Entitled

STRUCTURE AND ACTIVITY RELATIONSHIPS OF BIMETALLIC CATALYSTS FOR AQUEOUS PHASE REFORMING AND THE WATER-GAS SHIFT REACTION

For the degree of Doctor of Philosophy

Is approved by the final examining committee:

Fabio H. Ribeiro

Jeffrey T. Miller

Jeffrey P. Greeley

Rajamani Gounder

To the best of my knowledge and as understood by the student in the Thesis/Dissertation Agreement, Publication Delay, and Certification/Disclaimer (Graduate School Form 32), this thesis/dissertation adheres to the provisions of Purdue University's "Policy on Integrity in Research" and the use of copyrighted material.

Fabio H. Ribeiro

Approved by Major Professor(s): _____

_____

Approved by: John Morgan 10/22/2014

Head of the Department Graduate Program Date

STRUCTURE AND ACTIVITY RELATIONSHIPS OF BIMETALLIC CATALYSTS FOR AQUEOUS PHASE REFORMING AND THE WATER-GAS SHIFT REACTION

A Dissertation

Submitted to the Faculty

of

Purdue University

by

Fred Gerald Sollberger

In Partial Fulfillment of the

Requirements for the Degree

of

Doctor of Philosophy

December 2014

Purdue University

West Lafayette, Indiana

Lord, help me to do great things as though they were little, since I do them with Your power; and little things as though they were great, since I do them in Your name.

—Blaise Pascal

ACKNOWLEDGEMENTS

I would like to take this space to thank the influential people key to keeping me on track these past few years. First, I would like to recognize my advisors Prof. Fabio Ribeiro and Prof. W. Nicholas Delgass for filling my knowledge base with conceptual understanding and experimental design expertise, and for training me to think about the world of catalysis and the wider world of science with a critical mind and a curious spirit. On a similar magnitude is the great guidance from Dr. Jeff Miller in gaining a working knowledge of all things XAS related, whether ex situ, in situ, or operando, both in the experimental design and data analysis aspects. Prof. Jeffrey Greeley likewise has been a great help with learning the possibilities of leveraging theoretical calculations to reach further and faster than experiments will sometimes allow us to go. I also thank Prof. Rajamani Gounder for kindly agreeing to give feedback and input through my defense committee.

I would next like to recognize the graduate students among whom I have shared a lot of learning time with. This would include especially Dr. Paul Dietrich, who taught me most of what I know about experimental rig building, equipment troubleshooting, and running an x-ray beamline at 3 am in the morning. Kaiwalya Sabnis and Dr. M. Cem Akatay have proved to be a wealth of help and ideas relating to the water-gas shift reaction and transmission electron microscopy, respectively. Of course I would also like to thank

those who persistently helped round-the-clock experiments to go as smoothly as possible at Argonne's APS facility: former and current Purdue graduate students Dr. Vincent Kispersky, Dr. Shane Bates, Atish Parekh; fellow IACT member Dr. Brandon O'Neill; beamline scientists Dr. Soma Chattopadhyay and Dr. Tomohiro Shibata.

Moving to the source of a lot of emotional support, I would like to recognize my circle of friends, and more importantly, my Brothers and Sisters in Christ from the Apostolic Christian Churches in Champaign, IL, and West Lafayette, IN. In particular, I am thankful for the loving support of Dick and Sharon Meister and the long evening conversations about history, society, religion, and the origin of the universe that I have enjoyed so much with Dick. Also, I am indebted to Fred and Libby Wahl who have done so much to make me feel welcome in West Lafayette from the time I was first looking for a place to live in Indiana. They have graciously opened their home, kitchen, and tennis court to me, and provided consistent support and friendship. Fred: you can stop calling me "Doctor Fred-to-be" now!

Finally, I would not miss the opportunity to thank the unwavering support of my family. To my mom Elaine, and my siblings Sam and Madeline, thank you for your enduring support even from a distance. You will not know just how much you have been a source of cheer and motivation through not just my academic career, but my entire life.

TABLE OF CONTENTS

Page

Page

LIST OF TABLES

Appendix Table Page

LIST OF FIGURES

Figure Page

Figure Page

Figure Page

Figure Page

Appendix Figure

Appendix Figure Page

ABSTRACT

Sollberger, Fred Gerald. Ph.D., Purdue University, December 2014. Structure and Activity Relationships of Bimetallic Catalysts for Aqueous Phase Reforming and the Water-Gas Shift Reaction. Major Professor: Fabio Ribeiro.

As the existing deposits of petroleum and non-renewable energy resources are exhausted, become more difficult to extract, and remain in politically unstable regions of the world, the search for long term alternatives for fuels and chemicals from renewable sources such as biomass continues. One promising process for the production of renewable hydrogen to use in conversion of biomass to fuels and chemicals is aqueous phase reforming (APR) of cellulose-derived carbohydrates.

In the first study Pt/MWCNT catalysts have been promoted by addition of transition metal promoters Cu, Ni, Co, Fe, Mn, Mo, W, and Re in Pt:M 1:1 atomic ratios to give up to 13 times higher glycerol reforming site time yield (STY) and 8 times higher water-gas shift (WGS) turnover rate (TOR). The bimetallic structure and oxidation state of the catalysts before and after reaction were determined by x-ray absorption spectroscopy (EXAFS and XANES spectra). While the fresh structure varied among the catalyst compositions, the used samples had similar preferences toward Pt-rich core, M-rich shell configurations, with some amount of oxidized M even after reduction in hydrogen at 450 °C. The measurement of the kinetic isotope effect (KIE) for replacement of water

with D_2O during glycerol APR determined that the rate determining step for APR is one which involves the O-H bond in water, not glycerol decomposition. In collaboration with Professor Jeffrey Greeley, water dissociation barriers were estimated by density function theory (DFT) calculations of OH binding energies on Pt_3M (111) surfaces. A volcano plot of WGS and APR reaction rates with OH binding energy was obtained. Additionally, DFT revealed that the more oxophillic metal promoters make use of separate sites for water dissociation that otherwise would require Pt sites that are used for glycerol decomposition. This dual site advantage was explicitly shown by DFT studies of OH on Pt_3M surfaces which already had CO adsorbed.

The second study shows that differences in rates and selectivity between two similar catalysts PtRe/MWCNT and PtRe/C can be explained in terms of metal distribution. Comparing the reduced catalyst EXAFS and XANES to those collected in operando, we find that PtRe/MWCNT contained larger alloyed particles which sinter slightly to 3.1 ± 1.1 nm during glycerol APR. The Re metal remains primarily reduced and the most prevalent surface adsorbates are CO and H for Pt and Re sites, respectively, during both WGS and APR reactions. For the smaller metal particles in PtRe/C (1.2 ± 0.3 nm), the Re oxidizes to form acid sites to open up dehydration/hydrogenation routes to [C-O] bond scission. Electron energy loss spectroscopy (EELS) maps confirm that while for individual particles Re remains well mixed with Pt in PtRe/MWCNT, the Re metal is well dispersed on the high surface area activated carbon support of PtRe/C, allowing easy oxidation under reaction conditions. In this case where high rates of hydrogen production by APR are desired, the PtRe/MWCNT catalyst was able to obtain higher STYs and

maintain higher [C-C] bond scission selectivity compared to PtRe/C due to the differences in metal distribution.

In a third study, various C3 alcohol molecules were compared in their reaction selectivity towards [C-O] and [C-C] bond scission over Pt/MWCNT. Glycerol, propylene glycol, and 1-propanol were found to have a high selectivity towards [C-C] scission, in agreement with relative bond scission barriers estimated by linear scaling relationships from DFT. However, 1,3-propanediol reacted through a pathway favoring [C-O] scission. Despite having different [C-C] and [C-O] bond scission selectivity, these different alcohols had similar reactant STYs, consistent with having a common rate determining step such as WGS.

CHAPTER 1. INTRODUCTION

1.1 Introduction

Today the consumption of fossil resources to produce fuels and chemicals remains politically and economically straining as societies strive to keep human environments clean and sustainable. Thus, research into finding processes for utilization of renewable feedstocks has remained a priority. As part of this effort within the U.S. Department of Energy's Energy Frontiers Research Centers (EFRC), the Institute for Atom Efficient Chemical Transformations (IACT) seeks to push the frontier of catalyst design and understanding in the area of biomass conversion. An integrated approach of catalyst synthesis, experimental testing, advanced characterization, and computational studies is used within IACT to accomplish this task. With experts in each area of expertise, it is increasingly evident that we can both create and understand novel catalytic systems that overcome past issues in catalyst activity, selectivity, stability, and cost. These materials were tested to improved the catalytic processes outlined in Figure 1.1, where carbohydrate molecules are converted to different platform chemical intermediates and finally into useful fuels and chemicals

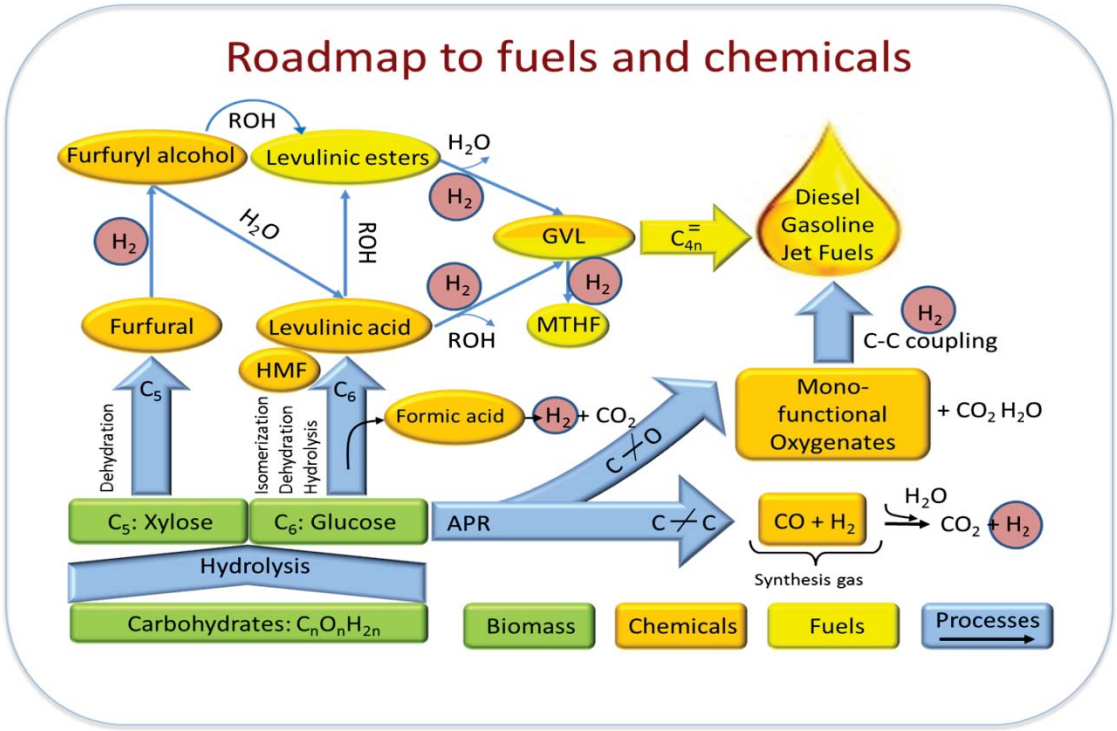

Figure 1.1 The Institute for Atom-Efficient Chemical Transformations' proposed catalytic pathway from biomass-derived sugars to fuels and chemicals.

In particular, this thesis has focused on using the tools of synthesis, kinetic testing, characterization, and computational studies to address the system of aqueous phase reforming (APR) over bimetallic catalysts. The main characterization technique employed was x-ray absorption spectroscopy, both *ex situ* and *operando* measurements. This was supplemented with scanning transmission electron microscopy (STEM) and electron energy loss spectroscopy (EELS) to compare the rates and selectivity from catalyst kinetics measurements to the catalyst structure.

1.2 Background Information and Previous Work

In the early 2000s it was discovered by Dumesic and coworkers that oxygenated hydrocarbons such as polyols, alcohols, and sugars can undergo reforming reactions over

supported noble metal catalysts in aqueous phase to yield hydrogen in high selectivity [1]. This aqueous phase reforming (APR), which is performed under high pressure (29-56 bar), and moderate temperatures (225°C-265°C) can be tuned by the catalyst composition, reaction conditions, and feed molecule to offer either hydrogen production by [C-C] bond scission, or short alkanes by [C-O] bond scission (Figure 1.2).

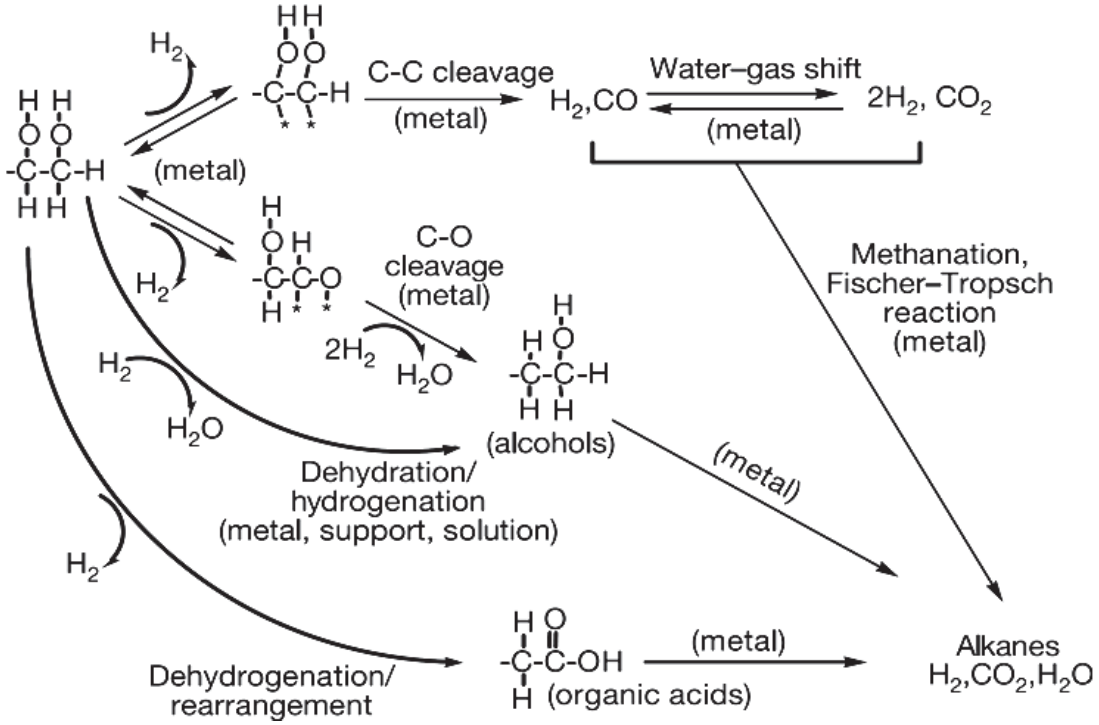

Figure 1.2 Generalized reaction scheme for aqueous phase reforming from [1]

Biomass reforming in the aqueous phase instead of the gas phase also offers several important advantages. Low or non-volatile biomass molecules like polyols and sugars may be used as feed molecules directly without first breaking the molecules down to smaller fragments which are more volatile. Second, it is possible to avoid most of the energy cost due to the large heat of vaporization of water by keeping the aqueous feed streams in the liquid phase under pressure. Third, the yield of hydrogen is enhanced and

the concentration of carbon monoxide is reduced by the large partial pressure of water which promotes the water-gas shift reaction during reforming. This last point is especially relevant in the case that this hydrogen is used in fuel cells, as these devices typically contain a platinum catalyst which is easily poisoned by small amounts of carbon monoxide at low operating temperatures [2]. Among metals which are active for the APR reaction, platinum has been found to be the best monometallic catalyst, as it promotes [C-C] bond scission over [C-O] bond scission to give high hydrogen selectivity (Figure 1.3).

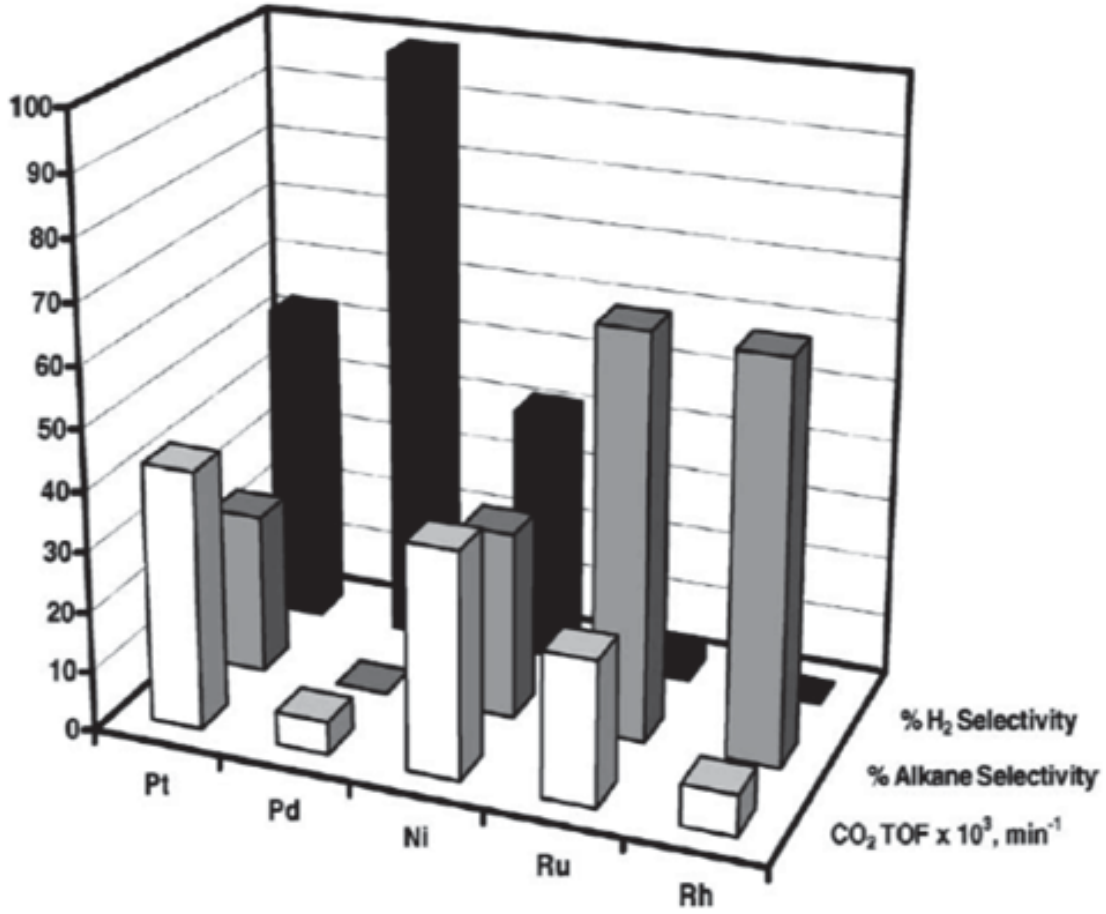

Figure 1.3 Comparison of selectivity and rates for metals active for aqueous phase reforming, as published in [3].

In a paper by Davda, et al. platinum and nickel were both found to have the highest activity, but nickel suffered from lower selectivity to hydrogen versus the production of monofunctional alcohols and alkanes [3]. As a base metal which can leach in hot water, nickel also displayed low stability under aqueous phase reforming conditions. A wide range of support materials have also been tested and it was found that adequate activity and stability are achieved in particular for platinum supported on γ-alumina and platinum supported on carbon [4]. Even so, γ-alumina has been shown to undergo transformation to a boehmite (AlOOH) phase via hydration of surface sites, yielding a support with diminished acidity and much smaller surface area [5]. The presence of supported metal particles such as platinum and nickel may actually help slow this transition on γ-alumina [5]. Carbon supports have thus been favored for platinum aqueous phase reforming catalysts most recently, as an inert and stable material.

Adding a second metal to platinum for the reforming catalysts has been shown to improve the reaction rate, although in many cases at the cost of a small decrease in hydrogen selectivity. It has been suggested that this increased activity may be due to the ability of alloying to reduce the binding energy of carbon monoxide to the platinum metal sites. For example in the case of platinum-rhenium, a Pt-Re(1:1)/C catalyst was measured by microcalorimetry to have a CO heat of adsorption of roughly 10 kJ/mol less than the monometallic Pt/C over a range of low to moderate CO surface coverages [6]. Lowering the CO binding energy should lead to less blocking of surface sites by reaction intermediates or products [6]. Another reason for promotional effects of a second metal is the promotion of the water-gas shift reaction rate. An example of this is the promotion of palladium on alumina catalysts with iron. It was found by Huber,et al. that due to the

promotion of WGS on iron oxide, palladium-iron on alumina yielded hydrogen turnover rates of 39-46 times that of unpromoted palladium on alumina [2]. Dumesic and coworkers have used a high-throughput reactor to screen over 70 bimetallic platinum and palladium catalysts [2]. While platinum-rhenium on carbon was found to be best bimetallic catalyst in terms of reaction rate and stability, other bimetallics that have worked well include platinum-nickel, platinum-cobalt, palladium-iron, tin-modified Raney nickel, and current work in our laboratory using platinum-molybdenum [2, 6-8].

1.3 Thesis Overview

In Chapter 2 of this thesis a series of PtM(1:1)/MWCNT (M = Mn, Fe, Co, Ni, Cu, Mo, W, Re) catalysts were tested for aqueous phase reforming (APR) of glycerol and the gas phase water-gas shift (WGS) reaction. A correlation between rates of these two reactions was observed, which is supported by experimental evidence of the kinetic isotope effect (KIE). Density functional theory (DFT) calculations of OH binding energy on the bimetallic Pt_3M (111) surface related to the step of water dissociation on new sites created with the addition of the promoter metal. Volcano plots for the rates of both reactions versus OH binding energy indicate that there are different optimum values of this descriptor for WGS versus APR. The bimetallic structure of the catalysts before and after APR was determined by x-ray absorption spectroscopy (both XANES and EXAFS), and indicated that under the oxidizing environment of hot liquid water the promoter metals tend to segregate and oxidize at the surface, but remain coordinated to Pt. This dual site feature of PtM/MWCNT catalysts allows facile water dissociation for the promotion of water-gas shift reaction, which enhances APR rates by reacting with surface CO created during the reforming reaction.

Another study which is part of this thesis (Chapter 3) is the investigation of how the aqueous phase reforming site-time yields (STYs) were found to be higher and selectivity of [C-O]/[C-C] bond scission products were found to be lower for PtRe bimetallic catalysts prepared on multiwalled carbon nanotubes as compared to PtRe on activated carbon. *Operando* x-ray absorption spectroscopy (XAS) of both catalysts was performed to determine the metal particle structure and oxidation state of the working catalyst, as well as the most important surface adsorbates on Pt and Re metal sites. Together with information from electron energy loss spectroscopy (EELS) elemental maps of the metal distribution on each used catalyst, it was found that Re which remained alloyed with Pt during reaction (as in PtRe/MWCNT) remained reduced and was able to work with Pt in a dual site mechanism for promoting the rates of glycerol APR and WGS reactions. In contrast, Re which is well dispersed on the support (as in PtRe/C) will partially oxidize during reaction and contribute to limiting the promotion of glycerol STY and decreasing the hydrogen selectivity by introducing new [C-O] bond scission reaction routes.

The third investigation of this thesis (Chapter 4) is a kinetic and computational study of the effect of different alcohol group positions and how this affects the [C-C] and [C-O] bond scission selectivity. Linear scaling relationship calculations are used to estimate the relative reaction barriers to bond scission for the alcohols under investigation: 1,2-propanediol, 1,3-propanediol, and 1-propanol. While there is good agreement between experimental results and calculations that both 1,2-propanediol and 1-propanol have a preference towards the [C-C] bond scission pathway, 1,3-propanediol prefers [C-O] bond scission, in disagreement with calculations. Another result from this set of experiments is that the rates for aqueous phase reforming of different C3 alcohols is very similar,

indicating that there may be a common rate determining step for all three. This includes the possibility of a slow initial dehydrogenation step, or the water-gas shift reaction which is needed to clean surface sites of adsorbed CO.

CHAPTER 2. SPECTROSCOPIC AND KINETIC STUDY OF THE ACTIVE SITE FOR PLATINUM BIMETALLIC CATALYSTS FOR AQUEOUS PHASE REFORMING AND THE WATER-GAS SHIFT REACTION

2.1 Introduction

As the existing deposits of petroleum and non-renewable energy resources are exhausted, become more difficult to extract, and remain in politically unstable regions of the world, there continues to be a search for long term alternatives for fuels and chemicals from renewable sources such as biomass. Many processes such as catalytic hydrodeoxygenation which are used to decrease the high oxygen content of biomolecules to yield useful chemicals require a renewable source of hydrogen. One such process for the production of renewable hydrogen is aqueous phase reforming (APR) of sugar and sugar alcohols over noble metal catalysts as developed by the group of Dumesic and coworkers [1]. In subsequent work it was discovered that rates of APR could be increased by addition of a second transition metal as a promoter [2]. The nature of the promotional effect on the selectivity and rates of platinum catalysts have recently been investigated by our group using *operando* x-ray absorption spectroscopy (XAS), calculations from density functional theory, and scanning transmission electron microscopy with electron energy loss spectroscopy [9]. These efforts determined that there are differences in the preferred alloy structure, the distribution of mixed alloy and core-shell particles, and the oxidation state of the promoter metal. Each of these

components can affect the selectivity of Pt towards C-C bond scission in favor of hydrogen production or C-O bond scission in favor of alkane production and monofunctional organic compounds.

Descriptors for the selectivity of different bimetallic catalyst compositions have been suggested in previous work in the literature, such as oxygen binding energy and deprotonation energy from density functional theory (DFT) calculations [10]. Additionally, experiments have focused on broad surveys of prospective metals for active and selective polyols reforming [3], support materials which optimize the rates and stability of the catalyst in hot aqueous environments [11], and promoter metals which can enhance the reforming rates of Pt and Pd monometallic catalysts by alloy formation [2]. The fields of computational chemistry and electrocatalysis have also focused much attention to the theoretical prediction and spectroscopic characterization of bimetallic Pt alloys to determine the preferred metal nanoparticle structure. Density functional theory has been used to calculate the segregation energies for a wide range of both extended surfaces [12] and small nanoparticles [13] in order to predict core-shell preferences in vacuum with both metals in the fully reduced state. In addition, there have been DFT studies to assess the effect of adsorbed H and CO species on the stability of alloy structures, particularly near-surface alloys (NSA) which are important for fuel cell applications to minimize the use of precious metals [14]. *In situ* x-ray absorption studies of Pt alloy electrocatalysts have been performed at ambient temperature as well, in order to determine the bimetallic structure for several Pt_3M/C compositions during operation of fuel cell electrodes [15].

The current work seeks to use the reactions water-gas shift and aqueous phase reforming of glycerol along with characterization by XAS (both near edge structure and extended fine structure), transmission electron microscopy (TEM), and reaction kinetics, and kinetic isotope effects (KIE) to reach conclusions about the promotional effect of secondary metals added to Pt/MWCNT catalysts and the nature of the active site for each reaction. These conclusions are enhanced through the use of DFT calculations to provide binding energies and preferred binding sites of key surface species common to water-gas shift and reforming reactions on Pt_3M (111) extended surfaces, namely OH and CO adsorbates.

2.2 Experimental

2.2.1 Catalyst Synthesis

A series of monometallic and bimetallic platinum catalysts were prepared on multiwalled carbon nanotubes (MWCNT purchased from Cheaptubes, Inc.) as a support. Platinum was first added by incipient wetness impregnation of as-received MWCNT with an aqueous solution of tetraammineplatinum(II) nitrate (Sigma-Aldrich) in order to give 5 wt% Pt loading. After drying overnight in air at 60 °C, the samples were further impregnated with an aqueous solution of one of the following salts: manganese nitrate, iron nitrate nonahydrate, cobalt nitrate hexahydrate, nickel nitrate hydrate, copper nitrate hydrate, ammonium heptamolybdate, ammonium tungstate, ammonium perhennate. After this second impregnation the samples were dried overnight in air at 150 °C, along with the monometallic 5 wt% Pt/MWCNT sample.

2.2.2 Aqueous phase reforming reaction kinetics

Aqueous phase reforming of glycerol was carried out by loading 30 to 150 mg of catalyst into a 10 mm × 6 mm × 200 mm (OD×ID×L) quartz tube (Chemglass, Inc.) or 10 mm × 4 mm × 200 mm (OD×ID×L) Sigradur glassy carbon tube (Hochtemperatur-Werkstoffe), secured by plugs of quartz wool and stainless steel rod spacers. The temperature of the reactor was controlled by inserting a K-type thermocouple (Omega) into the top of the catalyst bed. The reactor was heated by a custom aluminum heater block with cartridge heaters [16]. Each catalyst was reduced *in situ* in 50 sccm of a 5 % H_2/Ar gas mixture at 450 °C (or 400 °C for Pt/MWCNT) with a 2 hour ramp, 2 hour dwell prior to the reforming reaction. Following cooling of the reactor to room temperature, the 10 or 30 wt% aqueous glycerol (Sigma-Aldrich) solution was pumped in an up-flow configuration by a dual syringe pump system (Teledyne ISCO) or HPLC pump (Chrom Tech) until the system was full of liquid. Then the system was pressurized from the downstream section by Ar sweep gas to 32 bar, utilizing a biphasic backpressure regulator (Equilibar), and the reactor temperature was ramped to 230 °C over a period of 2 hours. The weight hourly space velocity (WHSV, g glycerol g cat^{-1} h^{-1}) was varied over a range of 0.05 to 5 h^{-1} by changing the pump rate in order to obtain selectivity versus conversion results. For initial rate measurements the amount of catalyst was 30 mg and the pump rate was kept at 0.30 mL/min for 30 wt% aqueous glycerol in order to maintain glycerol conversion of less than 5%.

Product analysis of the gases was obtained by an online gas chromatograph (Agilent 7890) with a Carboxen 1000 packed column and He (for gas phase carbon species) or N_2 (for improved resolution of the hydrogen peak) carrier gases. Argon sweep gas was used to

flush the line into the gas/liquid phase separator and as an internal standard for the gas products (H_2, CO, CO_2, CH_4, and C_2H_6). Liquid samples were drained from the phase separator at regular intervals and analyzed by the same gas chromatograph using a DB-WAX capillary column. Diethylene glycol was added to each liquid sample for use as an internal standard

Site time yield (STY) was used to define the normalized rate per surface site as counted by CO chemisorption. This convention is used instead of the turnover rate (TOR) due to the fact that data, while taken at low conversions, was not differential since products were not co-fed into the reactor. Also, the reaction consists of many parallel and series reactions happening simultaneously such that glycerol STY was used as the standard rate comparison. Carbon selectivity calculations are defined for products or product groupings as $(\Sigma(\mathrm{r}_{\mathrm{product}} \times \mathrm{carbon\ number}))/(\mathrm{r}_{\mathrm{glycerol}} \times 3) \times 100\%$. The product groupings are [C-C] scission products (ethylene glycol and methanol), [C-O] scission products (acetaldehyde, propionaldehyde, acetone, 2-propanol, ethanol, 1-propanol, hydroxyacetone, propylene glycol, and 1,3-propanediol), and acid products (acetic acid and propionic acid). Hydrogen selectivity is quantified as the fraction of H_2 which was in the product gas over the total H2 which would have been possibly produced if the both methane and ethane were instead fully reformed to CO_2 and H_2, as defined as $(\mathrm{r}_{\mathrm{H}_2})/(\mathrm{r}_{\mathrm{H}_2} + 4 \times \mathrm{r}_{\mathrm{CH}_4} + 7 \times \mathrm{r}_{\mathrm{C}_2\mathrm{H}_6}) \times 100\%$.

2.2.3 Water-gas shift kinetics

Water-gas shift kinetics were collected in a system of four parallel fixed bed reactors as described elsewhere [17]. Products were co-fed and CO conversion was maintained below 10 percent to give differential conditions. By changing the gas feed concentrations

and reaction temperature, the apparent reaction orders and apparent activation energies of all catalyst samples were obtained.

2.2.4 Catalyst Characterization

2.2.4.1 X-ray absorption spectroscopy

X-ray absorption spectra of samples were obtained at Argonne National Laboratory's Advanced Photon Source on the Materials Research Collaborative Access Team (MRCAT) Sector 10 insertion device or bending magnet beamlines. Experiments were conducted at the Pt L_{III} or L_{II} (for PtW sample, due to overlap of the W L_{II} and Pt L_{III} edge, see Figure A.1) and at the promoter K (Mn, Fe, Co, Ni, Cu, Mo) or L_{III} (Re, W) edges. All experiments were conducted in transmission in quick scan mode. Reference metal foils for energy calibration were captured simultaneously with every scan with a third detector in series. The x-ray beam was 1000 × 1000 μm.

The catalysts were pressed into 4 mm diameter self-supporting pellets within a six well sample holder, which was then placed into an *in situ* reactor consisting of a 1 inch quartz tube with an Ultra-Torr fitting with Kapton window and a shutoff valve on each end to allow for a controlled gas atmosphere. Bimetallic samples were reduced in 3.5 % H_2/He for 30 minutes at 450 °C (or 400 °C for Pt/MWCNT), purged with He, and cooled to room temperature before scanning. These reduced samples are referred to as 'fresh' samples, and samples which have been used for APR and then re-reduced under the same conditions are referred to as 'used' in the remainder of this study. Scans of reference materials were diluted with silica and scanned in air at room temperature. Sample loadings were calculated to give a total absorption (μx) above the edge of ~2.0.

The x-ray absorption spectra of each sample were analyzed by WinXAS 3.1 software following standard procedures for energy calibration to the experimental metal foil and background subtraction. K-edge XANES spectra were fit for Cu, Ni, Co, and Fe from -10 eV to +30 eV as a least squares linear combination of metal foil and oxide standards. The EXAFS of each fresh and used catalyst sample were fit using the k^2-weighted Fourier transform (FT) EXAFS spectra from k of 2.7 to 11.5 $Å^{-1}$ of both element edges simultaneously. Experimental foil spectra were used for Pt-Pt and M-M scatters, whereas theoretical Pt-M scatters were calculated using FEFF6 software. The M-O scatter was isolated from the acetylacetonate salts of Cu, Ni, Co, Fe, Mn; and the compounds sodium molybdate, ammonium perrhenate, and sodium tungstate were used for Mo, Re, and W, respectively.

2.2.4.2 Transmission electron microscopy

Several catalyst particles were suspended in ethanol by ultrasonic bath for approximately 5 minutes. Afterward the suspension was pipetted onto a copper TEM grid (200 mesh) with lacey carbon film. Images were acquired on an FEI Titan microscope at an operating voltage of 300kV and a Gatan Imaging Filter (GIF). A CCD camera (2048 × 2048 pixel) was used to capture the images, and they were stored via the Gatan Digital Micrograph software. ImageJ software was used to determine particle size distributions using at least 350 particles for each used catalyst sample.

2.2.4.3 Chemisorption

Hydrogen and carbon monoxide chemisorption measurements were performed on the fresh catalyst samples by first reducing the sample in pure hydrogen at 450 °C, and then

obtaining initial and repeat isotherms of adsorbed gas at 35 °C between the pressure ranges of 150 and 450 Torr. Within the linear range of each sample's isotherms, the difference was taken and extrapolated to zero pressure to obtain the H/Pt or CO/Pt ratio for the sample. Dispersion was calculated assuming a 1:1 stoichiometry of both H and CO to surface Pt atoms. Due to problems with outgassing after removal from the glycerol solution, chemisorption was not performed on the used samples.

2.2.4.4 Density functional theory calculations

DFT calculations were performed using periodic, plane wave based Vienna Ab initio Simulation Package (VASP). Gradient corrected PW-91 functional was used for exchange correlation energy. The bimetallic alloys were assumed to have composition Pt_3M, M being the alloying material and all calculations were performed on the fcc 111 surface of the alloys using 2×2 unit cells and slab thickness of 4 layers. Lattice constants of the alloys were computed using DFT. Vacuum layer between surface slabs was fixed at 16 Å. A Monkhorst Pack sampling scheme with 4×4×1 K-point set was used in all the calculations. Energy cutoff was fixed at 400 eV. Dipole corrections were introduced in z directions for all calculations. Spin polarized calculations were performed for Ni, Co, Fe and Mn. Methfessel Paxton smearing of 0.1 eV was used for calculations on slabs and Gaussian smearing of 0.01 eV was used for gas phase calculations. Gas phase calculations were performed in 13×14×15 Å unit cells. Convergence criterion for self-consistent iterations was set to 1×10^{-4}, while that for ionic steps was 0.02 eV/Å. The parameter values were chosen after carrying out convergence tests. OH binding energy

was computed with reference to gas phase water dissociation according to the following equation.

$$BE_{OH^*} = E_{OH*} - E_* + 0.5E_{H_2(g)} - E_{H_2O(g)}$$

BE_{OH*} = Binding energy of OH

E_{OH*} +surface = Energy of surface with OH adsorbed

$E_{surface}$ = Energy of clean surface

$E_{H2(g)}$ = Energy of gas phase hydrogen

$E_{H2O(g)}$ = Energy of gas phase water

Initial placement of OH was on 9 different surface sites illustrated in Figure A.2. Lower values of BE_{OH*} correspond to stronger OH binding.

2.3 Results

2.3.1 Aqueous phase reforming

All bimetallic samples except PtCu displayed significant rate promotion over monometallic Pt when normalized to surface sites by CO chemisorption as reported in Table 1. The largest glycerol STY was obtained by PtRe/MWCNT (~13 times higher than Pt), and this alloy has been the focus of a number of catalyst studies in the recent APR literature [18-22]. The hydrogen selectivity of this catalyst suffers compared to Pt and bimetallic PtM with 3d promoter metals, however. This is due to the higher selectivity to C-O bond scission (54 %), which is responsible for consuming hydrogen and leading to alkanes and liquid products with saturated hydrocarbon fragments which are less reactive than glycerol towards the reforming reaction. The three catalyst compositions which have hydrogen selectivity significantly lower than Pt/MWCNT were PtMo, PtRe, and PtW. These alloys have previously been identified as catalysts for C-O

hydrogenolysis of oxygenates, due to the low deprotonation energies on the promoter/secondary metal which generates Brønsted acidity [23]. They correspondingly have the highest ratio of 1,3-propanediol to 1,2-propanediol in the liquid products, a measure of acidic dehydration compared to metal catalyzed C-O hydrogenolysis [10].

Table 2.1 Kinetics and product selectivities for Pt monometallic and bimetallic catalysts used for aqueous phase reforming of glycerol. Data obtained at 230 °C, 32 bar total pressure, 30 wt% glycerol feed, and 0.30 mL/min liquid flow rate.

Catalyst	**Pt**	**PtCu**	**PtNi**	**PtCo**	**PtFe**	**PtMn**	**PtMo**	**PtRe**	**PtW**
Glycerol STY /10^{-2} mol mol^{-1} s^{-1}	4.8	3.3	11.0	18.7	25.8	21.9	28.8	60.4	8.3
Glycerol (STY_{PtM}/ STY_{Pt})	1.0	0.7	2.3	3.9	5.4	4.6	6.1	12.7	1.7
Carbon Conversion	0.5%	0.3%	1.0%	4.9%	1.3%	1.6%	1.8%	12.1%	0.7%
CO_2/alkanes	21.6	36.9	102.9	23.7	20.1	20.5	7.7	8.0	9.6
H_2/CO_2	2.3	3.6	2.2	2.1	2.2	2.4	1.1	1.1	2.4
H_2 Selectivity	93%	97%	98%	93%	92%	93%	71%	72%	86%
[1,3-PDO]/[1,2-PDO]	0.13	0.00	0.07	0.02	0.06	0.08	0.14	0.18	0.28
[C-C]/[C-O] scission	0.54	0.13	1.30	0.29	0.44	0.59	0.17	0.26	0.48
Product selectivity									
[C-O] scission	30%	72%	27%	33%	32%	25%	64%	54%	31%
[C-C] scission	16%	9%	35%	10%	14%	15%	11%	14%	15%
Acids	0%	0%	0%	0%	0%	0%	0%	1%	0%
CO	0%	0%	0%	0%	0%	0%	0%	0%	0%
CO_2	52%	18%	38%	54%	51%	58%	22%	28%	49%
CH_4	1%	0%	0%	2%	1%	2%	1%	1%	3%
C_2H_6	1%	0%	0%	1%	1%	1%	1%	1%	2%

All of the catalysts except PtMn/MWCNT displayed deactivation over time periods of greater than 5 days on stream in Figure 2.1. The two most oxophillic metal promoters corresponded to the quickest deactivation (PtMo and PtW). Unlike the other catalysts PtMn/MWCNT continued to increase in activity even 8 days after starting the reaction, up to 69 % higher than the initial STY. This is also the catalyst which lost the most

secondary metal to leaching in the aqueous environment, and was initially all MnO_x as seen in the XANES and EXAFS data presented later.

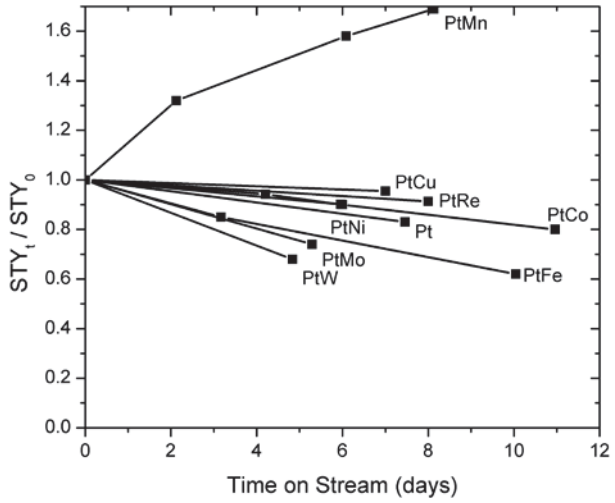

Figure 2.1 Deactivation for each catalyst displayed as a fraction of the initial STY during at least 5 days time-on-stream. Data obtained at 230 °C, 32 bar total pressure, 10 wt% glycerol feed, and 0.30 mL/min liquid flow rate.

2.3.2 Kinetic isotope effect (KIE)

To establish that water dissociation is involved in the rate determining step of aqueous phase reforming, one experiment was performed using D_2O as a solvent instead of water to observe any kinetic isotope effect on the rate of glycerol reforming over PtCo/MWCNT. When the pump feed was switched from 30 wt% glycerol to the glycerol/D_2O feed at an equivalent molarity, the glycerol STY dropped from 1.94×10^{-1} s^{-1} down to 1.15×10^{-1} s^{-1}. Afterward the feed was switched back to the 30 wt% glycerol fed and the rate returned to 2.00×10^{-1} s^{-1}. This yields a KIE equal to 1.7.

2.3.3 Water-gas shift kinetics

Complete water-gas shift kinetics for all catalysts obtained by the plug flow reactors under differential conditions are displayed in Table 2. It can be seen that all catalysts

except PtCu, PtW, and PtNi achieved at least a twofold increase in turnover rates compared to monometallic Pt. A consistent trend in the WGS kinetics parameters was a decrease in the apparent activation energy with increasing CO order (see Figure A.3). This is indicative of a common rate determining step for the series of similar catalysts which affects the surface coverage of CO.

Table 2.2 Water-gas shift kinetic parameters. Turnover rates were interpolated to 300 °C with standard gas feed composition of 6.8% CO, 21.9% H_2O, 8.5% CO_2, 37.4% H_2 and balance Ar.

			Apparent Reaction Order				TOR at 300°C / 10^{-2} s^{-1}
Catalyst	**$E_{a,\ app.}$ (kJ mol^{-1})**	**Temp (°C)**	**H_2O**	**CO_2**	**CO**	**H_2**	
5% Pt/MWCNT	81.6	300	0.76	-0.06	0.12	-0.44	3.2
5% Pt, 1.4% Mn/MWCNT	93.7	280	1.01	-0.10	0.01	-0.43	8.5
5% Pt, 1.4% Fe/MWCNT	79.5	300	0.67	-0.27	0.25	-0.58	6.9
5% Pt, 1.5% Co/MWCNT	95.6	275	0.90	-0.11	-0.01	-0.47	7.8
5% Pt, 1.5% Ni/MWCNT	113.3	300	1.54	-0.06	-0.12	-0.54	3.6
5% Pt, 1.6% Cu/MWCNT	93.2	300	0.76	-0.12	0.08	-0.37	2.5
5% Pt, 2.5% Mo/MWCNT	60.0	250	0.63	0.03	0.24	-0.23	26.8
5% Pt, 4.7% W/MWCNT	73.4	300	0.99	-0.18	0.20	-0.41	3.0
5% Pt, 4.8% Re/MWCNT	99.6	240	0.87	-0.07	-0.15	-0.48	17.9

2.4 Characterization

2.4.1 XANES

The near edge spectra for the metal promoter (K or L_{III} edge) in Figure 2.2 are accompanied by reference foil, oxide, and carbide spectra. For Cu, Ni, and Co the edge shape and white line intensity of the fresh catalysts is very close to that of the foil, indicating qualitatively that a majority of the metal has been reduced to the zero valent state. After being used in the reforming reaction and subsequently re-reduced, the white line intensity increased and the shape moved closer to a combination of foil and oxide

references. Linear combination least squares fitting of fresh and used samples (Table S.1) indicates a general increase in the fraction of oxide in the used samples compared to the fresh. Also, the percentage of reduced metal for the fresh catalysts decreases from Cu as the most reducible metal (98 %) to Co and Fe as the least reducible metals (86 %) among these four catalysts.

XANES analyses of the other promoter metals, which have multiple common oxidation states and possible carbide phases (W, Mo), are not as quantitative. For fresh PtMn/MWCNT, the shape of the edge is nearly identical to MnO, which indicates primarily Mn^{2+}. In contrast, the white line intensity and pre-edge feature of the used sample are closer to those of the foil spectra. This partially reduced metal is consistent with the evidence of alloyed Mn observed in the EXAFS. The fresh and used PtMo/MWCNT have edge positions between Mo foil and MoO_2, such that the average Mo oxidation state is between 0 and +4, but this may contain some contribution from Mo_2C which has an edge shape and position similar to the samples. The W L_{III} edge is similar, with fresh and used spectra between WO2 and WO3 (oxidation 4+ and 6+), with a possibility of WC contribution. The Re L_{III} edge spectra for PtRe/MWCNT fresh and used samples are of a shape and edge position between Re foil and ReO_2, such that the average oxidation state is between 0 and +4 both before and after APR.

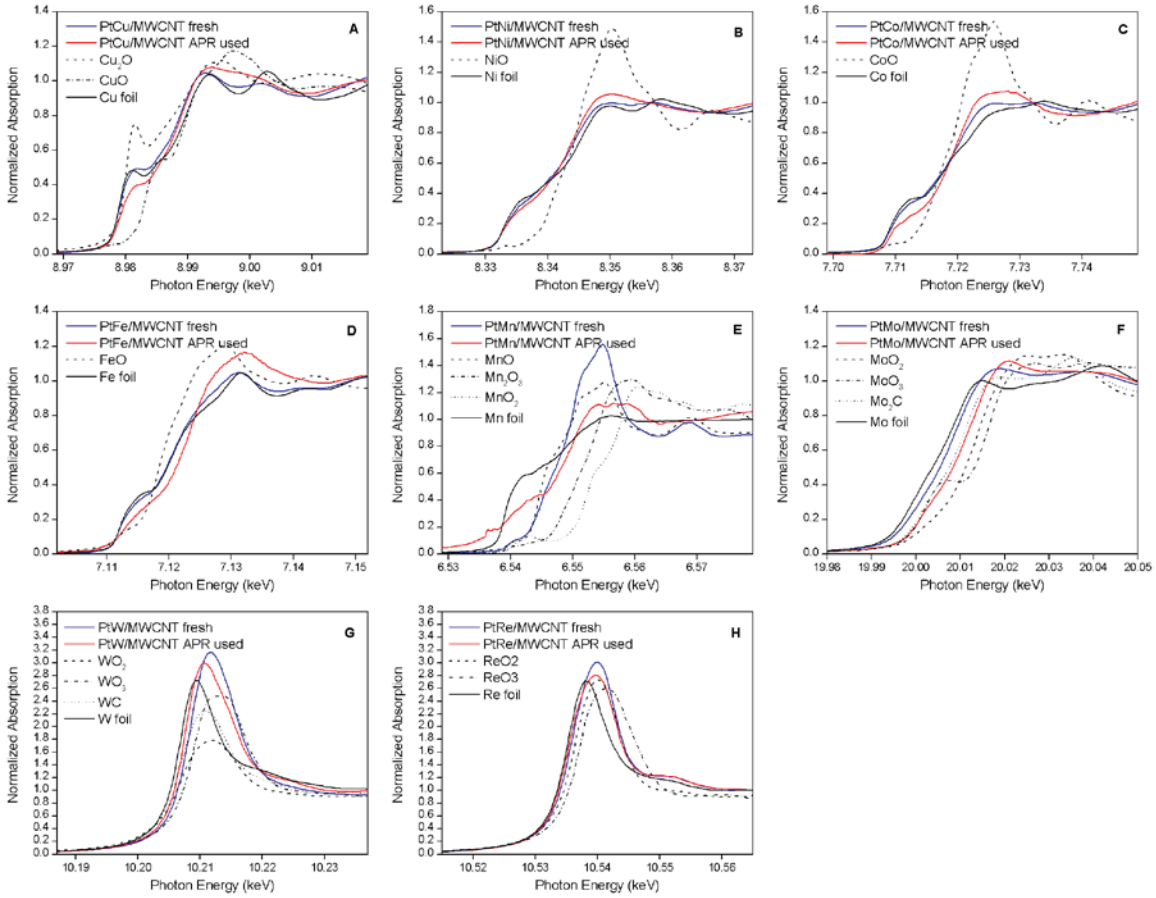

Figure 2.2 XANES spectra of the M K (or L_{III} for W and Re) edge of the reduced bimetallic catalysts before (blue) and after (red) reaction as compared to reference Pt foil (black, solid) and any relevant bulk oxide and carbide references. Edge positions of all spectra are shown in Table S.2.

The corresponding Pt L_{III} edge spectrum for each catalyst in Figure 2.3 indicates that the Pt is always in a reduced state, but there is a small shift in edge position and whiteline intensity of varying degrees due to the electron sharing with the alloying metal [24-26]. Several catalysts were found to leach some amount of promoter metal under the hot aqueous conditions of the reaction environment according to atomic absorption spectroscopy measurements of the liquid effluent and a decrease in the relative edge step for common sample loading of for XAS measurements (Figure A.1). It is these metals

(Ni, Co, Fe, Mn, W) for which the used catalyst spectra is closer to the Pt foil than the fresh catalyst spectra, due to the loss of alloy from metals leaching.

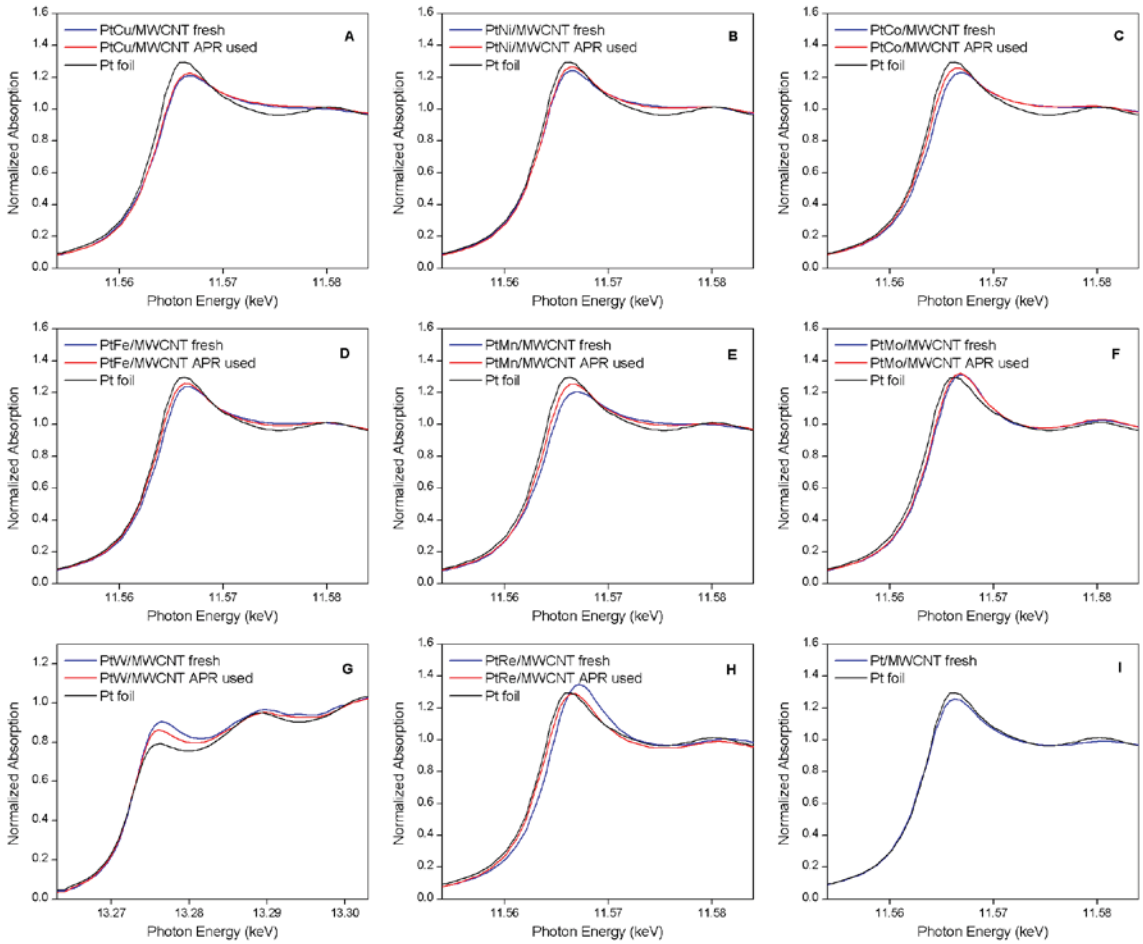

Figure 2.3 XANES spectra of the Pt L_{III} (or Pt L_{II} for PtW) edge of the reduced bimetallic (A-H) and monometallic (I) catalyst before (blue) and after (red) reaction as compared to reference Pt foil (black). Edge positions of all spectra are shown in Table S.3.

2.4.2 EXAFS

Extended x-ray absorption fine structure (EXAFS) was analyzed and fit for the reduced bimetallic PtM/MWCNT catalysts before and after reaction to determine the differences in alloy structure among the different promoter metals. The R-space of the k^2-weighted

Fourier transform data of the various promoter metal edges are displayed in Figure 2.4. The Cu, Ni, Co, and Fe promoted catalysts' spectra are dominated by the single metallic peak at a similar position to the metal foil (approx. 2.5 Å). In contrast, the Mn spectrum of the fresh PtMn catalyst (Figure 2.4E) is characterized by a Mn-O peak at 2.15 Å and large Mn-Mn peak at 3.04 Å which is significantly longer than that for Mn foil (2.70 Å), but similar to the metal bond distance in bulk MnO (3.14 Å), indicating that Mn is predominantly oxidized in the fresh catalyst and forms no discernable alloy. For the 3d metals Cu, Ni, Co, and Fe, the used catalyst has decreased metallic peak intensity and a slight increase in the left shoulder corresponding to more M-O scatter, which is seen quantitatively in the EXAFS fits tabulated in Table S.4 and S.5 and is consistent with the XANES fits. The less reducible and more easily leached metals Co and Fe have a more dramatic decrease in the metallic peak than Cu and Ni. In the Mn K edge spectrum of PtMn, a metallic peak emerged after reaction, which was fit with Mn-Pt backscattering only, indicating that alloy formation is occurring during reaction.

Mo K edge and and W L_{III} edge had low R scattering which is too long for typical oxides (2.08 and 2.10Å), and are more typical to Mo-C and W-C scatters for Mo_2C (2.10 Å) and WC (2.20 Å). The PtMo was fit with a Mo-Pt and Mo-Mo at a length greater than that of Mo foil (2.80 versus 2.73 Å), which is characteristic of an interstitial carbide (see Table S.5). The fresh and used PtMo spectra were very similar. In contrast, the PtW spectra are quite different in the W-M coordination number. The fresh catalyst contains distinct W-O (1.83Å) and W-C (2.10Å) bonds and very little W-M contribution, NW-M = 0.9. After reaction, there is increased W-M at a coordination number of 3.3. It is unlikely that this is due to metallic W after reduction at 450 °C, and it is more likely W-Pt

coordination that comes with alloy formation. Both W and Re have similar backscattering functions to Pt, so mixed W-Pt and Re-Pt cannot be discerned from W-W and Re-Re.

The Re L_{III} edge EXAFS had significant Re-O scattering in the used sample and corresponding decrease in Re-M coordination, due to some unreducible Re species present in the used sample which were not present in the fresh sample.

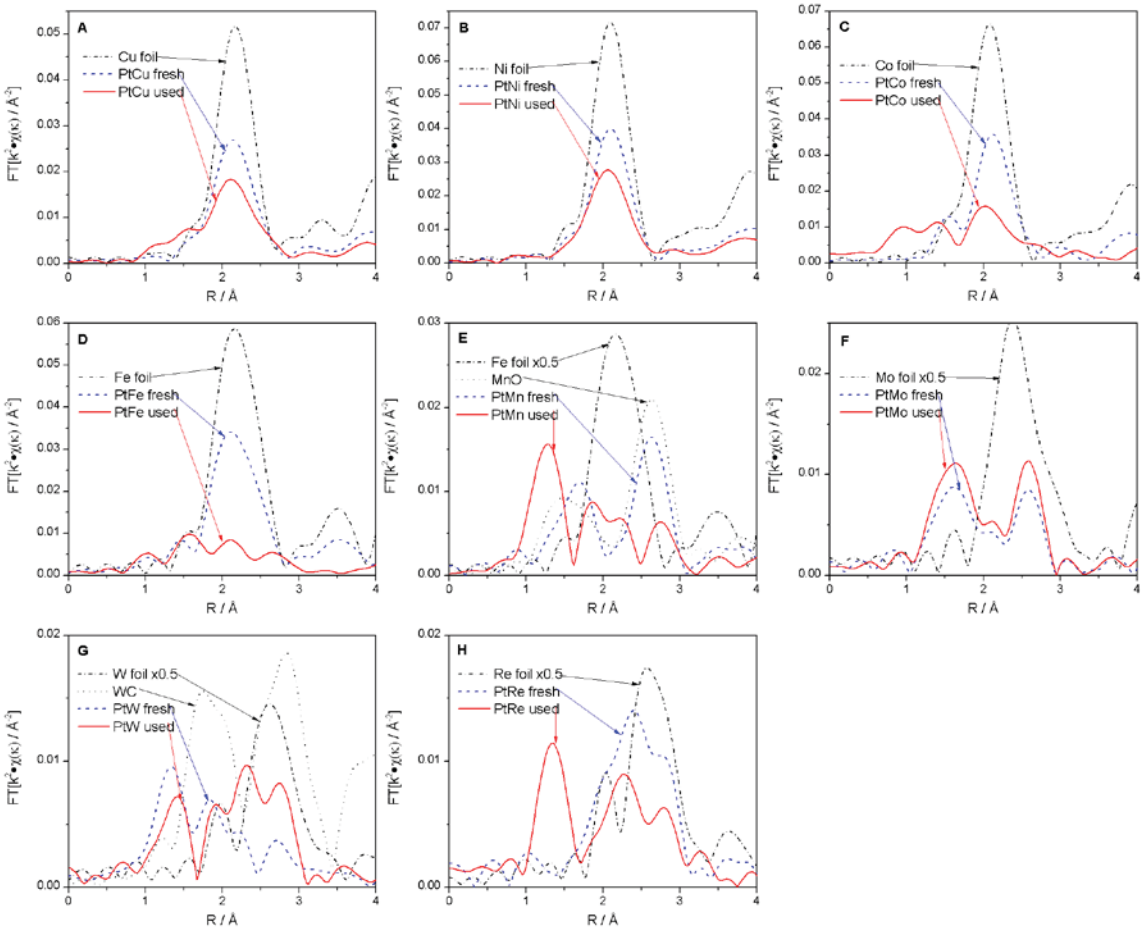

Figure 2.4. Magnitude of the FT of the M K (or L_{III} for PtW and PtRe) edge k^2-weighted EXAFS of the reduced bimetallic catalysts before (blue, dash) and after (red, solid) reaction as compared to reference M foil (black, dash/dot) and any relevant bulk oxide or carbide references.

The Pt L_{II} and L_{III} edge EXAFS in Figure 2.5 show an increase in the metal peak for all catalysts due to some degree of sintering during APR. Bimetallic catalysts with 3d promoter metals susceptible to leaching had a disproportionate increase in the right shoulder of the three metal peaks compared to the whole group of peaks. This is due to the decrease in Pt-M contributions to the peak, which is supported by the fit results indicating a decrease in the Pt-M coordination across PtNi, PtCo, PtFe, and PtMn catalysts (Table S.4).

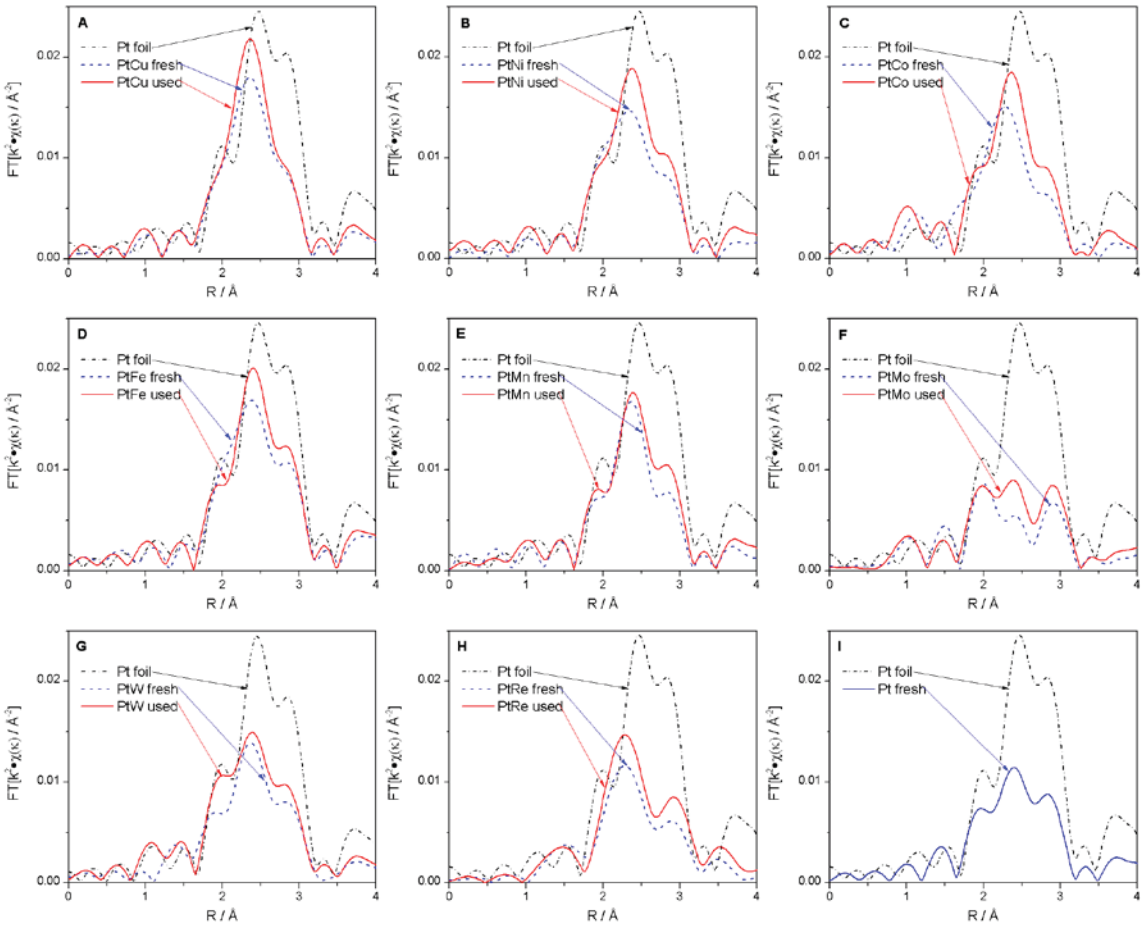

Figure 2.5 Magnitude of the FT of the Pt L_{III} (or Pt L_{II} for PtW) edge k^2-weighted EXAFS of the reduced bimetallic (A-H) and monometallic (I) catalyst before (blue, dash) and after (red, solid) reaction as compared to reference Pt foil (black, dash/dot).

2.4.3 Density functional theory calculations

2.4.3.1 OH Binding sites

The calculated OH binding energy on each Pt_3M (111) surface increased in a similar order to what has been reported in literature for O binding energy on M (111) surfaces [27]. This trend in OH binding energy will also be used to reference to the reducibility of the metal promoters in the order of least reducible to most reducible: W < Mo < Re < Mn < Fe < Co < Ni < Cu. The optimal OH binding site for each Pt_3M (111) alloy surface shown in Figure 2.6 varied among the promoter metals, but followed a discernable trend. From the most reducible metal Cu to the least reducible metal W, the OH binding site changes from Pt-Pt bridge to Pt-M bridge to M top site. The OH binding strength increases in the direction of increasing oxophillicity of promoter metal from Cu to W, which was expected due to the similarity of O and OH absorbates.

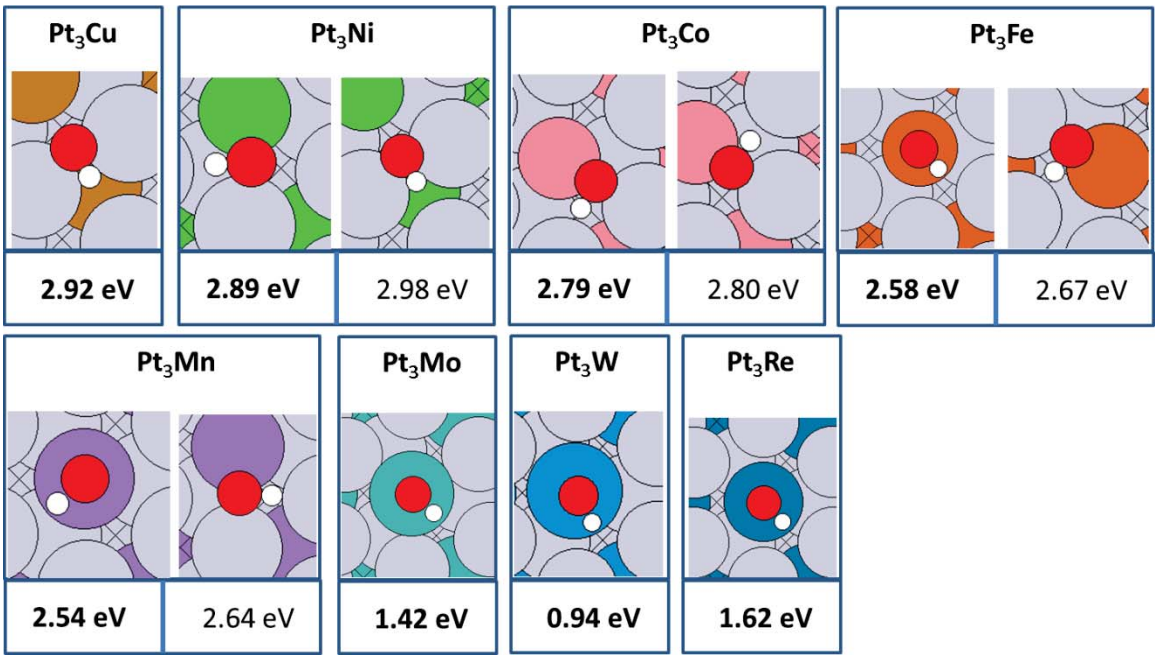

Figure 2.6 Optimal OH binding configurations on Pt_3M alloys. The two lowest energy configurations are displayed if within 0.1eV.

2.4.3.2 CO + OH Binding energies

The role of CO adsorbed on the catalyst surface during both WGS and APR was assessed by calculation of CO binding energy on the clean Pt_3M (111) surfaces and comparing to WGS TORs and APR STYs with no correlation resulting (Figure A.4). The effect of CO adsorbed to the metal surface on OH binding energy values was assessed by adsorbing OH on a Pt_3M surface which had CO already adsorbed. The two most important cases considered were CO allowed to adsorb to the lowest energy binding site, and CO positioned in the Pt-top position which has is experimentally more accurate of the actual Pt surfaces. A sampling of the lowest energy configurations, which includes both of the aforementioned cases are shown in Figure A.5. Both cases provided similar OH binding energies to that of the clean surface (Figure A.6). A third case of CO adsorbed on M-top

site resulted in significantly higher OH binding energies, especially for Pt_3Mo, Pt_3Re, and Pt_3W. This third case is least relevant experimentally due to the affinity of OH for the same sites under reaction conditions of both WGS and APR.

2.5 Discussion

2.5.1 Effect of aqueous reaction environment on catalyst structure

Changes to the metal structures which occurred during reaction were analyzed for broad trends among the eight bimetallic samples. Figure 2.7A indicates that exposing the catalyst to reaction conditions generally results in a lower fraction of mixed Pt-M scattering, i.e. a decrease in alloying. For 3d metals this is due to a combination of metal leaching into solution depleting the PtM alloy phase, as well as the oxidation of M resulting in MO_x at the particle surface. In the case of Mo, since no metal leaching has been detected, the cause for dealloying is exclusively the oxidation of Mo to surface MoO_x species on the PtMo particle surface. Considering the other half of the bimetallic data, Figure 2.7B displays the fraction of M-Pt mixed scatter in the promoter metal EXAFS fits. After exposure to the reaction environment there was a small increase in the fraction of mixed scatter for PtCu, PtNi, and PtCo. For PtFe and PtMn metallic scatter was all M-Pt such that the average bonding of metallic M was only to neighboring Pt and not to other M atoms. While this may appear in contradiction to the Pt L_{III} edge fits which indicate that the particles are becoming more Pt-rich, the fraction of M-Pt scatter increases as the non-alloyed promoter metal species are either leached to the solution (and removed from the bulk average) or oxidized forming M-O bonds. The PtMo catalyst's decrease in fraction of M-Pt was consistent with the Pt data in Figure 2.7A. Mathematically, a catalyst which is synthesized with PtM in a 1:1 ratio should have Pt-M

and M-Pt coordination numbers equal to each other [28]. While there is some error associated to EXAFS fits that prevents this equality from being precisely true experimentally, large deviations indicate loss of one metal relative to the other. Figure 2.7C illustrates this fact across catalysts which change total composition during APR. All fresh catalysts have $N_{M\text{-}Pt}/N_{Pt\text{-}M}$ values near unity. However, after APR there is an increase in this ratio which indicates a loss of promoter metal for PtNi, PtCo, PtFe, and PtMn. The change is especially large for Fe and Mn which as mentioned above show entirely M-Pt coordination from the metal EXAFS fits after reaction. It is important to note that even though the $N_{M\text{-}Pt}/N_{Pt\text{-}M}$ value for PtMn is high (5.4) due to a large amount of metal leaching, the glycerol STY actually increases for this catalyst up to 69 % after 8 days on stream. Thus the decrease in bulk alloy actually did not correspond to a decrease in activity, and it is more likely that excess MnO_x was covering surface sites. Removal of this excess oxide was able to increase the number of exposed sites while still providing an adequate amount of promoter metal to increase the reaction rates.

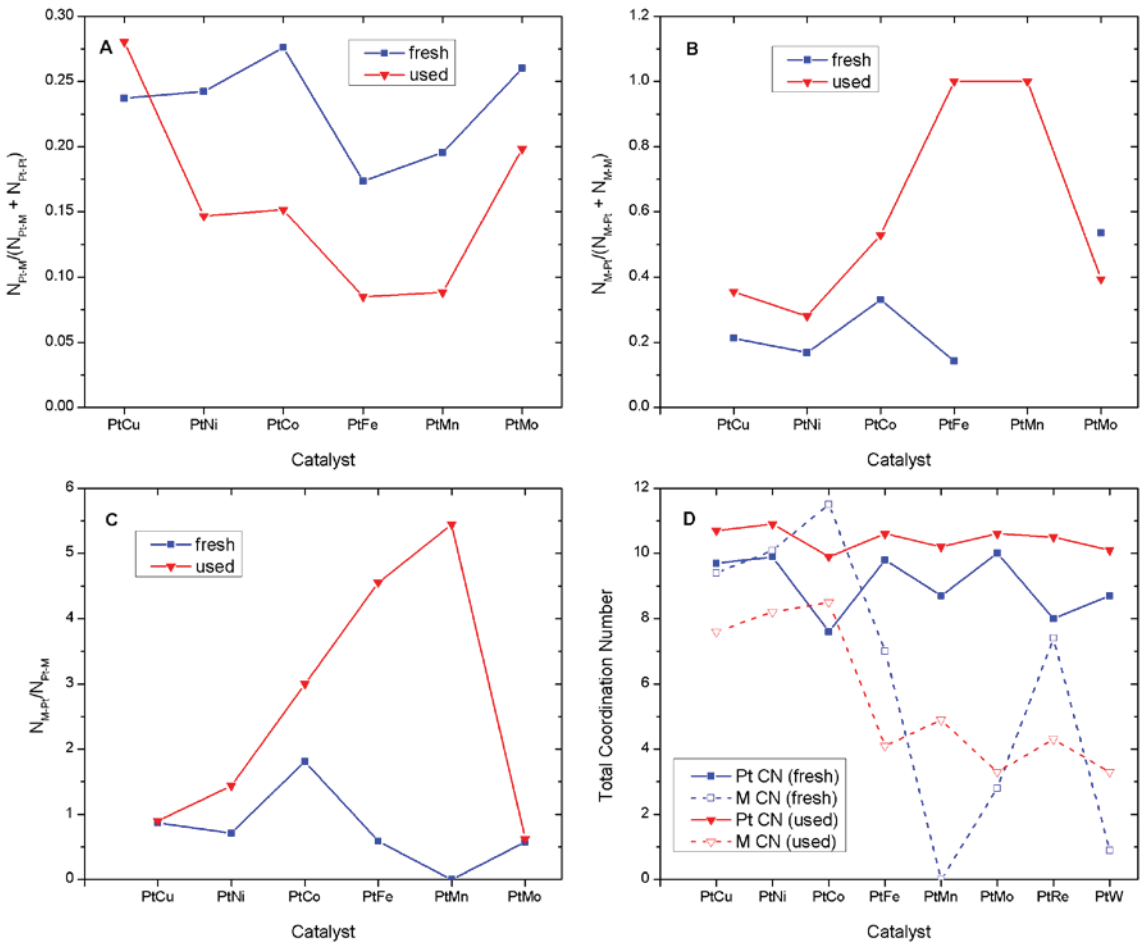

Figure 2.7 (A) Fraction of mixed scatter of Pt EXAFS fits. (B) Fraction of mixed scatter for M EXAFS. (C) Ratio of M-Pt to Pt-M scatter in bimetallic catalysts. (D) Total metal coordination number for Pt and M EXAFS both before (blue) and after (red) reaction.

Figure 2.7D uses the information from total metal coordination available for all samples to compare the core-shell preference of alloy nanoparticles before and after reaction. The core-shell preference is an independent consideration from the amount of mixing of the two metals, which was considered in Figures 2.7A and 2.7B. This is also the only configuration information for PtW and PtRe, which cannot differentiate mixed scatter from monometallic scatter. When comparing the total Pt and total M coordination number, the metal which has a larger value tends to segregate towards the core of

bimetallic particles (closer to fully coordinated bulk metal), and the metal which has a smaller value tends to segregate towards the shell of the particles (fewer bonds due undercoordinated surface atoms) [28]. Thus, the fresh PtCu, PtNi, and PtRe catalysts have little or no core-shell preference of the mixed nanoparticles due to similar total Pt and M coordination numbers. PtFe, PtMn, PtMo, PtW prefer Pt-core, M-shell configurations due to the higher relative Pt total coordination, and PtCo prefers an M-core, Pt-shell configuration due to the higher relative M total coordination. Regarding the used samples, all bimetallic compositions prefer Pt-core, M-shell configurations, with the preference significantly stronger for the more oxophillic metals in PtFe, PtMn, PtMo, PtRe, and PtW. This is the opposite prediction of theory calculations for both bimetallic metal clusters and extended surfaces [13, 29]. The difference in this case is that the catalysts have been shown to have partially oxidized metal promoter, which will conflict with the oxygen-free environment of reduced metals used in the DFT calculations in literature.

It is important to note for the catalysts PtRe and PtW that this analysis of core-shell preference assumes that most of the metals are forming bimetallic particles. If the metals were to form mostly separate monometallic particles the difference in total Pt coordination and total Re (or W) coordination numbers could be satisfied by separate monometallic particles of different average sizes, without the actual formation of alloy particles that prefer a core-shell arrangement. So while EXAFS cannot provide a measure of alloy formation, the XANES spectra show changes in white line intensity and edge position of both Pt L_{II}/L_{III} and Re L_{III} or W L_{III} edges that imply the electronic effect of intimately mixed metals forming some amount of alloy phase for both catalysts. The

extent of mixing also qualitatively decreases for both of these catalysts after reaction since the shift becomes smaller in the XANES spectra after reaction. Also, note that despite the evidence for some amount of carbide phase for both PtW and PtMo after reduction of fresh and used catalysts at 450 °C, under reaction conditions of both WGS and APR it is very unlikely that these metal carbide species would not oxidize due to the highly reactive nature of transition metal carbides.

In previous studies of PtCo and PtMo catalysts by our group [30, 31], we performed *operando* XAS characterization of the bimetallic structures and studied the structural differences between these promoter metals. Under the hot aqueous environment of glycerol reforming there was a decrease in the Pt-Co and Pt-Mo coordination, with the final state of PtMo being more phase segregated than PtCo due to the greater oxophillic nature of Mo and the loss of Co to leaching. In this study, the entire range of bimetallic catalysts evolves from various starting configurations to similar Pt-core, M-shell preferred configurations after reaction. The difference between catalysts depends on how easily oxidized the promoter metal is; with the more reducible metals (Cu, Ni, Co) having a weaker core-shell preference as in the *operando* experiments. While not as accurate as *operando* measurements of the working catalyst, the used catalyst configuration is a good approximation of the bimetallic structure for these PtM/MWCNT samples. This comparison has already been performed for a series of PtCo/MWCNT catalysts in a recent publication of ours [9]. The path from the fresh to the used bimetallic structures may also follow different routes for different metal combinations. The leaching of some metals (particularly the 3d promoters) in the hot aqueous environment contributed to the observed Pt-rich core configurations, while for others this was not a contribution.

During the optimization of the OH binding energy on Pt_3Mo, Pt_3Re, and Pt_3W surfaces, there was reconstruction in the subsurface layer of metal when OH was positioned on Pt-rich sites, resulting in the exchange of a Pt and M atom, as seen in Figure A.7. This rearrangement resulted in increasing the number of M-M bonds. The new configuration was a lower energy by 0.93 eV for Pt_3Re, 0.89 eV for Pt_3Mo, and 0.72 eV for Pt_3W. While the purpose of the DFT modeling in this study was not focused on metal segregation, this spontaneous rearrangement is evidence from theory that in the presence of atomic oxygen or hydroxyl species such as the WGS or APR reactions strongly oxophillic metals may phase segregate *in situ*.

Even samples with significant leaching did not suffer dramatic deactivation and one catalyst increased in rate (PtMn), indicating that the final active structure formed due to the compositional change is stable under APR conditions. For catalysts with unchanging total composition (PtCu, PtMo, PtRe), structural changes were also observed. This suggests that under liquid phase reaction conditions there is a different thermodynamic minimum than that of a gas phase hydrogen atmosphere, and adequate metal mobility to obtain this different configuration. This rearrangement to a more stable configuration appears to be irreversible since during re-reduction the original structure is not regained.

2.5.2 Effect of catalyst structure on reactivity

Catalyst structure is connected to reactivity for WGS and APR, like many other catalytic systems. The selectivity towards C-O bond scission over C-C bond scission during aqueous phase reforming results in poor H2 selectivity. The catalysts displaying the lowest H2 selectivity (PtMo, PtRe, PtW) also have the most oxophilllic metal promoters. The EXAFS of these used catalysts show that these bimetallics also have the strongest

preference towards Pt-core, M-shell particle segregation. While for all bimetallic catalysts surface segregation of M atoms will provide surface Pt-M sites that may facilitate pathways to hydrogenolysis of C-O bonds, there is also Brønsted acidity created from surface metal oxides such as MoO_x, ReO_x and WO_x. This increased Brønsted acidity is evidenced by higher ratios of 1,3-propanediol to 1,2-propanediol for these three bimetallic catalysts. 1,3-propanediol is favored by the acid catalyzed process of C-O scission by dehydration/hydrogenation due to the formation of a secondary carbocation. The same mechanism would require creation of a primary carbocation for producing a molecule of 1,2-propanediol. Due to the increased Brønsted acidity of these three samples which has recently been quantified as low deprotonation energies by DFT calculations [10, 23], the activation barrier for this route of 1,3-propanediol formation is lower and the rates higher than other alloy compositions. It is also happens that all other PtM catalysts have lower selectivity to 1,3-propanediol than monometallic Pt/MWCNT, which would indicate that either the surface acidity is lower upon addition of these other metal promoters or that the rate of direct hydrogenolysis increased relative to acid-catalyzed C-O scission.

By comparing the WGS TOR and APR STY of all bimetallic and monometallic catalysts in Figure 2.8, there appears a roughly linear correlation for all samples except PtMo/MWCNT (WGS TOR = 2.68×10^{-2} s^{-1}), which is the catalyst with the lowest H_2 selectivity. This would be in agreement with a common rate determining step which is promoted by the addition of the secondary metal.

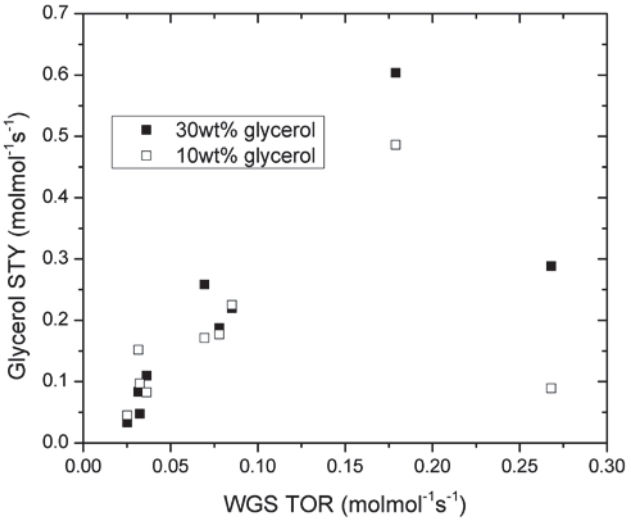

Figure 2.8 Glycerol STY during APR versus WGS TOR. WGS TORs were interpolated to 300 °C with standard gas feed composition of 6.8% CO, 21.9% H_2O, 8.5% CO_2, 37.4% H_2 and balance Ar. Glycerol APR STYs were obtained at 230 °C, 32 bar total pressure, 10 or 30 wt% glycerol feed, and 0.30 mL/min liquid flow rate.

In an attempt to assess whether water dissociation is the key step in both reactions, the calculated OH binding energy for the Pt_3M (111) surface was used as a chemical descriptor to plot the rates of both WGS TOR and glycerol APR STY in Figure 2.9.

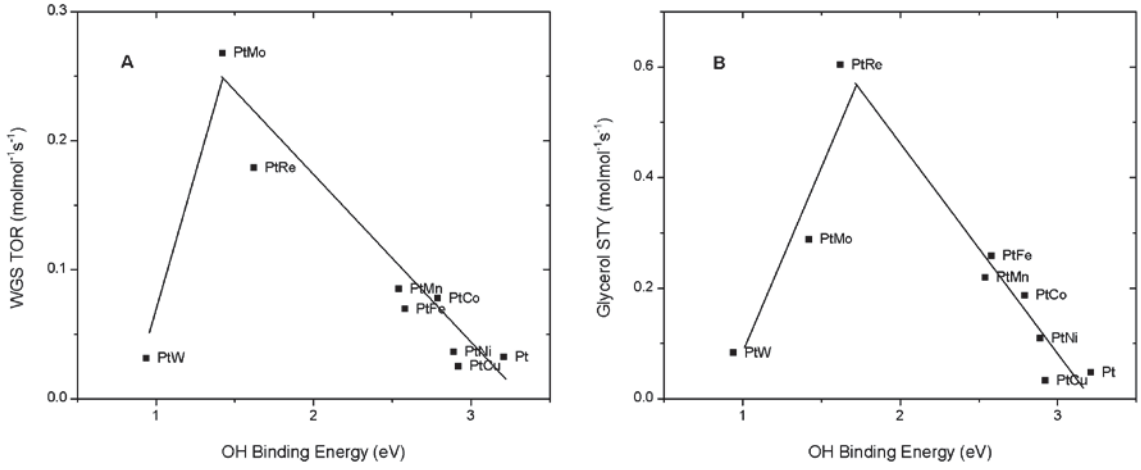

Figure 2.9 (A) Plot of WGS TOR versus calculated OH binding energy for Pt_3M (111) surfaces. (B) Glycerol STY versus calculated OH binding energy for Pt_3M (111) surfaces. Glycerol APR STYs were obtained at 230 °C, 32 bar total pressure, 10 or 30 wt% glycerol feed, and 0.30 mL/min liquid flow rate.

OH binding energy was chosen both to assess the preferred OH binding site on the bimetallic surface, and to decrease the complexity and computational cost of performing complete transition state calculations for water dissociation on all possible sites using DFT. The correlation between the oxygen binding energy and activation barriers of water dissociation on monometallic close-packed surfaces has already been well established by linear scaling relations in the DFT literature [32]. The volcano plot which results for each reaction shows that the reaction rate increases with increasing OH binding energy for each reaction up to a point and then begins to decrease. The optimum for each reaction differs, though, and is closer to PtMo/MWCNT for WGS reaction and closer to PtRe/MWCNT for APR. By these plots it appears likely that the water dissociation which results in surface OH species is the rate determining step of both reactions.

The measurement of a kinetic isotope effect of 1.7 during glycerol APR confirmed that the WGS reaction is involved in the rate determining step for APR. However, there are multiple elementary steps within the WGS reaction which include H/D from water/deuterium oxide besides water dissociation such as hydroxyl dissociation and carboxyl or formate formation and decomposition. While this experiment only indicates that some step in the WGS reaction is rate determining for the overall glycerol reforming reaction and not glycerol decomposition, we can further narrow the possibilities by considering the importance of OH binding energy as a chemical descriptor for both WGS and APR.

The optimum descriptor value in a volcano plot of a series of catalysts usually implies that a common reaction mechanism has a region in which adsorbate binding is too weak

and a region in which adsorbate binding is too strong. The real picture in high surface area metal catalysts is more complicated, however, due to multiple kinds of binding sites (surface, perimeter, corner) on metal nanoparticles. Also, bimetallic catalysts may not have a well-characterized starting structure, and this structure may be considerably different under operating conditions where the catalyst is turning over. That is why it was imperative that the question of bimetallic catalyst structure is addressed in coordination with asserting a descriptor-based correlation to reaction rates.

The consideration which is missing from this simple descriptor-based volcano plot is the difference in alloy structure in the two reaction environments which differ in how reducing or oxidizing they are for the metals. Considering the volcano plot maximum in light of the effect of reaction environment on bimetallic catalyst structure, the OH binding energy may not be optimized. Instead, there may simply be a balance between increasing rates due to higher OH binding energy and fewer Pt sites due to more strongly oxophillic promoter metals like Re, Mo, or W forming surface oxides under reaction conditions which cover Pt reaction sites. There is also evidence in the DFT calculations for this occurring in the presence of water, as sub-surface rearrangement of the Pt3Re, Pt_3Mo, and Pt_3W spontaneously occurred when optimizing the binding energy for adsorbed OH (Figure A.7). The promoter metals with the greatest affinity for oxygen in this study (Re, Mo, W) may all favor phase segregation similarly and this structural consideration may be a more realistic explanation for the decreasing TORs for WGS reaction and STYs for APR left of the peak in the volcano plots. The difference in the more oxidizing environment of APR versus the more reducing environment of WGS is an explanation for why PtMo is the most active catalyst for WGS, while PtRe is the most

active catalyst for glycerol APR; there may be a more severe structural change in the catalyst which occurs *in situ* during exposure to hot liquid water in APR versus gas phase WGS.

In order to see if WGS TOR and APR glycerol STY can be correlated as well to the descriptor of CO binding energy as with OH binding energy, a similar plot was assembled for this different chemical descriptor. By comparing the plots in Figure 2.9 to those in Figure A.4 it seems that OH binding energy is a much better descriptor for both reactions, as there is no discernable correlation of the reaction rates with CO binding energy. OH was also adsorbed on several surfaces with preadsorbed CO, as shown in Figure A.5. Based on previous *operando* XAS studies by our group which show predominantly CO adsorbed on Pt under APR reaction conditions, as well as the existing body of literature which says that CO prefers the Pt top site, it is likely that the preadsorbed CO on Pt top sites is the best scenario to consider. Considering all four calculations in Figure A.6, there appears to be little difference except in the case of CO adsorbed on the M top position. This is also the least likely scenario in the presence of steam or hot liquid water which, especially for the more oxophillic metals, is likely to cause these sites to be occupied primarily by O or OH species.

Another insight from the coadsorbed CO + OH calculations is the observation of new sites created for water dissociation, which then frees up surface Pt atoms for additional reactions (glycerol decomposition or WGS). For example, in Figure A.5 the lowest energy scenarios usually include an M top binding site for OH plus some type of Pt-rich site for CO adsorption. This is advantageous if the glycerol decomposition portion of APR occurs primarily on the Pt atoms or ensembles, allowing two sites to hold two

different types of adsorbates in a dual site mechanism for the overall APR reaction. Thus, it is not surprising that water dissociation may be the key step in both reactions, which is facilitated by the addition of promoter metals to Pt/MWCNT catalysts. The formation of new sites for facile water dissociation as modeled by OH adsorption is likely the primary mechanism of rate promotion for these bimetallic catalysts.

2.6 Conclusions

The glycerol reforming STY of Pt/MWCNT catalysts have been promoted up to 13 times by addition of transition metal promoters Cu, Ni, Co, Fe, Mn, Mo, W, and Re in Pt:M 1:1 atomic ratios. The bimetallic structure and oxidation state of the catalysts before and after reaction were determined by analysis of EXAFS and XANES spectra to characterize the differences in catalyst compositions which resulted in different degrees of rate promotion. While the fresh structure varied among the catalyst compositions, the used samples had similar preferences toward Pt-core, M-shell configurations, with some amount of oxidized M even after reduction in hydrogen. The trend of stronger Pt-core, M-shell preference for more oxophillic promoter metals was consistent despite the loss of some metal to solution during the APR reaction.

The measurement of the kinetic isotope effect for replacement of water with D_2O during glycerol reforming determined that the rate determining step for APR is one which involves the O-H bond in water, not glycerol decomposition. Hypothesizing that the barrier to water dissociation could be estimated by DFT calculation of OH binding energies on the Pt3M (111) surface, volcano plots for both WGS and APR reactions resulted in an optimal value for OH binding energy. Additionally, DFT revealed the more oxophillic metal promoters make use of separate sites for water dissociation that

otherwise would require Pt sites that are used for glycerol decomposition. This dual site advantage was explicitly shown by adsorbing OH to bimetallic surfaces which already contained CO surface adsorbates. Thus, with the combination of kinetic, spectroscopic, and theory calculations we find that the future design of bimetallic catalysts for APR and WGS reactions for maximum rates should consider both the ease of water dissociation and the catalyst structure caused by addition of the promoter metal.

CHAPTER 3. EFFECTS OF METAL DISTRIBUTION IN PTRE BIMETALLIC CATALYSTS FOR AQUEOUS PHASE REFORMING

3.1 Introduction

Due to the need for sustainable processes for the production of fuels and chemicals in the future, much effort in recent years has been directed at finding substitutes for non-renewable oil and natural gas-based chemical production. Much of the research has centered around conversion of biomass via pyrolysis and hydrodeoxygenation [33], or catalytic conversion of biomass-derived sugars and sugar alcohols [34-36]. Common to these proposed processes is the addition of large amounts of hydrogen to removed oxygen from biomass in the form of water in order to maintain carbon atom efficiency. In order to avoid using non-renewable resources by producing hydrogen by steam reforming of hydrocarbons, a renewable source of hydrogen is desired to make green fuels and chemicals. One route to renewable hydrogen from biomass is aqueous phase reforming, for which platinum catalysts reform sugar alcohols in hot liquid water to CO_2 and H_2 [1]. These Pt or Pd catalysts can further be promoted by the addition of a secondary metal, which may or may not retain the high hydrogen selectivity of Pt monometallic catalysts [2, 8, 30].

Recent studies have considered the effects of Re addition to Pt catalysts for both gas phase reforming [6] and aqueous phase reforming [19] in terms of both rates and

selectivity. These effects include decreasing CO binding strength on adjacent Pt sites [6] to increase reforming rates, as well as providing Re-OH species which can either react with adsorbed CO to form COOH and increase the rate of water-gas shift (WGS) reaction or react with alcohol moieties to perform C-O hydrogenolysis. Since the rate of C-O bond scission can determine whether the reforming reaction has high hydrogen selectivity or high alkane selectivity, additional investigations have used ammonia temperature programmed desorption (NH_3-TPD) to count the strength and number of acid sites created by Re addition. One study determined that Re addition to Pt/TiO_2 increases the strength of acid sites, but decreases the number of acid sites for the reduced catalyst [20]. Separately, it was found that Re addition to Pt/C catalysts which have been steam treated at elevated temperatures to oxidize the Re to Re-OH caused an increase in the number of acid sites proportional to the amount of added Re, while at the same time keeping the acid strength constant [21].

Bimetallic catalysts can have a variety of different metal distributions and alloy particle configurations, which can affect both turnover rates and selectivities for reactions. In a recent publication from our group a series of PtCo bimetallic catalysts supported on multi-walled carbon nanotubes were studied in the distribution of well-mixed, core-shell, and monometallic particles by electron energy loss spectroscopy (EELS) of the used catalysts [9]. Also, studies from literature indicate that the particle size and sintering is decreased for bimetallic PtCo catalysts used for APR if carbon nanotube supports are pretreated with nitric acid to create surface oxygen groups [37, 38].

This work looks to identify the reasons for such departure in product selectivity of the PtRe/MWCNT catalyst compared to the well-studied PtRe/C catalyst, which has

heretofore been recommended as being efficient in C-O scission for production of deoxygenated product by aqueous phase reforming. We quantified the number of acid sites or the strength of acid sites on bimetallic PtRe catalysts to determine on the number and strength of acid sites, and whether the sites are assigned to surface alloy Pt-Re or isolated ReO_x species.

3.2 Experimental

3.2.1 Catalyst Synthesis

Three catalysts were synthesized on multi-walled carbon nanotube (MWCNT, 233 $m^2 g^{-1}$ BET surface area) supports (Cheaptubes, Inc.): 5 % Pt, 5 % Re, and 5 % PtRe(1:1). One catalyst was prepared on a traditional activated carbon support (Norit-SX1G, 1000 $m^2 g^{-1}$ BET surface area): 5 % PtRe(1:1). All catalysts were performed by incipient wetness impregnation of an aqueous solution of tetraammineplatinum(II) nitrate or ammonium perrhenate. Bimetallic samples were synthesized by sequential impregnation of the aqueous platinum salt solution, overnight drying in air at 60 °C, and then impregnation of the aqueous rhenium salt solution, and finally overnight drying in air at 150 °C.

3.2.2 Reaction kinetics measurements

Glycerol aqueous phase reforming was performed in a fixed bed reactor made of 10 mm × 6 mm × 200 mm (OD×ID×L) quartz tube (Chemglass, Inc.) or 10 mm × 4 mm × 200 mm (OD×ID×L) Sigradur glassy carbon tube (Hochtemperatur-Werkstoffe). For a typical experiment 30 to 150 mg of unsieved catalyst powder was loaded between quartz wool plugs supported between stainless steel rod spacers [16]. Catalyst bed temperature was controlled by a K-type thermocouple (Omega) inserted through the top quartz wool plug to the top of the catalyst bed. The reactor was heated by a custom aluminum heater

block with cartridge heaters through a PID temperature controller (Eurotherm). The catalyst was reduced *in situ* for 2 hours (2 hour ramp) by flowing 50 sccm of 5 % H_2/Ar gas mixture at 450 °C (400 °C for Pt/MWCNT). After cooling to room temperature, the liquid feed (5, 10, or 30 wt% aqueous glycerol solution) was pumped in an up-flow configuration into the reactor by a dual syringe pump (Teledyne ISCO) or HPLC pump. Once the liquid had filled the system, the pressure was increased to 32 bar with a biphasic backpressure regulator (Equilibar), and the catalyst bed temperature was increased to 230 °C (2 hour ramp).

The gases from a downstream phase separator were swept continuously with 14 sccm Ar as an internal standard to be analyzed by an online gas chromatograph (Agilent 7890). A Carboxen 1000 packed column and TCD detector were used with N_2 carrier gas (H_2 quantification) or He carrier gas (CO, CO_2, CH_4, and C_2H_4 quantification). At regular intervals liquid samples were drained from the phase separator using a liquid chromatography fraction collector (SpectraChrom CF-1). Each liquid sample was analyzed by a DB-WAX capillary column with an FID detector. Diethylene glycol was added to each liquid sample as an internal standard.

Reaction rates were quantified in terms of glycerol site time yield (STY), defined as the rate of glycerol consumption normalized per surface site as counted by CO chemisorption. This convention is used in place of a turnover rate (TOR) because the conditions were not differential since products were not co-fed. An additional complication for defining a turnover rate comes from the fact that glycerol APR consists of many parallel and series reactions. Carbon selectivity for glycerol reforming is defined for each product or product grouping as $(\Sigma(r_{product} \times \text{carbon number}))/(r_{glycerol} \times 3) \times 100\%$. The

product groupings are [C-C] scission products (ethylene glycol and methanol), [C-O] scission products (acetaldehyde, propionaldehyde, acetone, 2-propanol, ethanol, 1-propanol, hydroxyacetone, propylene glycol, and 1,3-propanediol), and acid products (acetic acid and propionic acid). Hydrogen selectivity is defined as $(r_{H_2})/(r_{H_2} + 4 \times r_{CH_4} + 7 \times r_{C_2H_6}) \times 100\%$. This is the fraction of H_2 which was actually produced versus the total H2 which would have been produced if the final products methane and ethane were fully reformed to CO_2 and H_2.

The water-gas shift reaction kinetics for each catalyst were collected with an automated system of four parallel fixed bed reactors described in a previous publication [17]. Conversion of CO was maintained below 10 %, and products (H_2 and CO_2) were co-fed to yield differential conditions. Apparent reaction orders and apparent activation energy were obtained by changing feed compositions and reaction temperature, respectively.

3.3 Catalyst Characterization

3.3.1 X-ray absorption spectroscopy

X-ray absorption spectra of all samples were obtained at the Advanced Photon Source, Argonne National Laboratory on the Materials Research Collaborative Access Team (MRCAT) Sector 10 insertion device beamline. Experiments were conducted at the Pt L_{III} and Re L_{III} edges, and experiments were conducted in transmission in quick scan mode. Every scan simultaneously captured a reference metal foil spectrum with a third detector in series for energy calibration. The x-ray beam was 1000 × 1000 μm for *ex situ* samples and 500 × 500 μm for *operando* measurements.

For *ex situ* measurements each catalyst was pressed into a 4 mm diameter self-supporting pellet within a six well sample holder. The holder was placed into an *in situ* reactor

constructed of a 1 inch quartz tube with an Ultra-Torr fitting, Kapton window, and shutoff valve on each end to allow for a controlled gas atmosphere. Samples were reduced in 3.5% H_2/He for 30 minutes at 450 °C (or 400 °C for Pt/MWCNT), purged with He, and cooled to room temperature before scanning. In order to measure the change in x-ray absorption near edge structure (XANES) due to adsorbed gases, the reduced catalyst was exposed to either 1 % CO/He or 3.5 % H_2/He for 30 minutes at room temperature and then scanned. The effect of adsorbed water was obtained by treating the samples with 50 sccm He routed through a water saturator at room temperature (approx. 3.2 Torr H_2O). Between gas treatments the samples were heated above 300 °C to desorb the previous adsorbed gas, and water treatment was last due to the possibility of partially oxidizing the Re metal. Reference materials scans were made by diluting the chemical with silica and scanning in air at room temperature. Sample loadings for the pellets were calculated to yield a total absorption (μx) above the edge of ~2.0.

Operando XAS measurements were obtained with the same glassy carbon tube reactor as used in the laboratory with identical reaction conditions and online gas product quantification to verify reaction rates. One condition was compared between PtRe/C and PtRe/MWCNT: 10 wt% glycerol at 230 °C, 32 bar, and liquid feed rate 0.30 mL/min. Several reaction conditions were then compared on the PtRe/MWCNT catalyst, the first of which was WGS at 1 bar and gas feed composition of 6.8 % CO, 21.9 % H_2O, 8.5 % CO_2, 37.4 % H_2, and balance Ar. Next, glycerol APR was performed at the same conditions as with PtRe/C, at three different feed compositions: 5 wt%, 10 wt%, and 30 wt% aqueous glycerol. Reaction rates from WGS and glycerol APR of 10 wt% glycerol

were compared to previously obtained rates in the laboratory to confirm that the catalyst was in the working state.

X-ray absorption spectra were analyzed by WinXAS 3.1 software following standard procedures for energy calibration to the experimental metal foil and background subtraction. After normalization, ΔXANES spectra of Pt L_{III} and Re L_{III} edges were obtained by subtracting the spectrum of the reduced catalyst in He from each spectrum after gas absorption or in *operando*. The EXAFS spectra were fit using the k^2-weighted Fourier transform (FT) EXAFS spectra from k of 2.7 to 12.0 $Å^{-1}$ for Re and k of 2.7 to 9.8 $Å^{-1}$ of Pt. The experimental Pt foil spectrum was used to generate the Pt-M scatter (Pt-Pt or Pt-Re), and the experimental Re foil spectrum was used to generate the Re-M scatter (Re-Re or Re-M). Only total coordination numbers can be extracted due to the mixed scatter shape being very close to that of the pure metal scatter. The Re-O scatter was isolated from ammonium perrhenate. The temperature dependence of the Debye-Waller factor ($\Delta\sigma^2$) was accounted for by taking spectra at reaction temperature and again after reaction and cooling to room temperature and making the assumption that coordination numbers and bond lengths are unchanged.

3.3.2 Scanning Transmission electron microscopy

The used PtRe/C and PtRe/MWCNT catalysts were each analyzed by scanning transmission electron microscopy (STEM) and electron energy loss spectroscopy (EELS) to determine particle size distributions and Pt and Re metal mixing and dispersion. Images were acquired with the dedicated aberration corrected STEM Hitachi HD-2700C at 200kV equipped with a modified Gatan Enfina ER spectrometer, located at the Center for Functional Nanomaterials, Brookhaven National Laboratory.

The EELS spectra for Pt and Re were collected at the $M_{4,5}$ edges and performed simultaneously for both metals. Particle size distributions for both catalysts were obtained from the STEM-HAADF micrographs with the ImageJ software package by counting at least 100 particles of the used catalyst.

3.3.3 Ammonia temperature programmed desorption

Ammonia temperature programmed desorption (NH_3-TPD) was performed on a Micromeritics Autochem II chemisorption unit which was outfitted with an Agilent 5975B mass spectrometer. For an experiment the catalyst powder was sieved >125 μm, and approximately 25 mg were loaded into the quartz u-tube between 2 quartz wool plugs. The sample was reduced in flowing H_2 for 2 hours at 450 °C (10 °C min^{-1} ramp). Optionally, the sample was cooled to 230 °C where it was treated with water vapor produced by flowing 50 sccm He through a water saturator at 25 °C (approximately 3.2 kPa H_2O). After flushing with dry He for 15 minutes, the sample was cooled to room temperature and saturated with flowing 3 % NH_3/Ar for 1 hour, followed by flushing with 100 sccm He for 6 hours. The TPD was performed by ramping the temperature at 10 °C min-1 to 450 °C in 50 sccm He, and recording NH_3 and H_2O signals (m/z = 17, 18) in the MS. The NH_3 signal was corrected for the water contribution and quantified by Ar pulse calibration.

3.4 Results

3.4.1 Glycerol reforming kinetics

Comparing the selectivity profiles of Pt/MWCNT, PtRe/MWCNT, and PtRe/C in Figure 3.1 reveals that all final products and liquid intermediates follow similar trends for these Pt-based reforming catalysts. For all three catalysts the selectivity to CO_2 begins around

40 % and monotonically increases with increasing carbon conversion as liquid intermediates are further reacted to form this final product which corresponds to complete C-C scission. Likewise, the alkanes CH_4 and C_2H_6 increase from 0 % with increasing carbon conversion as liquid intermediates that have already undergone C-O scission and have saturated hydrocarbon fragments further react by C-C bond breaking. The selectivity to liquid intermediates resulting from both C-O scission and C-C scission decrease monotonically as the carbon conversion increases, due to these further reforming to CO_2 or gaseous alkanes as final products. Finally, organic acids, which only appear for the bimetallic catalysts, increase from zero for PtRe/MWCNT, and decrease from a carbon selectivity of 4 % to 2 % for PtRe/C.

The major difference among the catalysts is in the relative selectivity of C-O and C-C scission, which results in different amounts of alkanes produced. In this respect, Pt/MWCNT and PtRe/MWCNT are similar at low conversions with twice the carbon selectivity to C-O scission products (40 %) as C-C scission products (20 %), but both C-O and C-C scission selectivity drop off more quickly for Pt/MWCNT by 50 % conversion (approximately 15 and 5 %, respectively). PtRe/MWCNT instead maintains higher selectivity to both liquid product groups, and by 50 % carbon conversion there is still approximately 40 % selectivity to C-O scission and 15 % selectivity to C-C scission products. The carbon selectivity towards alkanes, while higher for PtRe/MWCNT than Pt/MWCNT, still remains below about 9 % for both methane and ethane as conversion approaches 85 %. The large difference for PtRe/C is that the relative selectivity to C-O bond scission products is much higher than C-C scission products (approximately 40 % and 10 %, respectively). This large difference results in high selectivity to alkanes,

reaching 17 % carbon selectivity to ethane and 9 % selectivity to methane before reaching 80 % carbon conversion.

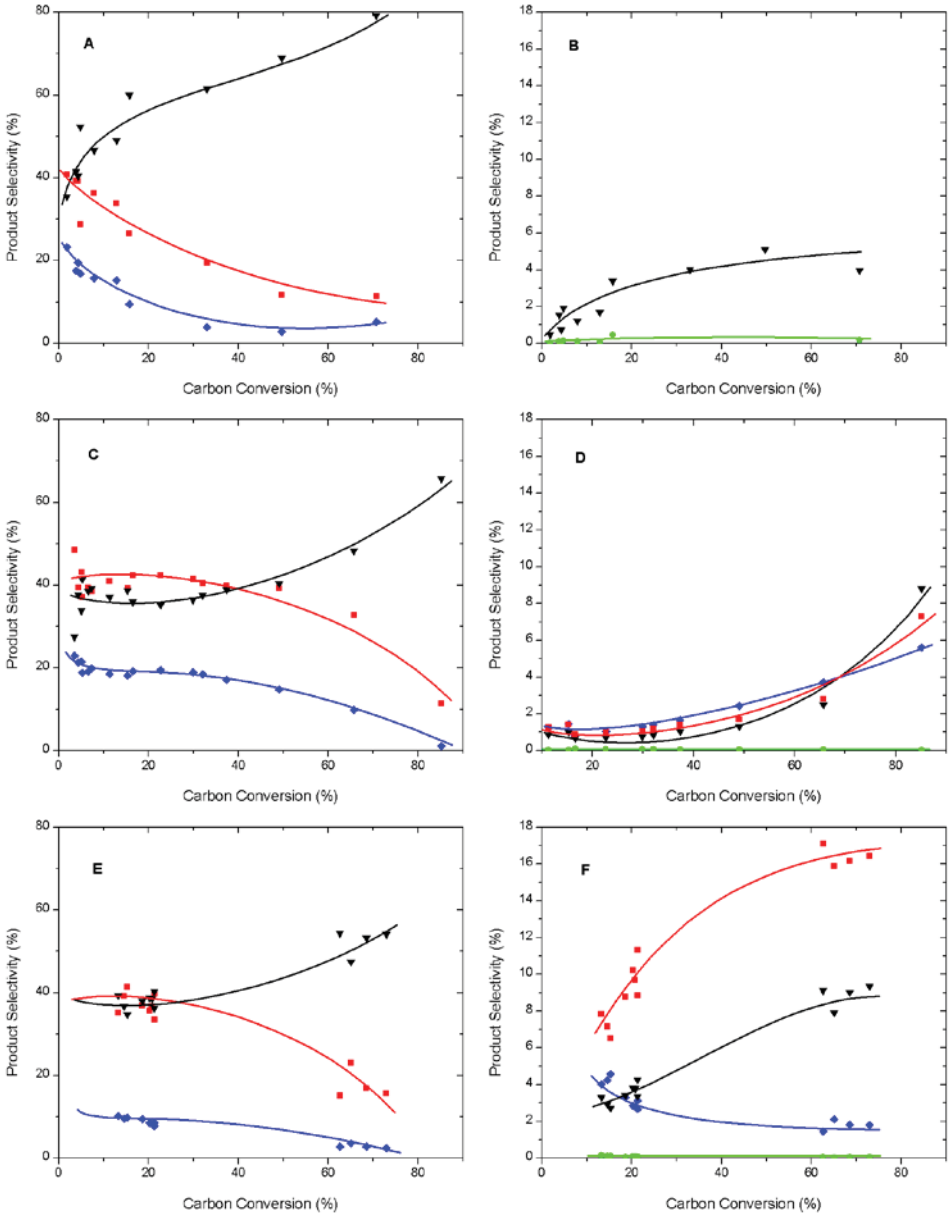

Figure 3.1 Carbon selectivity versus carbon conversion during glycerol APR for Pt/MWCNT (A and B), PtRe/MWCNT (C and D), and PtRe/C (E and F). The left column contains plots of major products: CO_2 (black triangles), [C-O] scission liquid products (red squares), [C-C] scission liquid products (blue diamonds). The right column contains plots of minor products: CH_4 (black triangles), C_2H_6 (red squares), organic acids (blue diamonds), CO (green circles). Data obtained at 230 °C, 32 bar total pressure, 10 wt% glycerol feed.

The difference in carbon selectivity directly affects the achievable hydrogen selectivity for each catalyst, as seen in Figure 3.2. Pt/MWCNT and PtRe/MWCNT catalysts have initial hydrogen selectivity above 92 % and decrease with increasing conversion as more alkanes are produced from liquid intermediates with saturated hydrocarbon fragments. PtRe/MWCNT drops as low as 65 % hydrogen selectivity by 85 % conversion, and Pt/MWCNT stays above 90 % hydrogen selectivity through 70 % conversion. PtRe/C initially has low selectivity to hydrogen (63 % at 12 % conversion) and continues to decrease down to around 45 % selectivity by 65 % conversion.

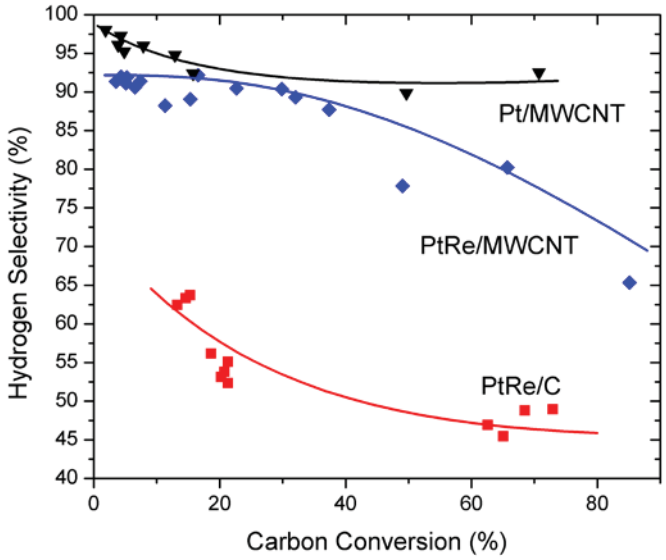

Figure 3.2 Hydrogen selectivity versus carbon conversion during glycerol APR for Pt/MWCNT (black triangles), PtRe/MWCNT (blue diamonds), and PtRe/C (red squares).

The reaction rate promotion for APR and WGS reactions differ for PtRe/MWCNT and PtRe/C catalysts. The glycerol STY for PtRe/C is 1.7 times higher than Pt/MWCNT but 5.5 times higher for PtRe/MWCNT, as shown in Table 3.1. There are similar differences in WGS rate promotion, such that among all four catalysts there is a linear relationship between WGS TOR and glycerol APR STY, plotted in Figure B.1. The reason for the

differences in selectivity towards C-C and C-O bond scission for the PtRe can be illustrated by the ratio of [1,3-PDO]/[1,2-PDO] produced. Since 1,3-propanediol is preferred over 1,2-propanediol in a Brønsted acid-catalyzed dehydration/hydrogenation pathway of C-O scission, those catalysts with a higher ratio have increased acidity [10]. Both bimetallic catalysts have a higher ratio than monometallic Pt or Re, with PtRe/C having nearly twice the ratio of PtRe/MWCNT.

Table 3.1 Kinetics and product selectivities for monometallic and bimetallic catalysts used for aqueous phase reforming of glycerol. Data obtained at 230 °C, 32 bar total pressure, 10 wt% glycerol feed, and 0.30 mL/min liquid flow rate.

Catalyst	**Pt/MWCNT**	**Re/MWCNT**	**PtRe/C**	**PtRe/MWCNT**
Dispersion (mol CO /mol Pt)	0.22	0.26	0.61	0.28
Glycerol STY /10^{-2} mol mol^{-1} s^{-1}	7.6	0.3	13.2	41.5
Glycerol (STY_{PtM}/ STY_{Pt})	1.0	0.3	1.7	5.5
Carbon Conversion	4.8%	4.4%	13.3%	7.4%
CO_2/alkanes	27.1	19.7	3.5	23.6
H_2/CO_2	3.0	9.4	1.7	1.7
H_2 Selectivity	95%	98%	62%	91%
[1,3-PDO]/[1,2-PDO]	0.05	0.01	0.16	0.09
[C-C]/[C-O] scission	0.59	0.13	0.29	0.52
Product selectivity				
[C-O] scission	29%	84%	35%	39%
[C-C] scission	17%	11%	10%	20%
Acids	0%	1%	4%	1%
CO	0%	0%	0%	0%
CO_2	52%	4%	39%	39%
CH_4	2%	0%	3%	1%
C_2H_6	--	0%	8%	1%

3.4.2 Scanning Transmission electron microscopy

STEM images for PtRe/MWCNT shown in Figure 3.3 show the transparent multiwalled carbon nanotubes with a broad distribution of metal particle sizes, including several larger agglomerates on the order of 50 to 100 nm (Figure 3.3B) and mostly smaller particles in the range of 2 to 4 nm (Figures 3.3E and 3.3F). The low density of metal particles is expected due to the lower surface area of the MWCNT support (233 $m^2 g^{-1}$) compared to typical activated carbons such as Norit-SX1G (1000 $m^2 g^{-1}$). Also, due to the use of as-received MWCNT without an oxidizing acid treatment, all particles are deposited on the external surface area of the nanotubes, as has been established in literature by TEM studies [39]. The PtRe/C STEM images in Figure 3.4 show a high metal particle density on this high surface area porous support, such that some particles even remain hidden in the porous carbon material. The metal particle sizes are also more uniform than PtRe/MWCNT and range between 1 and 2 nm (Figures 3.4E and 3.4F), with no metal agglomerates larger than 5 nm. These smaller particle sizes of PtRe/C compared to PtRe/MWCNT correspond to the higher metal dispersion measured by CO chemisorption (61.2 % versus 27.9 % dispersion).

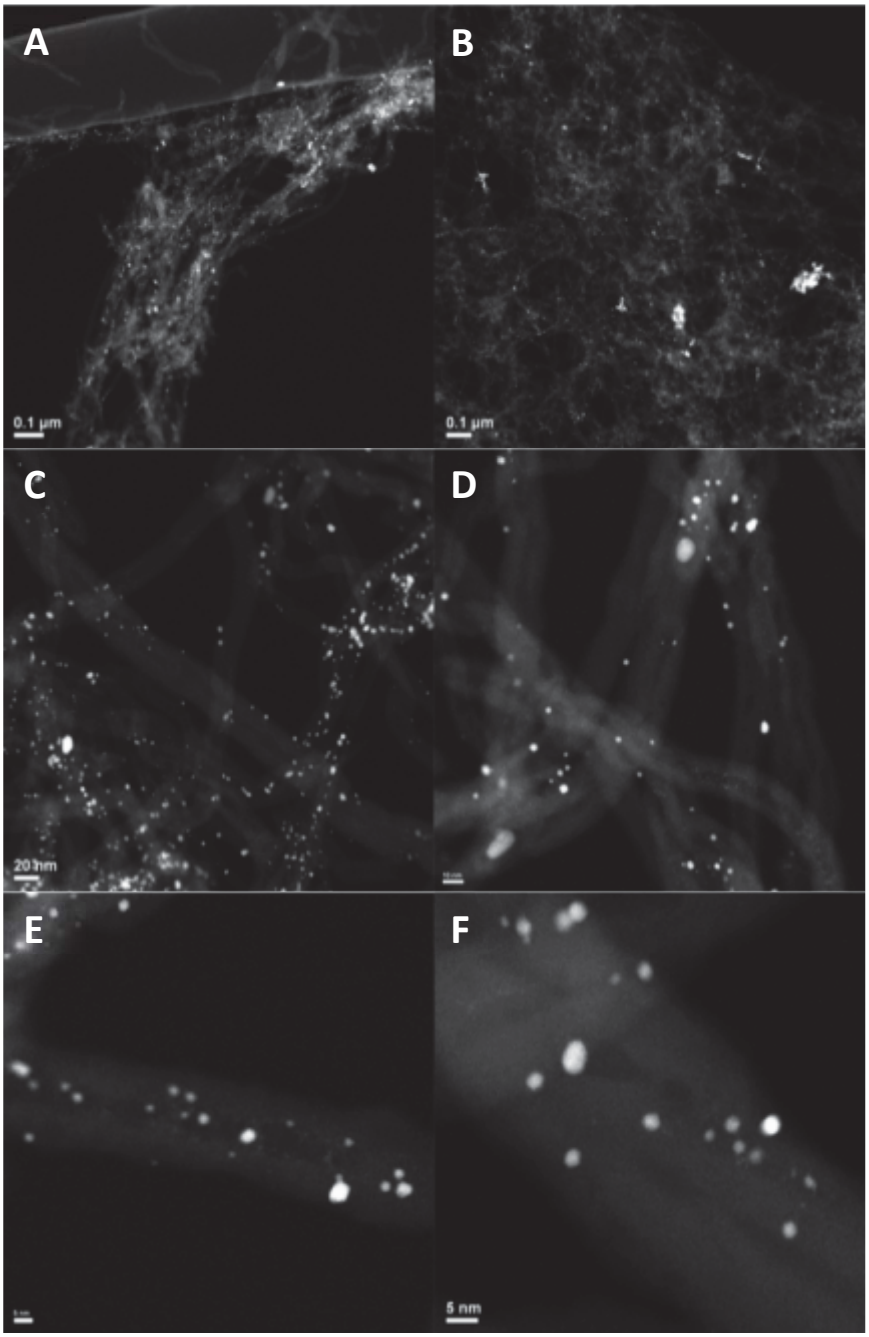

Figure 3.3 Representative STEM images of PtRe/MWCNT after glycerol APR for at least 5 days reaction time.

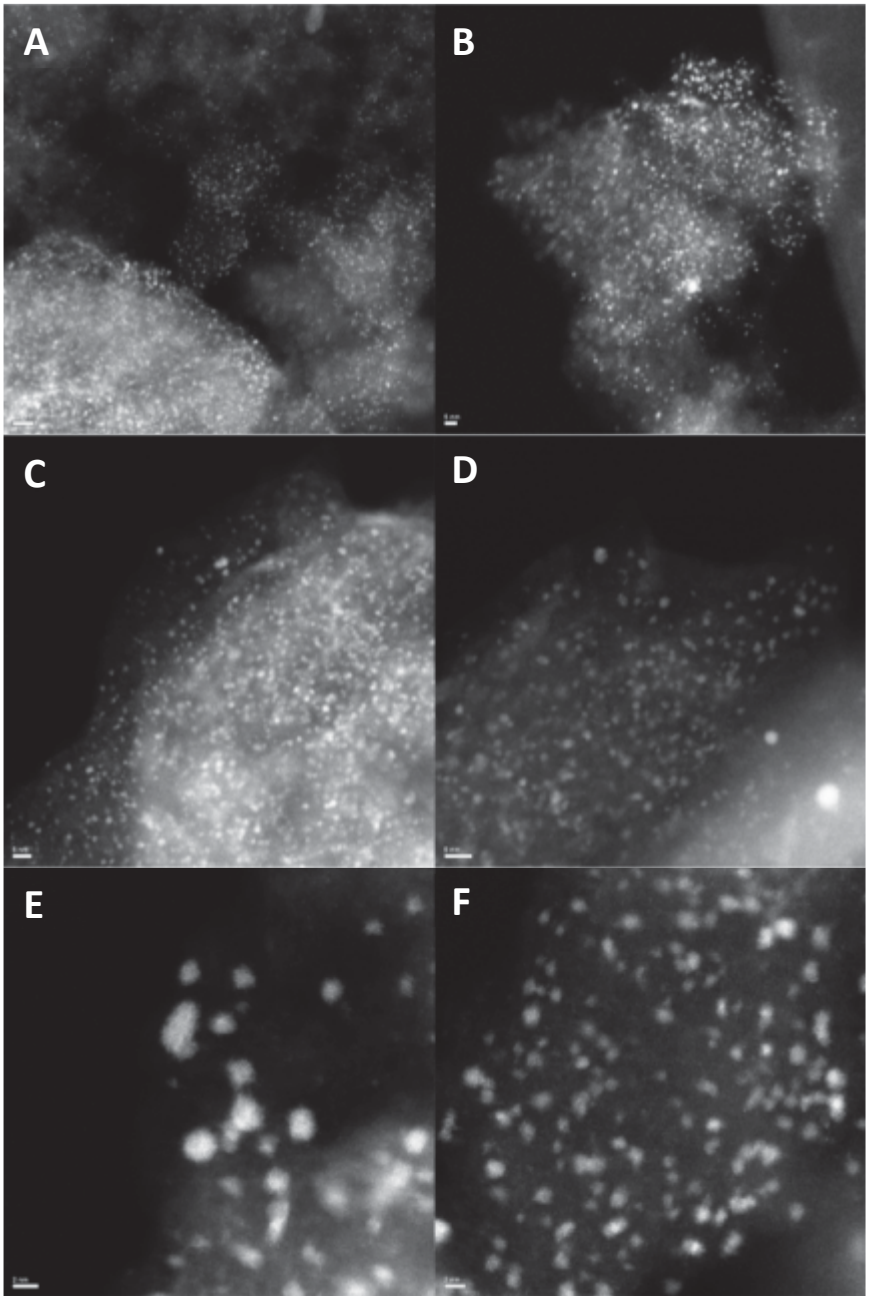

Figure 3.4 Representative STEM images of PtRe/C after glycerol APR for at least 5 days reaction time.

3.4.3 EELS elemental mapping

In order to determine the local metal distribution on each PtRe catalyst, EELS maps were produced for Pt and Re distribution in individual metal particles of the used catalyst samples. This mapping is especially important given that EXAFS analysis for PtRe catalysts cannot determine the amount of alloying from mixed metal scatters as has been done for promoted Pt catalysts with 3d and 4d transition metals. For PtRe/MWCNT the maps in Figure 3.5 show several 2-7 nm well-defined particles that all contain a mixture of Pt and Re metal. Some particles appear to be Pt-rich and some Re-rich with no easily discernable preferred configuration of metal distribution, either in a core-shell configuration or homogeneous mixed alloy.

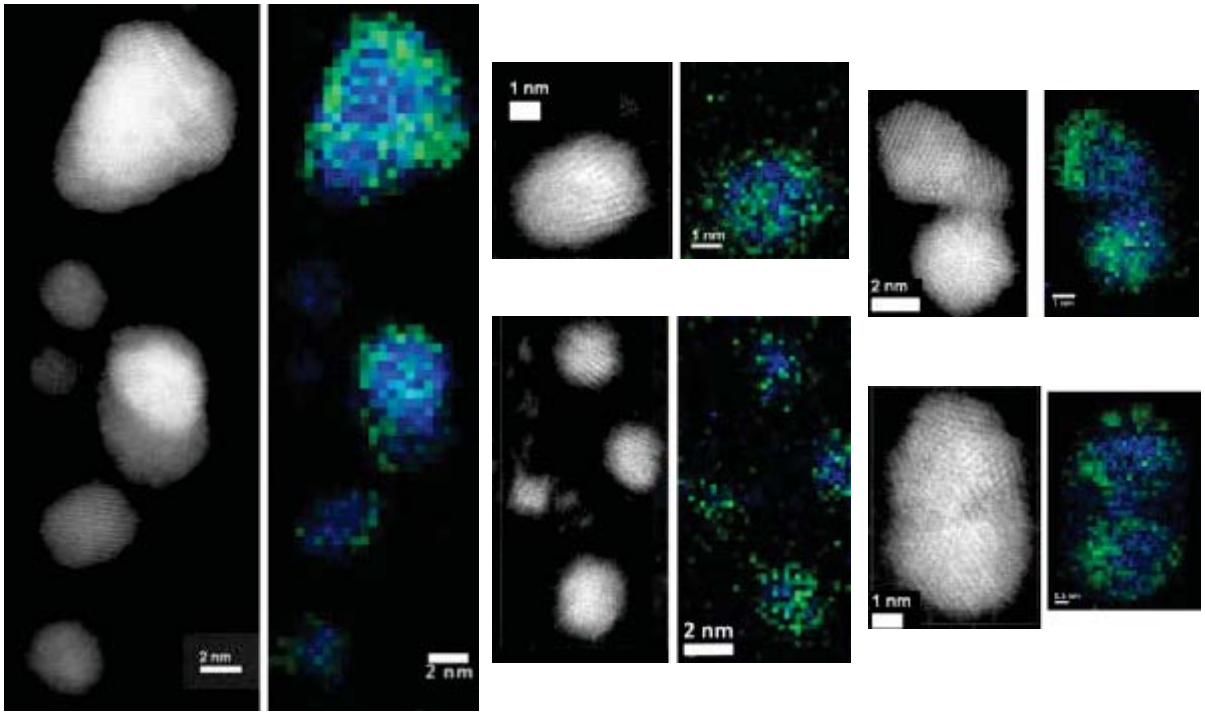

Figure 3.5 Representative STEM-EELS elemental maps at the Pt $M_{4,5}$ edges (green) and Re $M_{4,5}$ edges (blue) for nanoparticles on PtRe/MWCNT after glycerol APR for at least 5 days reaction time.

The EELS maps of PtRe/C after glycerol APR in Figure 3.6 are smaller particles of around 2 nm in size for which the metal distribution does not form well-defined particle borders. Specifically, while the Pt metal corresponds to the easily identifiable metal particles in the STEM images, the Re metal is both mixed with the metal particles and dispersed over the carbon support to a greater extent than for PtRe/MWCNT.

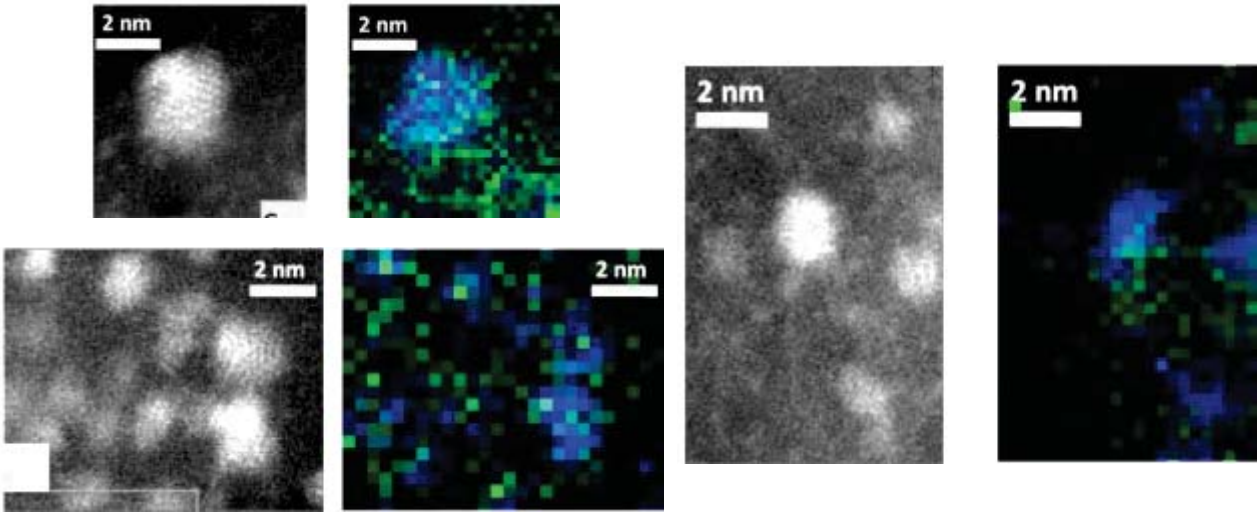

Figure 3.6 Representative STEM-EELS elemental maps at the Pt $M_{4,5}$ edges (green) and Re $M_{4,5}$ edges (blue) for nanoparticles on PtRe/C after glycerol APR for at least 5 days reaction time.

3.4.4 X-ray absorption spectroscopy

3.4.4.1 EXAFS

The bimetallic PtRe catalysts were characterized *ex situ* and in *operando* by x-ray absorption spectroscopy at the Pt L_{III} edge (11.564 keV) and Re L_{III} edge (10.535 keV). The extended x-ray absorption fine structure (EXAFS) of the Pt L_{III} edge in Figure 3.7 of both bimetallic catalysts shows that the PtRe/C catalyst has lower Pt-M coordination than PtRe/MWCNT both after reduction and during glycerol APR reaction. There is also a shift in the metal Pt-M peak to lower bond distance compared to the reference Pt foil. This is confirmed quantitatively in the EXAFS fits in Table 3.2 for both PtRe/MWCNT (0.03-0.04 Å shift) and PtRe/C (0.04-0.07 Å shift), and this bond distance contraction is characteristic of small metal nanoparticles [40]. The Pt-M peak for PtRe/MWCNT has become lower in intensity during *operando* measurements, but due to the broadening

effect of elevated temperatures on the EXAFS (increased Debye-Waller factor), this does not mean a decrease in the coordination number. For PtRe/C the Pt-M peak increases during *operando* measurement which means that there is an increase in the Pt-M coordination, and this effect is great enough to overcome the effect of any broadening due to taking spectra at high temperature. For both sets of spectra, there appears no evidence of any Pt-O coordination during the APR reaction, indicating that Pt stays primarily reduced, which is supported by the XANES spectra.

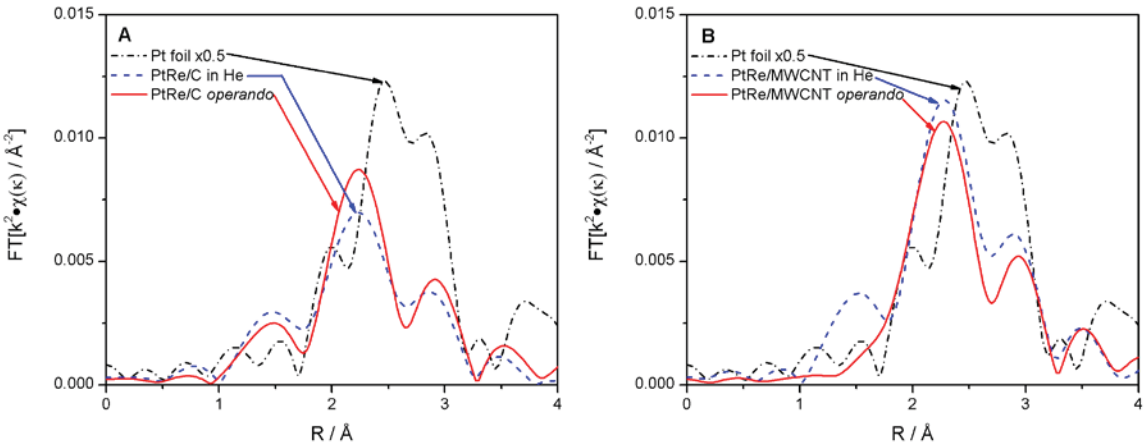

Figure 3.7 Magnitude of the FT of the Pt L_{III} edge k^2-weighted EXAFS of the (A) PtRe/C and (B) PtRe/MWCNT catalysts after reduction at 450 °C (blue, dash) and in *operando* (red, solid) as compared to reference Pt foil (black, dash/dot). *Operando* conditions were 230 °C, 32 bar, and 10 wt% aqueous glycerol feed.

The EXAFS of Re L_{III} edge data for both PtRe catalysts in Figure 3.8 indicates that both catalysts contain only Re-M coordination after reduction at 450 °C. This absence of oxygen coordination does not occur with a monometallic Re/MWCNT catalyst reduced at the same temperature (see Table 3.2), as Pt can facilitate reduction of a more oxophillic metal in alloy catalysts. As in the Pt EXAFS, the PtRe/MWCNT catalyst has higher Re-M intensity corresponding to larger particles. Also similar to Pt there is a contraction in

the Re-M bond length for both both PtRe/MWCNT (0.03-0.04 Å shift) and PtRe/C (0.07-0.08 Å shift) as seen in Table 3.2. The major difference in the two bimetallic catalysts occurs during reaction, when we see the *operando* spectrum of PtRe/C gain a Re-O peak at lower bond lengths (1.99 Å) and a decrease the existing Re-M peak. PtRe/MWCNT does not see this change, but instead sees a slight decrease in Re-M intensity that may be only due to the temperature effect.

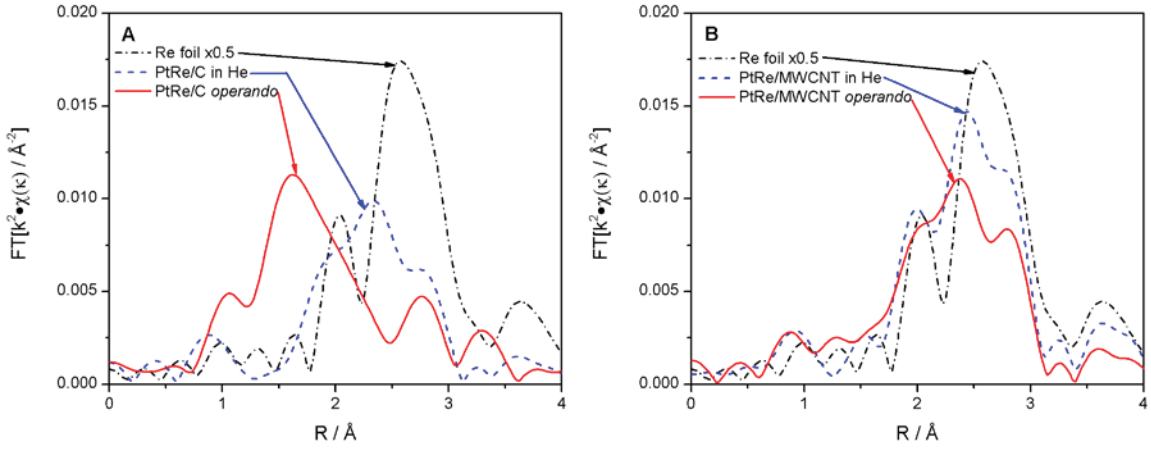

Figure 3.8 Magnitude of the FT of the Re L_{III} edge k^2-weighted EXAFS of the (A) PtRe/C and (B) PtRe/MWCNT catalysts after reduction at 450 °C (blue, dash) and in *operando* (red, solid) as compared to reference Pt foil (black, dash/dot). *Operando* conditions were 230 °C, 32 bar, and 10 wt% aqueous glycerol feed.

Table 3.2 EXAFS results for catalyst samples and reference materials.

Catalyst	Treatment	Edge energy (keV)	Absorber - Backscatter	N	R (Å)	$\Delta\sigma^2$ (10^{-3} Å^2)	E_0 shift (eV)	residual (%)
Pt L_{III} Edge								
Pt Foil	--	11.5640	Pt-Pt	12.0	2.77			
5% Pt/MWCNT	Reduced at 400 °C, in He at RT	11.5637	Pt-M	7.8	2.74	2	-1.2	8.0
5% Pt, 4.8% Re /MWCNT	Reduced at 450 °C, in He at RT	11.5645	Pt-M	8.0	2.73	2	-0.3	6.9
	Operando - 230 °C, 32 bar, 10 wt% aqueous glycerol	11.5647	Pt-M	9.9	2.74	5	-0.2	8.8
5% Pt, 4.8% Re/C	Reduced at 450 °C, in He at RT	11.5643	Pt-M	5.3	2.70	3	-1.9	7.4
	Operando - 230 °C, 32 bar, 10 wt% aqueous glycerol	11.5644	Pt-M	8.6	2.73	6	-1.2	6.2
Re L_{III} Edge								
Re Foil	--	10.5350	Re-Re	12.0	2.75			
ReO_2	--	10.5363	Re-O	6.0	1.98			
5% Re/MWCNT	Reduced at 450 °C, in He at RT	10.5370	Re-Re Re-O	7.0 0.7	2.69 1.81	3 1	-5.6 -17.0	17.1
5% Pt, 4.8% Re /MWCNT	Reduced at 450 °C, in He at RT	10.5366	Re-M	7.7	2.72	2	-1.4	8.5
	Operando - 230 °C, 32 bar, 10 wt% aqueous glycerol	10.5367	Re-M	9.1	2.71	5	-2.1	10.6
5% Pt, 4.8% Re/C	Reduced at 450 °C, in He at RT	10.5366	Re-M	5.8	2.67	3	-4.3	15.6
	Operando - 230 °C, 32 bar, 10 wt% aqueous glycerol	10.5374	Re-M Re-O	4.9 2.1	2.68 1.99	6 1	-6.4 2.5	17.4

3.4.4.2 XANES

For both Pt L_{III} and Re L_{III} metal edges, the x-ray absorption near edge spectrum (XANES) was used to characterize the oxidation state and the effect of surface adsorbates on the PtRe catalysts. In Figure 3.9 there is a small shift in the whiteline intensity and edge position of both catalysts during the reaction when compared to the spectra collected in He. For the Re L_{III} edge of PtRe/C this change is likely because of oxidation of the metal, in agreement with the EXAFS which show Re-O coordination. For Re L_{III} edge of PtRe/MWCNT and the Pt L_{III} edge of both catalysts the shift more likely to be due to surface adsorbates, since no Pt-O or Re-O was detected and the shifts are much smaller.

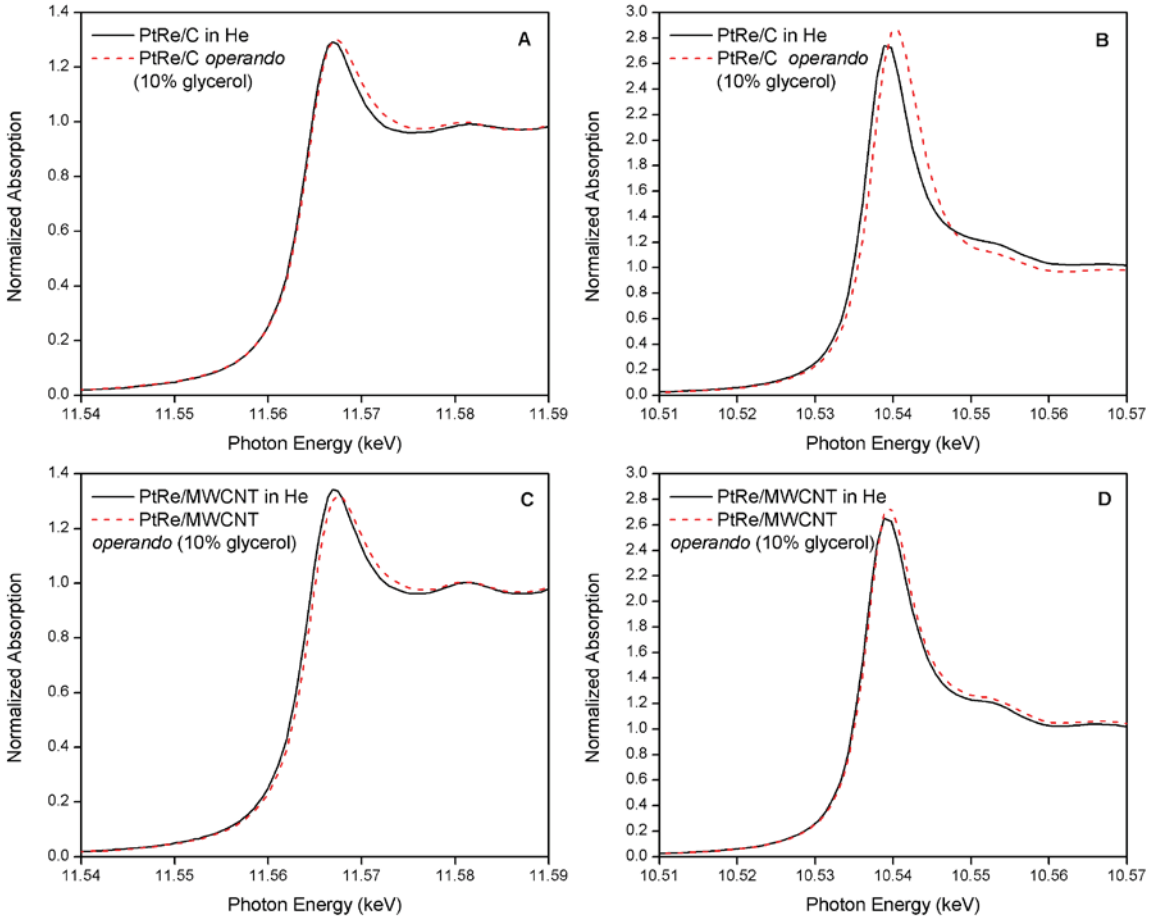

Figure 3.9 XANES spectra of the Pt L_{III} edge (A and C) and Re L_{III} edge of the bimetallic PtRe catalysts in He (black, solid) and in *operando* (red, dashed). Edge positions of all spectra are shown in Table 3.2.

Subtracting the spectrum collected in He for PtRe/MWCNT from the same catalyst after room temperature chemisorption with CO, H_2 and H_2O yields a difference spectrum (ΔXANES) for each gas corresponding to the relative changes in the whiteline intensity of both Pt L_{III} and Re L_{III} edges when these molecules are adsorbed to the metal surface. This electronic effect due to different bonding of the adsorbates can be compared to a similar difference spectrum for the *operando* XANES to identify the most abundant surface species. Figure 3.10C shows that the Pt ΔXANES for all conditions matches the

signature characteristic of adsorbed CO. Also, the relative intensity of that signature increases from 5 % glycerol APR to 30 % glycerol APR to WGS, suggesting that WGS has the highest relative amount of Pt-CO. This increasing Pt-CO corresponds to decreasing water partial pressure, which is a reactant needed for the WGS reaction to remove CO from the metal surface. The corresponding Re ΔXANES for PtRe/MWCNT under all *operando* conditions in Figure 3.10D matches the characteristic of adsorbed H_2. Because of the weakness of the H_2 signature at the Re L_{III} edge, it is difficult to conclude whether there is any significant difference in quantity of Pt-H under *operando* conditions.

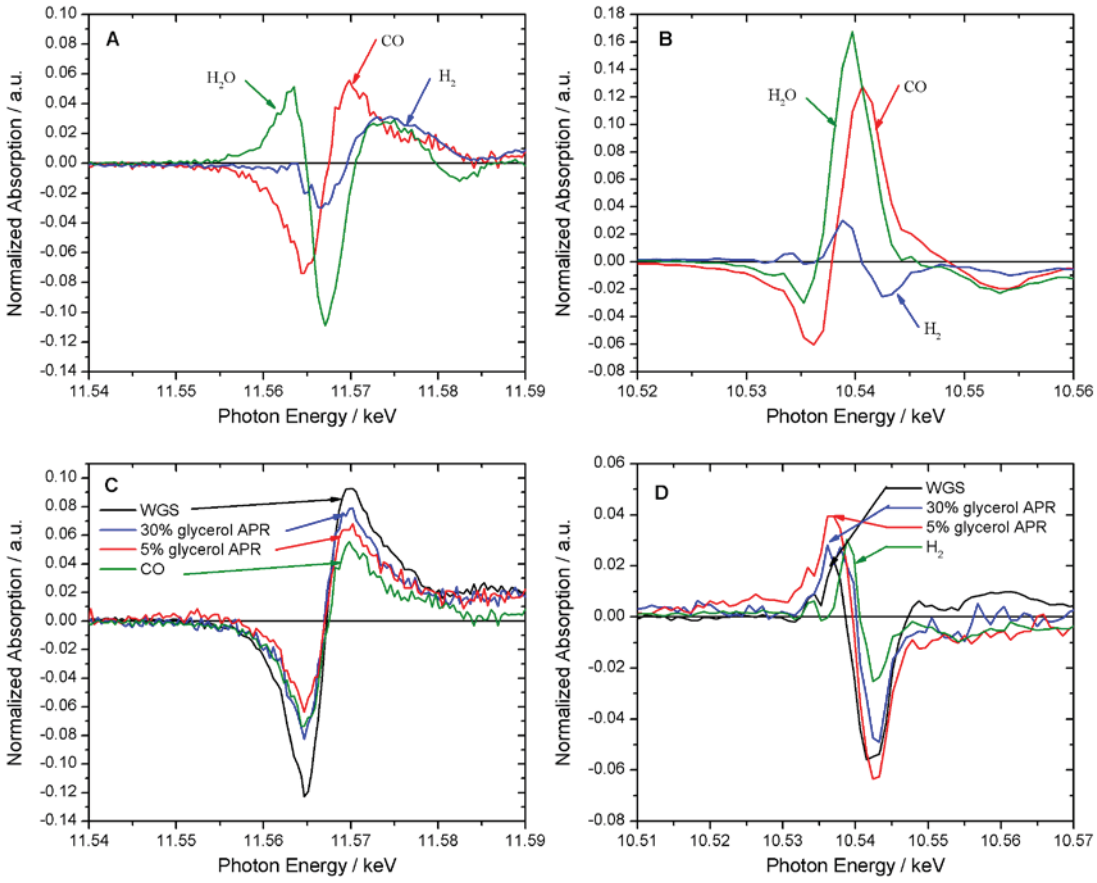

Figure 3.10 XANES spectra for PtRe/MWCNT saturated with adsorbed gases (CO, H_2, H_2O) at room temperature for the Pt L_{III} edge (A) and Re L_{III} edge (B). *Operando* XANES spectra of PtRe/MWCNT at various reaction conditions are shown for Pt L_{III} edge (C) and Re L_{III} edge (D).

A similar *operando* ΔXANES analysis was performed for PtRe/C during glycerol APR (10 wt% aqueous glycerol feed) with the resultant spectra displayed in Figure 3.11. The adsorbed gas signatures for the Pt L_{III} edge in Figure 3.11A are very similar shapes to those of PtRe/C in Figure 3.10A. The intensity of the signal is increased for PtRe/C, particularly for adsorbed CO, due to the higher dispersion of this catalyst. A higher percentage of surface Pt atoms on the metal particles will result in more change in the XANES whiteline intensity from Pt-CO bonding. During *operando* glycerol APR there is a ΔXANES signature of similar shape and slightly lower intensity than CO adsorption ΔXANES, such that this is the most abundant adsorbate on surface Pt during the reaction. For the Re L_{III} edge, we find different ΔXANES signatures for adsorbed gases on PtRe/C in Figure 3.11B compared to the same conditions for PtRe/MWCNT in Figure 3.10B. This is not unlikely if the metal distribution is different and amount of alloy formed is also different (Re clusters versus PtRe alloy particles). The glycerol APR *operando* ΔXANES in Figure 3.11D shows a signature of the same shape but a much larger intensity than that of adsorbed H_2. Using the evidence from EXAFS that the working PtRe/C catalyst has partially oxidized Re, an additional Re ΔXANES spectrum was generated for PtRe/C which was passivated in air at room temperature after reduction. This difference spectrum is very strong due to the increase in whiteline intensity that comes with oxidation of Re metal. So the *operando* ΔXANES spectrum is dominated by the whiteline change due to oxidation, masking the small changes that may come from surface adsorbates on Re sites.

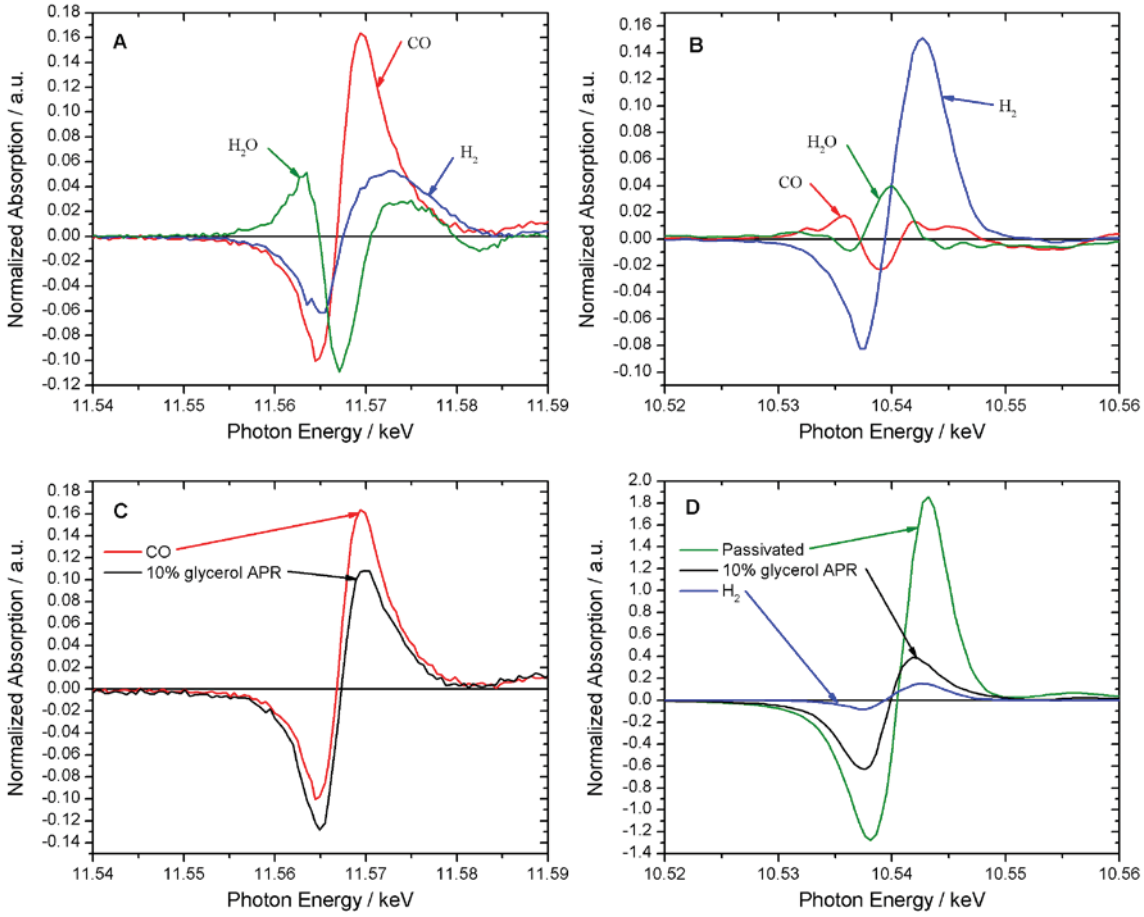

Figure 3.11 XANES spectra for PtRe/MWCNT saturated with adsorbed gases (CO, H_2, H_2O) at room temperature for the Pt L_{III} edge (A) and Re L_{III} edge (B). *Operando* XANES spectra of PtRe/MWCNT at various reaction conditions are shown for Pt L_{III} edge (C) and Re L_{III} edge (D).

3.5 Discussion

3.5.1 Structural differences between PtRe catalysts

The structure of bimetallic supported metal catalysts will depend upon the metal deposition method, support material used, catalyst pretreatment, and reaction environment. In this study, we investigated the differences between two kinds of carbon supports (MWCNT and activated carbon) and also changed reaction conditions for *operando* XAS analysis. The as-received multiwalled carbon nanotubes used in this

study have graphitic surfaces with few anchoring points on which metal salts can deposit and metal particles can nucleate and grow during reduction in hydrogen. Therefore, these materials are used as catalyst supports in literature typically after an oxidizing treatment in refluxing nitric acid to create surface oxygen-containing groups [37, 38]. The functionalized surface is able to maintain high dispersion of metal nanoparticles compared to the bare nanotubes. Activated carbon, which is much higher surface area and has an amorphous non-graphitic structure with many defects and surface oxygen groups already tends to provide high metal dispersion compared to bare carbon nanotubes. EXAFS characterization of the bimetallic PtRe structure of both catalysts indicates that there is no strong preference to core-shell segregation for the bimetallic particles. This is due to the fact that Pt-M and Re-M coordination numbers are similar in the reduced PtRe/MWCNT catalyst (N_{Pt-M} = 8.0, N_{Re-M} = 7.7) and reduced PtRe/C catalyst (N_{Pt-M} = 5.3, N_{Re-M} = 5.8). The evidence that Pt and Re are indeed forming alloy particles cannot be extracted from EXAFS. It instead comes from the shift in edge energy and white line intensity of the Pt L_{III} and Re L_{III} XANES and in the EELS maps of used catalyst which show mixing of Pt and Re in individual metal particles. During glycerol APR, *operando* measurements show that there is some sintering of metal particles as the Pt-M increases for both catalysts. However, the Re-M increases for PtRe/MWCNT in support of sintering, while Re-M decreases and Re-O appears for PtRe/C in support of oxidation of Re to ReO_x or Re-OH. This change affects the acidity of the catalyst, as discussed later. EELS elemental maps show that Re is dispersed over the activated carbon support in addition to alloying with Pt particles. So in the oxidizing conditions of glycerol APR this isolated Re is likely to be oxidized without the help of Pt noble metal to keep it reduced.

Also, while the increase both metal coordination numbers indicate particle sintering for PtRe/MWCNT, there is a larger increase in N_{Pt-M} to 9.9 compared to N_{Re-M} to 9.1. This lower coordination environment of Re under reaction conditions would occur if Re has tendency to phase segregate to the surface of bimetallic particles under reaction conditions. Given the oxophillic nature of Re, it is reasonable that this would occur in the hot aqueous conditions of APR similar to Mo in PtMo/C catalysts [24]. So, while there was no Re-O scatter in the *operando* spectrum for PtRe/MWCNT, it is possible that a small amount of Re metal oxidized to ReO_x or Re-OH as it assists in water dissociation for the water-gas shift reaction. The EELS elemental maps support this view of most Re remaining reduced because the location of Re is primarily within well-defined alloy particles for PtRe/MWCNT, instead of dispersed throughout the support surface as the Re on PtRe/C. Any small amount of oxidized Re is likely to be just at the surface of bimetallic particles. The difficulty in quantifying the small amount of oxidized Re from XANES comes from the fact that both alloy formation and oxidation can result in shifts in the whiteline intensity and Re L_{III} edge energy, and both of these effects change in the working catalyst as compared to the reduced catalyst in He.

3.5.2 Catalyst surface species and reaction selectivity

The primary surface adsorbate for surface Pt sites of both PtRe/C and PtRe/MWCNT catalysts in *operando* is CO for both WGS and glycerol APR at several different feed concentrations. For PtRe/MWCNT the Pt L_{III} ΔXANES has a stronger signature for all *operando* conditions than that of CO adsorbed at room temperature. A possible explanation of why there could be more adsorbed CO on Pt during reaction than after room temperature saturation is the high pressure conditions of glycerol APR (32 bar total

pressure), increasing the coverage of CO beyond that which occurs at ambient pressure. Also, there could be some amount of surface segregation of Pt during the reaction, which is more likely for the WGS reaction since its more reducing conditions are less likely to oxidize Re and cause it to segregate to the particle surface. The trend of increasing ΔXANES intensity from 5 % glycerol APR to 30 % glycerol APR to WGS also corresponds to the decrease in water partial pressure among these three reaction conditions. If water partial pressure is decreased, the WGS reaction rate should decrease and there should consequently be a higher coverage of CO on the metal surface, in agreement with the results. The ΔXANES for the Re L_{III} edge of the two PtRe catalysts differ substantially, and add to the picture of the working catalyst derived from EXAFS and EELS analysis. For the PtRe/MWCNT catalyst, all *operando* conditions result in primarily hydrogen adsorbed on Re from ΔXANES. This supports the view that Re addition to Pt catalysts allow for a bifunctional site for which glycerol decomposition occurs on the Pt sites (or CO adsorption during WGS), and Re assists in water dissociation which can react with CO adsorbed on Pt sites. The fact that Re ΔXANES matches adsorbed hydrogen may be due to water dissociation being a rate limiting step. If that is the case, we would expect that water is non-equilibrated and surface OH is reacting with CO faster than it is replaced, leaving adsorbed H from the water dissociation.

PtRe/C displays *operando* Re L_{III} ΔXANES which match the shape of both H_2 and an air passivated catalyst. Since the EXAFS indicate Re-O coordination, it appears that oxidation of Re occurs during reaction. Upon oxidation by water during glycerol APR, there will be created Re-OH sites with Brønsted acidity. Thus, a structural difference

between the PtRe catalysts in *operando* explains the origin of high C-O bond scission relative to C-C bond scission for PtRe/C, and the consequential low hydrogen selectivity of this catalyst.

3.6 Conclusions

The differences in rates and selectivity between the two similar catalysts PtRe/MWCNT and PtRe/C can be explained in terms of metal distribution. Comparing the reduced catalyst EXAFS and XANES to those collected in *operando*, we find that PtRe/MWCNT contained larger alloyed particles which sinter slightly during glycerol APR. The Re metal remains primarily reduced and the most prevalent surface adsorbates are CO and H for Pt and Re sites, respectively, during both WGS and APR reactions. For the smaller metal particles in PtRe/C, the Re oxidizes to form acid sites to open up dehydration/hydrogenation routes to C-O bond scission. EELS maps of individual particles of both catalysts confirm on a local level that while Re remains well mixed with Pt in PtRe/MWCNT, the Re metal is well dispersed on the high surface are activated carbon support of PtRe/C, allowing easy oxidation under reaction conditions. In this case where high rates of hydrogen production by glycerol APR are desired, the PtRe/MWCNT catalyst was able to obtain higher rate promotion and maintain higher C-C bond scission selectivity compared to PtRe/C due to the differences in metal distribution. These insights in metal distribution both of the used catalyst and the working catalyst (*operando*) for PtRe can inform future efforts to design bifunctional metal catalysts for selective bond breaking when different support materials and reaction environments are considered.

CHAPTER 4. EFFECT OF ALCOHOL AND ALKYL GROUP POSITION ON THE RATE AND SELECTIVITY OF AQUEOUS PHASE REFORMING REACTIONS

4.1 Introduction

For conversion of biomass into useful chemicals, several promising routes have been explored by experiments. These include pyrolysis followed by catalytic deoxygenation (by hydrodeoxygenation or decarbonylation) [33], and direct catalytic conversion via aqueous phase reforming (APR) to alkanes and monofunctional alcohols [41]. To simplify the complexity of biomass reactivity studies for catalytic processes, model compounds have been used extensively in literature. Glycerol is a good model compound for the cellulose fraction of biomass due to its C:O stoichiometry of 1:1 which is common to all carbohydrate molecules. However, a real biomass stream will contain many different compounds, including those with different C:O ratios and additional saturated and unsaturated hydrocarbon fragments. Also, the APR reaction network generates many liquid phase intermediate products, and so it is important to understand the reactivity of these intermediates and selectivity towards [C-O] and [C-C] bond scission so that catalyst design can address challenges and exploit opportunities of the various reactant molecules. Unfortunately, the number of studies in literature which address the effects of different functional groups and their positions during aqueous phase reforming are relatively few [42, 43]. There have been some additional surface science studies and density functional

theory (DFT) studies on the decomposition of simple oxygenate molecules [44-47], and it is of interest to see if the conclusions drawn in these works are borne out experimentally in APR over high surface area catalysts.

In the current study we present work addressing how the position of alcohol and alkyl groups affects the reaction rates and pathway selectivity of a Pt catalyst supported on multi-walled carbon nanotubes (MWCNT). The rates and selectivity for the conversion of C3 alcohols with varying position of the alcohol and alkyl functional groups are collected to directly compare rates and the analysis of the parallel reaction pathways is performed to quantify the initial [C-C] and [C-O] bond scission selectivity. The experimental results are then compared to results of predicted bond scission selectivities derived from Bronsted-Evans-Polanyi (BEP) linear scaling relationships and density function theory (DFT) calculations of the predicted activation barriers to bond breaking on Pt (111) surface. These predictions agree well with experiment for all cases except 1,3-propanediol reforming.

4.2 Experimental

4.2.1 Catalyst synthesis

The catalyst for this study was monometallic Pt supported on multi-walled carbon nanotubes (MWCNT). Before metal deposition, the MWCNT were treated by refluxing in concentrated nitric acid (69 wt%) for 4 hours at 121 °C to add oxygen functional groups to the surface and remove the Ni nanotube synthesis catalyst. Afterwards, the nanotubes were washed ten times with water by centrifugation and decanting and dried at 150 °C in air overnight. The Pt was loaded by incipient wetness impregnation of the MWCNT by an aqueous solution of tetraammineplatinum(II) nitrate (Sigma Aldrich) at

an appropriate concentration to give a 5 wt% Pt loading. The wet catalyst was dried at 150 °C overnight, and before running the reactions Pt/MWCNT was reduced *in situ* under 45 sccm of 4% H_2/Ar with a 2 hour ramp and 2 hour soak at 400 °C.

4.2.2 Aqueous phase reforming kinetics

Aqueous phase reforming reaction studies were performed in a fixed bed reactor using a 10 mm × 4 mm × 200 mm (OD × ID × L) Sigradur glassy carbon tube (Hochtemperatur-Werkstoffe GmbH) as the reactor. The reactor was connected to the feed and effluent lines using standard Swagelok fittings and graphite ferrules. The catalyst bed was held in place by plugs of quartz wool and mesh frits spot welded to the end of short 1/16" stainless steel rods. The mass of catalyst loaded for each experiment was between 60 and 100 mg. The reactor was heated by an aluminum heating block with cartridge heaters, the design of which was described in a previous publication [16]. The catalyst bed temperature was monitored and controlled with a PID temperature controller (Eurotherm) reading from a K-type thermocouple (Omega) inserted into the reactor at the top of the catalyst bed. System pressure was controlled by a dual phase back pressure regulator (Equilibar).

The reforming experiments were conducted at 230 °C and 32 bar with an aqueous feed of the reactant alcohol. Feed concentrations were 30 wt% for glycerol (>99%, Sigma Alrdich), 26.2 wt% for 1,2-propanediol (>99.5%, Sigma Aldrich) and 1,3-propanediol (98%, Sigma Aldrich), 22.1 wt% for 1-propanol (99.7%, Sigma Aldrich), and 17.7 wt% for ethanol (99.5% Koptec). These feed concentrations were all equal to 0.077 mole fraction alcohol in order to make accurate rate comparisons between different feeds. The feed solution was pumped into the reactor in an up flow configuration with a syringe

pump (Teledyne ISCO 100DM). Flow rates were varied to give weight hourly space velocities (WHSV, $g_{alcohol} \bullet g_{catalyst}^{-1} \bullet hr^{-1}$) between 0.17 hr^{-1} and 150 hr^{-1} to vary reactant conversion.

Gas phase products were collected with a constant flow rate of Ar sweep gas introduced directly before the backpressure regulator. From a gas liquid phase separator, the gas stream was then sampled by two online gas chromatographs (Agilent 6890 and 7890) equipped with packed columns (Carboxen 1000) and thermal conductivity detectors with He or N_2 carrier gases for quantification of carbon species (CO_x, hydrocarbons) and H_2, respectively. Liquid phase products were collected by draining the phase separator at regular intervals and analyzing the products by an offline GC (Agilent 7890) with a capillary column (Agilent DB-WAX) and a flame ionization detector. System mass balances and carbon balances generally closed to within 100 ± 3 % and 100 ± 5 %, respectively.

Reaction rates (r_x, where 'x' is either the reactant or product, e.g. $r_{glycerol}$ is the glycerol rate) are defined as site time yields (STY), which are normalized to the surface sites as measured by CO chemisorption. Carbon selectivity is defined as [($r_{product}$ × product carbon number) × ($r_{reactant}$ × reactant carbon number)$^{-1}$ × 100%]. The carbon selectivity is calculated with respect to all products in both the liquid and gas phase, and will sum to 100 % across all carbon-containing products.

4.2.3 Density functional theory calculations

Periodic density function theory (DFT) calculations were carried out on Pt fcc (111) surface. BEP relationships were used to estimate the activation barriers for [C-O] and [C-C] bond scission reactions of each lowest energy sequentially dehydrogenated alcohol

intermediate. The kinetic barriers for each reaction, along with the binding energy of dehydrogenated intermediates were used to create free energy diagrams in order to compare relative selectivity towards [C-C], [C-O], [C-H], and [O-H] at each progressive dehydrogenation step of each alcohol. This method was developed and described in detail in previous publications [48, 49].

4.3 Results

4.3.1 Aqueous phase reforming

Reaction rates and product distributions for glycerol, 1,2-propanediol, 1,3-propanediol, 1-propanol, and ethanol were measured on a Pt/MWCNT catalyst. The products measured for each of the reactants were similar and always consisted of a subgroup of glycerol reforming products. Table 4.1 lists the products in the effluent streams for each of the feed molecules, with liquid products listed in descending order of concentration.

Table 4.1 Identified and quantified reaction products for aqueous phase reforming reactions of glycerol, 1,2-propanediol, 1,3-propanediol, 1-propanol, and ethanol.

Glycerol	1,2-Propanediol	1,3-Propanediol	1-Propanol	Ethanol
Liquid Phase Products				
Ethylene Glycol (EG) 1,2-Propanediol (PG) Hydroxyacetone (HA) Methanol (MeOH) Ethanol (EtOH) 1-Propanol (1-PrOH) 1,3-Propanediol (1,3-PDO) Acetaldehyde (AcO) Acetone 2-Propanol (2-PrOH) Propionaldehyde (PrO)	Hydroxyacetone Ethanol 1-Propanol Acetaldehyde Propionic Acid Propionaldehyde Acetone 2-Propanol	1-Propanol Ethanol Propionic Acid Propionaldehyde Methanol Acetaldehyde	Propionaldehyde Propionic Acid Methanol	Acetaldehyde Methanol
Gas Phase Products				
Hydrogen Carbon Dioxide Methane Ethane Carbon Monoxide	Hydrogen Carbon Dioxide Methane Ethane Carbon Monoxide	Hydrogen Carbon Dioxide Methane Ethane Carbon Monoxide	Hydrogen Carbon Dioxide Ethane Carbon Monoxide	Hydrogen Carbon Dioxide Methane Ethane Carbon Monoxide

The carbon selectivity to reaction products listed in Table 4.1 for each of the feed molecules as a function of conversion are presented in Figures 4.1 through 4.5 for glycerol, propylene glycol (PG), 1,3-propanediol, 1-propanol, and ethanol, respectively.

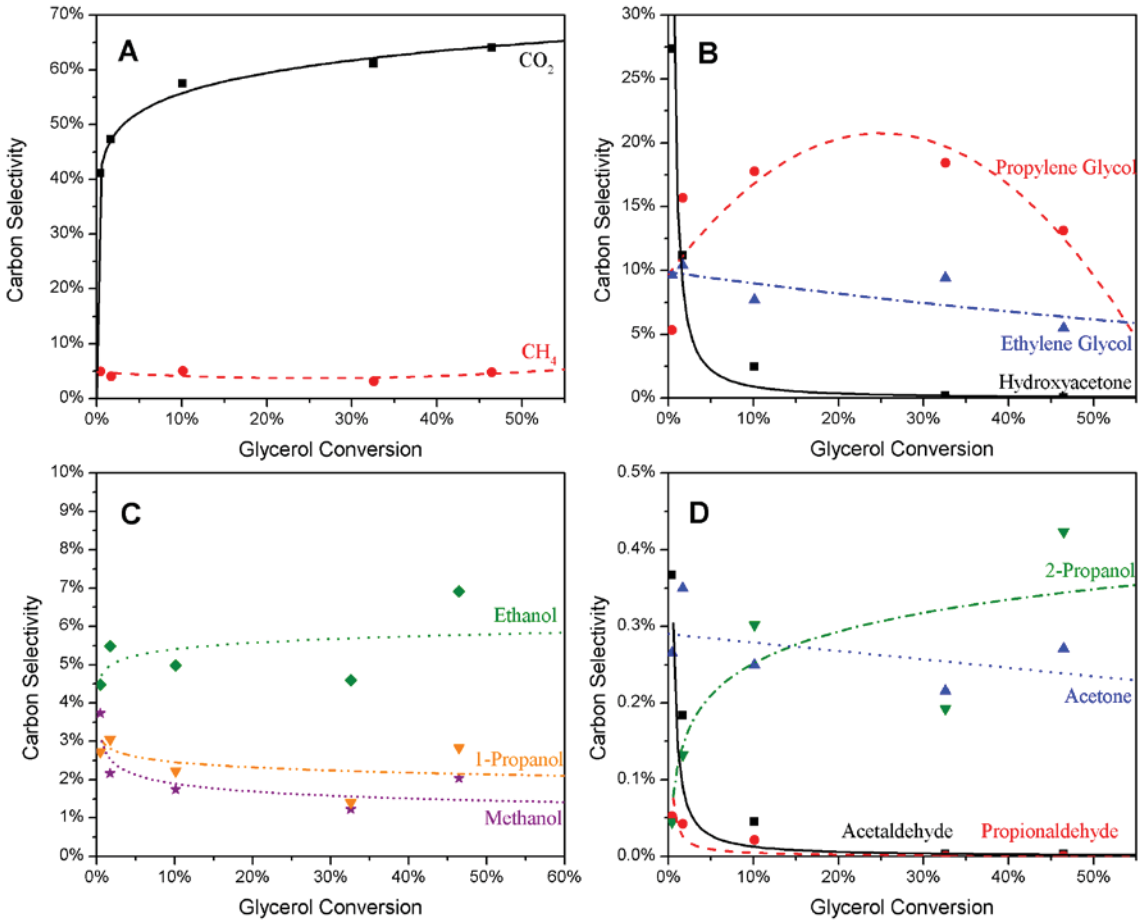

Figure 4.1 Carbon selectivity versus conversion during glycerol APR for (A) gas phase products, (B) major liquid phase products, and (C,D) minor liquid phase products.

The majority products in the gas phase effluent from glycerol conversion were H2 and CO_2, with CO_2 being the dominant carbon species in the gas phase (Figure 4.1A). The high CO_2 selectivity (>40 %) and low total alkane selectivity (less than 5 %) in the gas phase indicates that glycerol generally follows a carbon-carbon [C-C] scission pathway over Pt catalysts. The liquid phase results (Figure 4.1B) had higher selectivity to products resulting from [C-O] bond scission such as propylene glycol, ethanol, and 1-propanol, totaling between 50 and 70 % selectivity, versus 8 to 13 % selectivity for the [C-C] scission products (ethylene glycol and methanol). Overall, glycerol had a 60 %

total selectivity to the [C-C] scission pathway as a sum of CO_2 and liquid phase [C-C] product selectivities. The glycerol also showed negligible production of organic acids. Similar to glycerol, gas phase selectivity for the propylene glycol reaction (Figure 4.2A) was generally dominated by CO_2 (10-40 % selectivity) with low selectivity to alkanes (5-10 %). The higher selectivity to methane is not the result of additional [C-O] scission as for glycerol; instead, the methane is produced from [C-C] scission on the terminal hydrocarbon fragment of the feed molecule. For propylene glycol, ethane is a better indicator of [C-O] scission; ethane selectivity was lower than 10 % at all measured conversions. The major liquid phase product is hydroxyacetone, a dehydrogenation product of propylene glycol (Figure 4.2B). Propylene glycol has low selectivity to liquid phase intermediates resulting from [C-C] (ethanol) or [C-O] (1- and 2-propanol) bond scission. Of these products selectivity to ethanol (5 to 20%) was higher than the selectivity to 1-propanol (1 to 6 %). Propylene glycerol APR yielded negligible 2-propanol (<1 %) and organic acids.

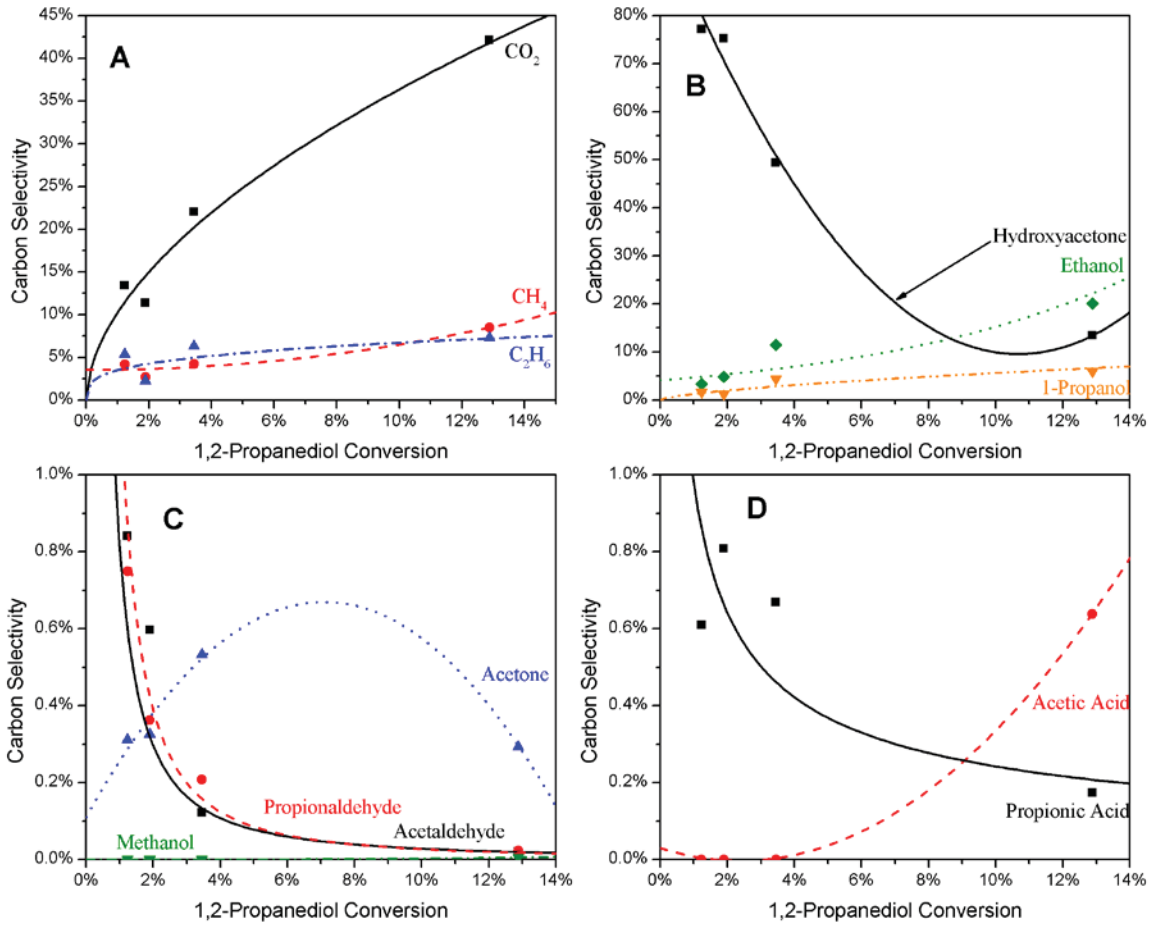

Figure 4.2 Carbon selectivity versus conversion during 1,2-propanediol APR for (A) gas phase products, (B) major liquid phase products, and (C,D) minor liquid phase products.

1,3-Propanediol displayed different selectivity trends compared to PG and glycerol. Gas phase selectivity results (Figure 4.3A) show that CO_2 and C_2H_6 dominate gas phase carbon selectivity. Methane selectivity is low (1 %), suggesting that complete [C-C] cleavage of the parent molecule is not favorable at the conversions studied. In the liquid phase (Figure 4.3B), 1-propanol was the dominant product (selectivity >30 %), with lower ethanol selectivity (<10 %). Unlike PG or glycerol, conversion of 1,3-PDO

produced some propionic acid (~5 % selectivity at all tested conversions). The remaining identified intermediates were present in carbon selectivities less than 1 %.

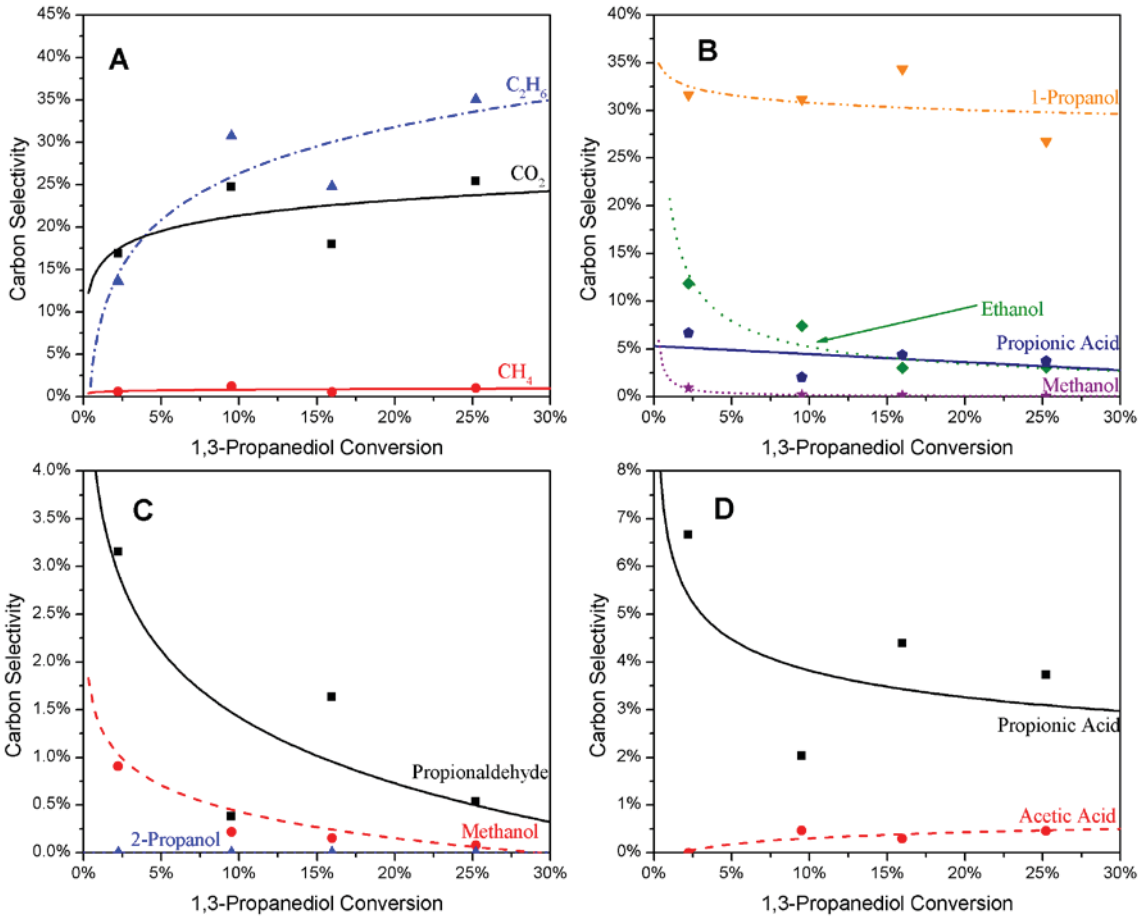

Figure 4.3 Carbon selectivity versus conversion during 1,3-propanediol APR for (A) gas phase products, (B) major liquid phase products, and (C,D) minor liquid phase products.

1-Propanol was the simplest reaction of the C3 alcohols, having a small number of identified products. Gas phase carbon selectivity (Figure 4.4A) was only CO_2 and ethane in a ratio of 1:2, in accordance with [C-C] scission of the alcohol group. No propane was detected, suggesting that [C-O] scission did not occur at up to 25 % conversion of 1-propanol. In the liquid phase (Figure 4.4B), the dominant product at low conversion was

propionaldehyde, which decreased to nearly zero selectivity at higher conversions. The only other significant product produced in the liquid phase was propionic acid (7-10 %).

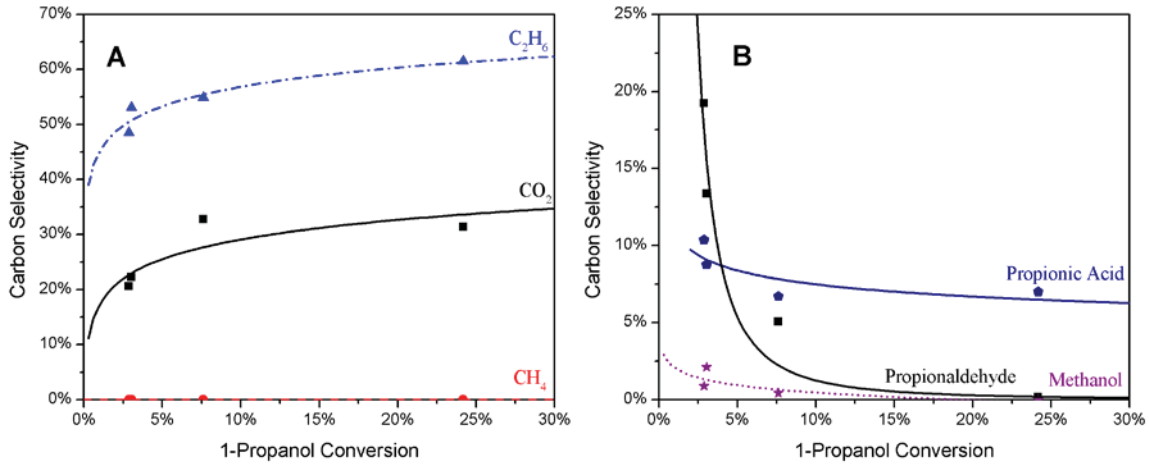

Figure 4.4 Carbon selectivity versus conversion during 1-propanol APR for (A) gas phase products and (B) liquid phase products.

Ethanol is a key APR intermediate for glycerol, propylene glycol, and 1,3-propanediol. Tor these latter two reactants ethanol and 1-propanol results can be used to assign final gaseous products to initial [C-C] or [C-O] bond scission. Thus, ethanol APR was performed to determine within each C3 alcohol reaction network whether this intermediate favors [C-O] or [C-C] scission, allowing us to assign final products to the pathway through ethanol as an intermediate. In the gas phase (Figure 4.5A) there was little ethane produced (< 5 %) and primarily a 1:1 ratio of methane to CO_2 in accordance with primarily [C-C] bond scission. In the liquid phase, there was negligible methanol

and a small amount of acetaldehyde due to dehydrogenation of ethanol, which dropped to zero selectivity at high conversion.

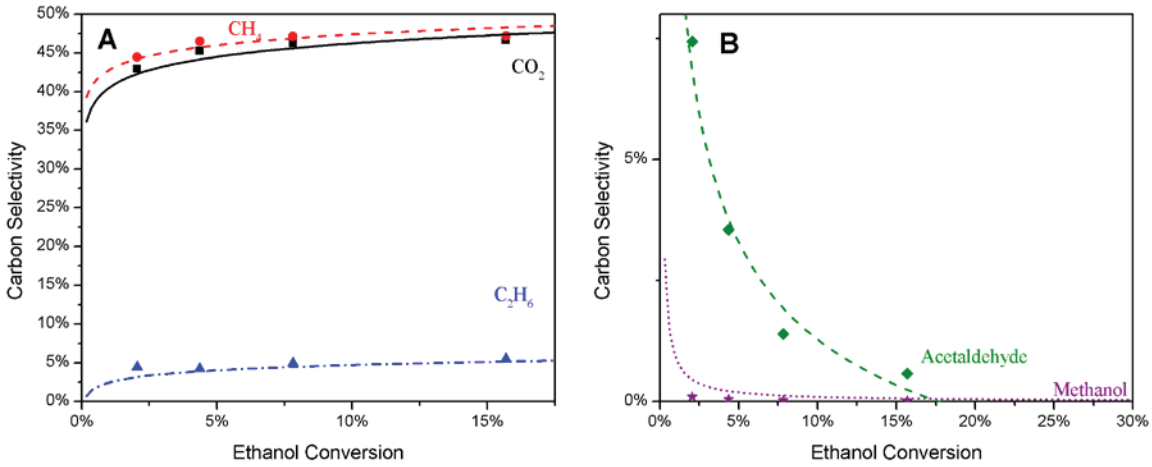

Figure 4.5 Carbon selectivity versus conversion during ethanol APR for (A) gas phase products and (B) liquid phase products.

Key reaction STYs at feed conversion between 1 % and 3 % are listed in Table 4.2. These include the reactant STY, and initial product STYs for [C-C] and [C-O] bond scission. The ratio of these initial rates indicates that based on primary products only, the preference towards selective [C-C] bond scission at low conversions is: 1,3-propanediol < glycerol < propylene glycol < ethanol < 1-propanol. There is some uncertainty in these numbers, however, due to the final products which have already reacted via initial [C-C] and [C-O] bond scission processes but which are not considered in this ratio of STYs for primary products. A more complete analysis will be discussed later by considering the entire reaction network.

Table 4.2 Site time yields of reactant consumption and initial products, the ratio of these rates, and the percentage of total products accounted for by initial products only.

Reactant	Conv.	STY / 10^{-2} s^{-1}			[C-C]/[C-O]	% of Reactant STY in Primary Products
		Reactant	First [C-C] Product(s) Rate	First [C-O] Product(s) Rate		
Glycerol	1.4%	3.0	0.59	0.87	0.69	49%
Propylene glycol	1.8%	3.7	0.27	0.06	4.9	8.8%
1,3-Propanediol	2.2%	4.7	0.84	1.5	0.56	49%
1-Propanol	3.2%	3.5	2.4	~0	High	67%
Ethanol	2.0%	7.5	6.7	0.33	20.2	94%

From Table 4.2 we also see that reactant consumption STYs were similar among C3 alcohol feed molecules (Between 3.0 and 4.7 • $10^{-2}s^{-1}$). This would be the case if all molecules have a similar rate determining step of similar activation barrier. For example, if WGS was rate limiting for aqueous phase reforming, then the experimentally measured rate of C3 alcohol decomposition would be the equal to the rate of WGS on Pt/MWCNT.

4.3.2 Free energy diagrams

The BEP relationships developed from DFT calculations were used to generate free energy diagrams for each C3 alcohol. Displayed in the following figures are the binding energy of the most favorable intermediates of each dehydrogenation of the alcohol, along with estimated transition state barriers for four possible bond-breaking steps which may occur next: [C-H], [C-C], [C-O], and [O-H] bond scission. By comparing the height of these barriers for any given point along the possible dehydrogenated intermediates (black dots), we can see the relative ease of breaking one chemical bond versus another. Dehydrogenation ([C-H] or [O-H] bond scission) occurs relatively easily beginning with

the starting reactant C3 alcohol molecule at the left. But once the barrier of these two dehydrogenation reactions starts to be a similar value to the [C-O] and [C-C] bond scission reactions, we can compare the relative heights of these two reaction routes to see which pathway is favored.

Figure 4.6 shows for 1-propanol that after three or four dehydrogenation steps, [C-C] scission becomes feasible due to the similar reaction barrier height to further dehydration steps. However, [C-O] still has a significantly higher barrier at this point, indicating that initial [C-C] bond scission during 1-propanol decomposition should be the favored route.

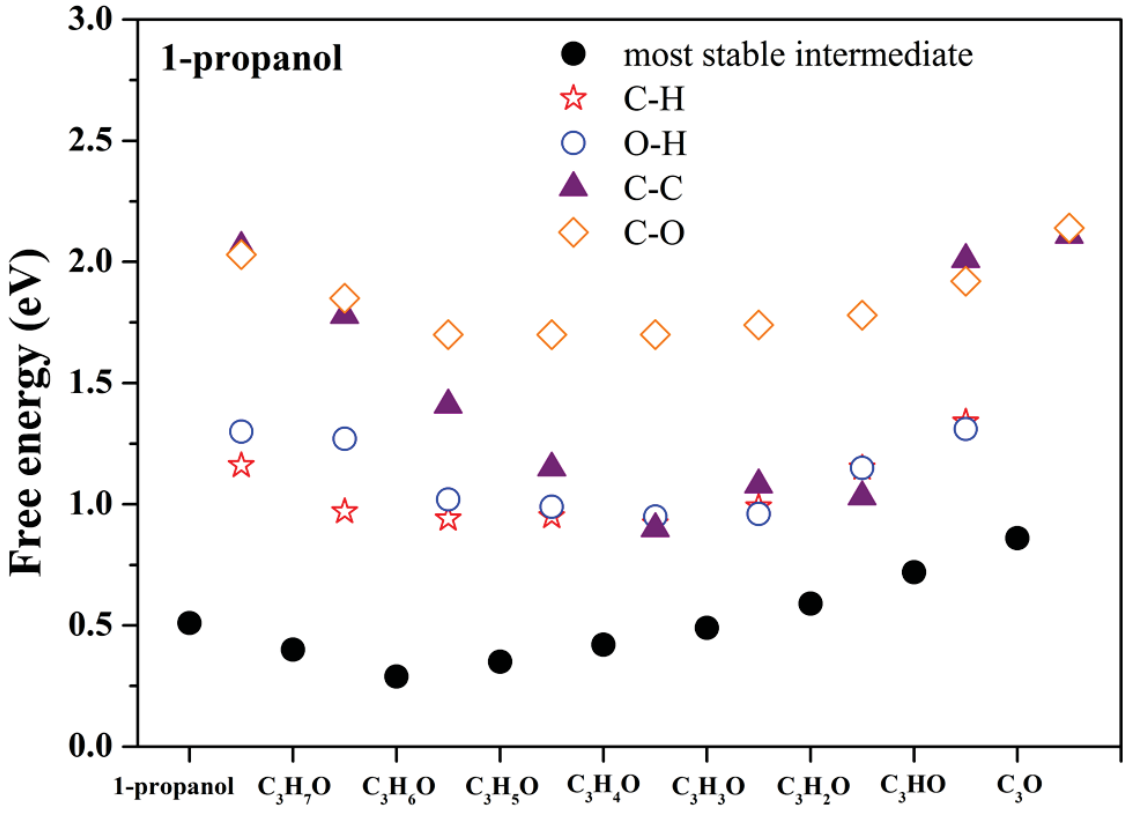

Figure 4.6 Free energy diagram for 1-propanol decomposition on Pt (111) surface. The activation barriers for breaking [C-H] (red star), [O-H] (blue circle), [C-C] (purple triangle), and [C-O] (yellow diamond] bonds are plotted for the most stable dehydrogenated intermediates as the alcohol is progressively dehydrogenated from left to right.

The conclusion is the same with 1,2-propanediol in Figure 4.7, as we see that after three or four dehydrogenation steps [C-C] bond scission barrier is significantly lower than the [C-O] bond scission barrier. The relative difference in barriers is also similar to 1-propanol. For 1,3-propanediol in Figure 4.8 the [C-C] bond scission barrier becomes feasible after five or six dehydrogenation steps, but the conclusion is the same as for the other molecules: [C-O] bond scission activation barrier is significantly higher than that of [C-C], although the difference is slightly less.

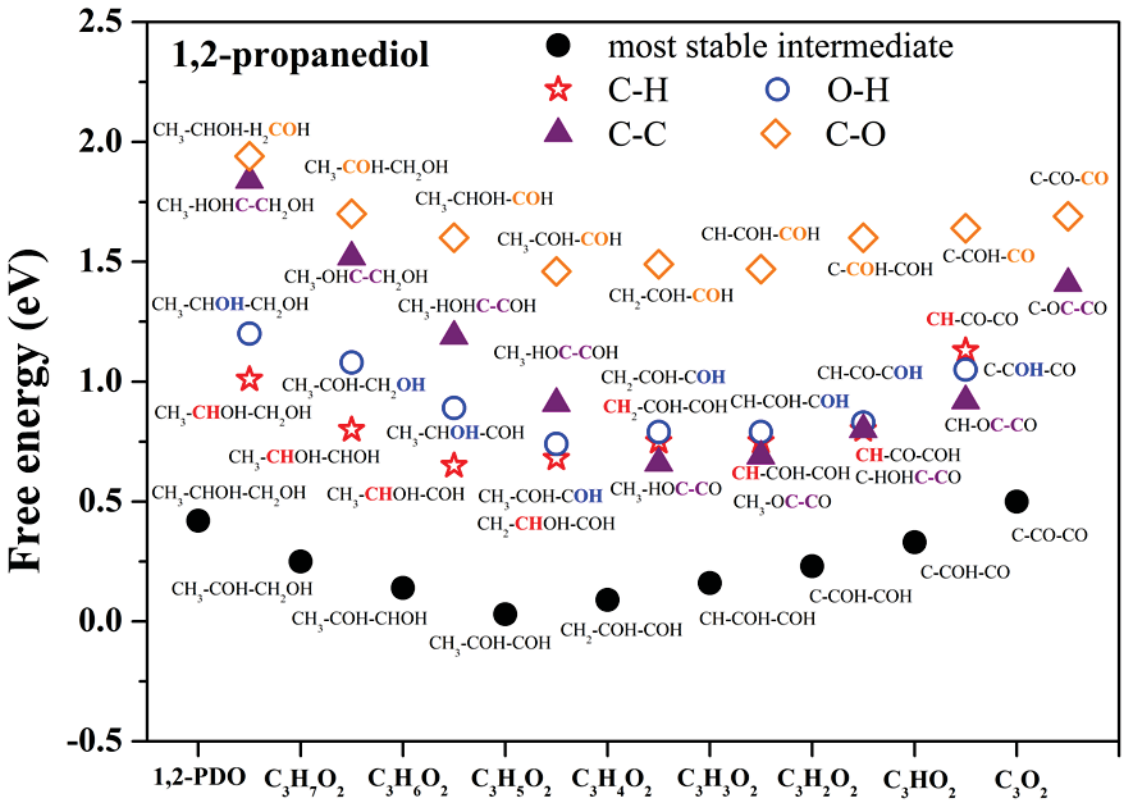

Figure 4.7 Free energy diagram for 1,2-propanediol decomposition on Pt (111) surface. The activation barriers for breaking [C-H] (red star), [O-H] (blue circle), [C-C] (purple triangle), and [C-O] (yellow diamond] bonds are plotted for the most stable dehydrogenated intermediates as the alcohol is progressively dehydrogenated from left to right.

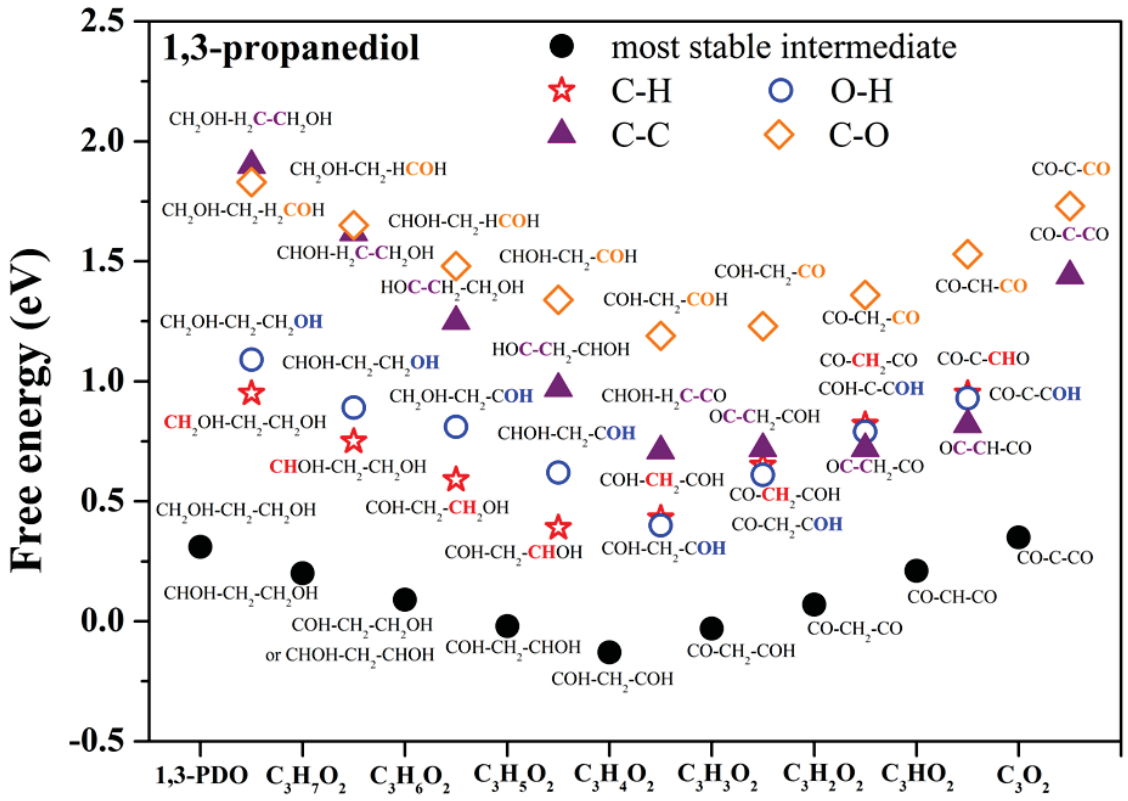

Figure 4.8 Free energy diagram for 1,3-propanediol decomposition on Pt (111) surface. The activation barriers for breaking [C-H] (red star), [O-H] (blue circle), [C-C] (purple triangle), and [C-O] (yellow diamond] bonds are plotted for the most stable dehydrogenated intermediates as the alcohol is progressively dehydrogenated from left to right.

4.4 Discussion

As with previous studies with glycerol as a reactant, the product distributions observed were consistent with parallel carbon-carbon ([C-C]) and carbon-oxygen ([C-O]) cleavage reactions. In addition, low concentrations of organic acid species were detected in some of the product distributions, suggesting an additional side reaction not observed over glycerol. The rates and selectivity trends presented here give insight into the reaction pathways towards biomass reforming, and how the positions of functional groups such as alcohol and alkyl groups affect these pathways. First, the overall rates of reaction are

similar regardless of the feed molecule which suggests that the rate determining step (RDS) may be similar on all reactants regardless of functional groups. Previous literature has suggested that the RDS for alcohol decomposition reactions is not a C-C or C-O cleavage step [12], but rather early dehydrogenation reactions at the C-H or O-H groups [13, 14]. Alternatively, the water-gas shift reaction is an important step during all APR reactions for removing CO adsorbed on the metal after decomposition of the alcohol and has been proposed as a possible RDS [15].

4.4.1 Pathway Analysis

In order to make a more complete comparison of initial reaction rates of [C-C] and [C-O] bond scission for C3 alcohols, it is necessary to look at all products, not just the initial products which can account for as little as 8.8 % of the reactant consumption (PG in Table 4.2). Also, the key intermediate ethanol needs to be looked at in its selectivity towards these two reactions. Taking the lowest conversion point, we find products distributed among the pathways as shown in Figure 4.9. The percentage of ethanol STY attributable to [C-C] bond scission (88.9 % or 87.2 %) is approximately 20 times that of [C-O] scission resulting in ethane product. Going forward in the pathway analysis, larger reaction networks of C3 alcohols will use this piece of information to estimate final products which went through ethanol as an intermediate molecule.

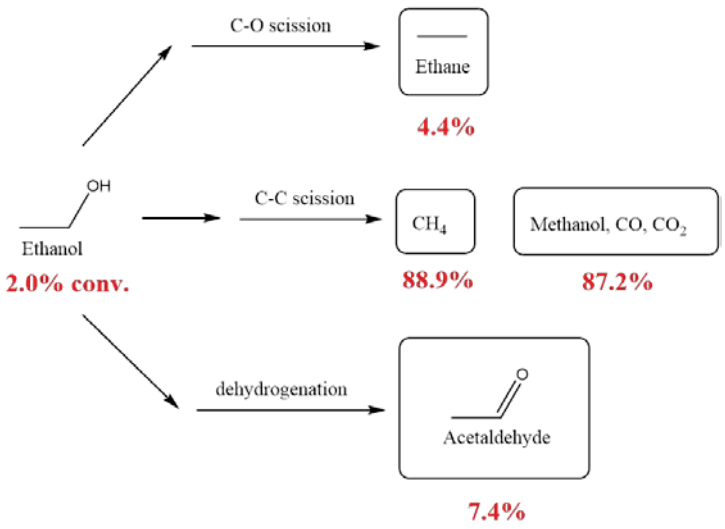

Figure 4.9 Reaction pathways of ethanol APR, and the corresponding percent of ethanol STY attributable to each product at 2.0 % ethanol conversion.

The simplest reaction network for a C3 alcohol is that of 1-propanol. Comparing the pathways for [C-C] and [C-O] bond scission yields the fact that no propane was detected and thus only the [C-C] pathway results from propanol reforming, apart from dehydrogenation and oxidation side products.

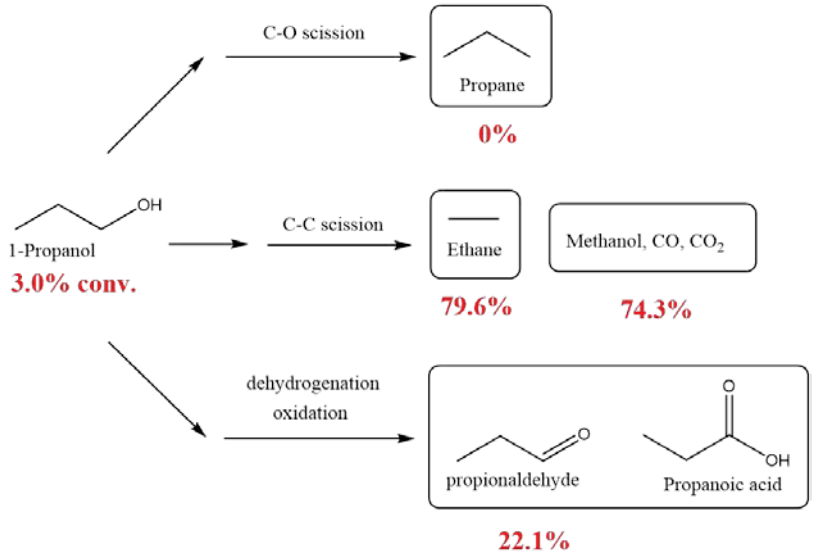

Figure 4.10 Reaction pathways of 1-propanol APR, and the corresponding percent of 1-propanol STY attributable to each product at 3.0 % 1-proanol conversion.

Next, the larger reaction network of propylene glycol in Figure 4.11 contains two intermediate steps which can yield the same final products (ethane plus methanol, CO, CO_2). These are initial [C-O] scission (to 1-propanol) followed by [C-C] scission or initial [C-C] scission (to ethanol) followed by [C-O] scission. In order to assign the product ethane to one of the two initial bond breaking steps, the results from ethanol reforming instruct that the ethane should primarily come through the initial [C-O] scission pathway. Thus by adding ethane to the initial [C-O] scission products and adding methane to the initial [C-C] scission products a better estimate of the relative [C-C]/[C-O] selectivity is obtained.

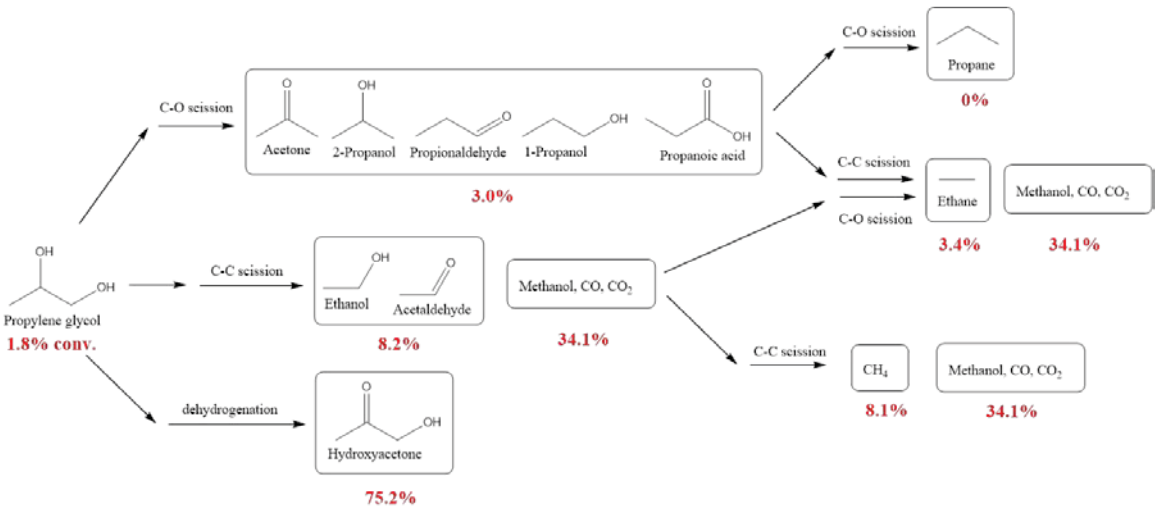

Figure 4.11 Reaction pathways of propylene glycol APR, and the corresponding percent of propylene glycol STY attributable to each product at 1.8 % propylene glycol conversion.

A similar calculation is performed with 1,3-propanediol from the reaction network in Figure 4.12, where ethane produced is assigned to initial [C-O] bond scission and methane produced is assigned to initial [C-C] bond scission. The complete results for the pathway analysis of the C3 alcohols and ethanol are found in Table 4.3.

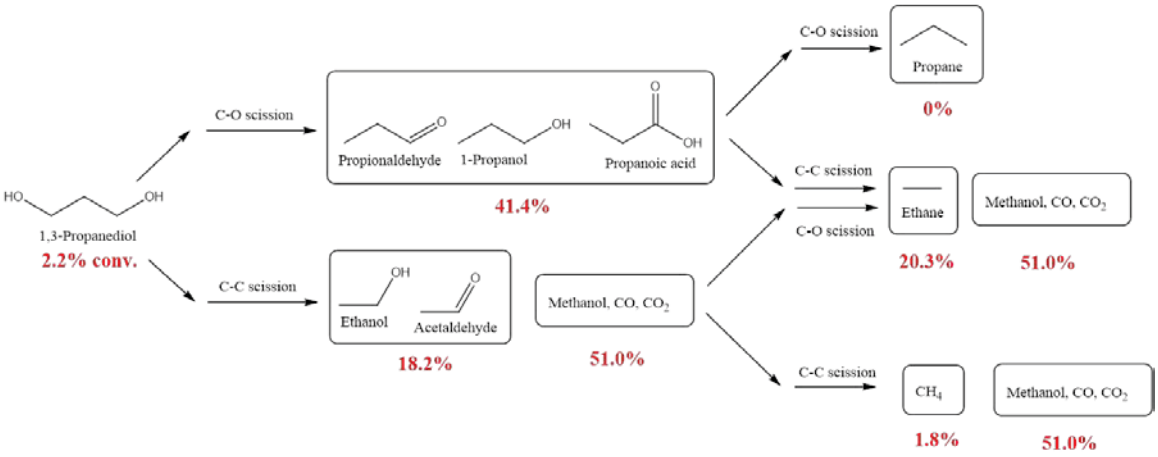

Figure 4.12 Reaction pathways of 1,3-propanediol APR, and the corresponding percent of 1,3-propanediol STY attributable to each product at 2.2 % 1,3-propanediol conversion.

Comparing the [C-C]/[C-O] ratio to the results from DFT, one would expect the ratio of these parallel pathways to be larger than unity for all three C3 alcohols studied. While this prediction agrees with the experimental results for propylene glycol and 1-propanol, the result from 1,3-propanediol is actually a ratio of less than one (0.32) which indicates a preference toward [C-O] bond scission. There may be additional effects not taken into consideration for the linear scaling relationships and the DFT calculations, however. These include the effect of adsorbed CO on the binding energies of molecules on the Pt (111) surface, or the reactivity of surface defects and surfaces besides the close packed metal (111). These defects would be relevant due to the use of Pt nanoparticles for the reaction, which have a large number of edges, corners, and surfaces. These considerations could change the adsorption strength of the dehydrogenated intermediates and the energy barriers to [C-C] and [C-O] scission reactions. If the dehydrogenated intermediates' adsorption energies change such that the lowest energy intermediates are earlier or later in the process of dehydration, the relative bond scission barriers to [C-C] and [C-O] breaking will be different. For example, the difference in relative height of the two barriers is small early in dehydrogenation of the alcohol (towards the right side of Figures 4.6 through 4.8). On the other hand, if there is a relative change in [C-C] and [C-O] scission barriers for a given intermediate there will also be a change in the overall reaction selectivity.

Table 4.3 Results of pathway analysis with final products assigned to initial bond scission pathways.

Reactant	Conversion	Reactant STY / 10^{-2} s^{-1}	Percent [C-C] initial pathway	Percent [C-O] initial pathway	[C-C]/[C-O]
Propylene glycol	1.8%	3.7	16%	6.4%	2.5
1,3-Propanediol	2.2%	4.7	20%	62%	0.32
1-Propanol	3.2%	3.5	80%	~0%	High
Ethanol	2.0%	7.5	89%	4.4%	20

The selectivity trends presented in Figures 4.1 through 4.5 give insight into how functional group position can affect the preferred pathway. Glycerol and propylene glycol prefer the [C-C] scission pathway to generate high selectivity to CO2 (and CH_4 in the case of propylene glycol). Also, the rates for the initial [C-C] scission reaction (i.e. CO_2 and ethylene glycol for glycerol, CO_2 and ethanol for PG) for glycerol and PG are higher than the measured [C-O] rates (HA/PG rate for glycerol feed, 1-PrOH rate for PG feed). This suggests that molecules with adjacent C-OH groups are more selective to the [C-C] scission pathway.

While PG had high selectivity to products resulting from the [C-C] cleavage pathway, a large fraction of that was contained as ethanol in the liquid phase. The presence of CO_2 and CH_4 in the gas phase effluent suggests that some complete conversion of the feed molecule is occurring, but the increasing selectivity towards ethanol, (20 % carbon selectivity at 13 % conversion) and the fact that the CO_2:CH_4 ratio is higher than 2 (experimental values between 3 and 5) suggest that, particularly at low conversions, the reaction is selective to a single [C-C] bond scission, forming CO_2, H_2, and ethanol. As complete conversion is reached, the ethanol will react to yield additional CH_4, driving the CO_2:CH_4 ratio closer to the expected stoichiometric value of 2. The production of ethane

via an initial [C-O], then [C-C] cleavage also causes this ratio to be higher than 2, as it generates CO_2 from the conversion of the 1-propanol. PG also had a high selectivity to hydroxyacetone at low conversion, which decreased rapidly at higher conversions. This is evidence that PG reacts through a dehydrogenated intermediate (hydroxyacetone), much like 1-PrOH.

APR of 1-propanol also favored [C-C] bond scission, reacting at the COH-alkyl bond. There were only a few products present, and the trends suggest that 1-propanol reacts first through a propionaldehyde intermediate (identified by the decaying trend in selectivity) followed by subsequent [C-C] scission to CO_2 and ethane. The CO_2:C_2H_6 ratios were close to 1:1 (within experimental error) with no propane detected, suggesting that [C-C] scission was the predominant reaction. 1-Propanol also showed production of measureable amounts of propionic acid at all conversions, suggesting the presence of a side reaction. The selectivity towards the acid decreases only slightly at higher conversions, suggesting that it is a side reaction of the feed molecule, and not a major pathway intermediate as has been previously proposed [43].

While glycerol, propylene glycol, and 1-propanol had a strong selectivity towards [C-C] scission, 1,3-propanediol reacted through a different pathway. The major product was 1-propanol at greater than 30 % selectivity for all measured conversion, which suggests that the first step in the conversion of 1,3-PDO is the [C-O] bond scission at the terminal C-OH to form 1-propanol. Ethanol, the major [C-C] scission intermediate, was detected at lower selectivity, from 12 % down to 3 % at conversion approaching 25 %. In addition, the presence of significant ethane selectivity (15-35 % selectivity) and low methane selectivity (<2 %) suggest that [C-O] scission to 1-propanol is the favored reaction,

followed by reaction along the 1-propanol pathway. This is supported by the fact that a significant fraction of propionic acid (around 5%) was detected at all conversions, as in the 1-propanol product distribution. There is still a contribution from the [C-C] scission pathway, due to the presence of ethanol (3 - 12 % selectivity) and small amounts of methane (<1 % selectivity) and the fact that CO_2:C_2H_6 ratios are less than 1:1. Compared to the reactants with adjacent C-OH groups, the relative contribution of [C-O] scission for APR of 1,3-propanediol is much higher.

4.5 Conclusions

Comparing propylene glycol and 1,3-propanediol gives some insight into the effects of alkyl position on the reactant reactivity. Propylene glycol, which contains a terminal methyl fragment tends to favor a predominantly [C-C] scission route, generating H_2, CO_2, ethanol, and methane. 1,3-Propanediol, which has a methylene fragment between the C-OH groups, has a higher selectivity to 1-propanol, and therefore a preference for [C-O] scission, to support the fact that the location of the alkyl group affects the reaction. These results show that a bridging alkyl group rather than a terminal fragment will shift the reaction selectivity towards initial [C-O] bond scission pathway, followed by subsequent [C-C] breaking at the remaining COH-alkyl bond, as in 1-propanol. The analysis of each C3 alcohol reaction network gives insight into how different molecules are formed from reforming of biomass derived compounds. Compounds with C:O stoichiometry of 1:1 generally react preferentially along a [C-C] scission pathway, but also make small amounts of [C-O] scission products, which reform further to small alkanes at higher conversions. The reaction results suggest that glycerol reforming yields methane through propylene glycol intermediates which subsequently react along a [C-C] scission pathway.

It is concluded that alkanes are generally formed during APR by [C-O] scission of an alcohol group, followed by [C-C] scission at COH-alkyl bonds. However, these results indicate that glycerol (and other similar carbohydrate molecules) are generally selective to hydrogen over Pt catalysts because their major liquid phase intermediates (propylene glycol, ethylene glycol, ethanol, and propanol), tend to prefer subsequent [C-C] scission reactions to form additional hydrogen, rather than favoring [C-O] scission reactions that would generate larger alkanes. 1,3-Propanediol, which is a minority product during glycerol APR over Pt catalysts, is the only product which reacts along a different pathway, and due to its low concentration is unlikely to have a significant effect on overall pathway selectivity. While the BEP relationships derived from DFT calculations can give support for preferential [C-C] bond scission for glycerol, propylene glycol, and 1-propanol, there is a disagreement with 1,3-propanediol which prefers initial [C-O] bond scission experimentally. Future investigation of CO coverage effects and the role of surface defects may provide an explanation for why this this disagreement occurs.

REFERENCES

REFERENCES

[1] R.D. Cortright, R.R. Davda, J.A. Dumesic, Hydrogen from catalytic reforming of biomass-derived hydrocarbons in liquid water, Nature, 418 (2002) 964-967.

[2] G.W. Huber, J.W. Shabaker, S.T. Evans, J.A. Dumesic, Aqueous-phase reforming of ethylene glycol over supported Pt and Pd bimetallic catalysts, Applied Catalysis B-Environmental, 62 (2006) 226-235.

[3] R.R. Davda, J.W. Shabaker, G.W. Huber, R.D. Cortright, J.A. Dumesic, Aqueous-phase reforming of ethylene glycol on silica-supported metal catalysts, Applied Catalysis B-Environmental, 43 (2003) 13-26.

[4] J.W. Shabaker, D.A. Simonetti, R.D. Cortright, J.A. Dumesic, Sn-modified Ni catalysts for aqueous-phase reforming: Characterization and deactivation studies, Journal of Catalysis, 231 (2005) 67-76.

[5] R.M. Ravenelle, J.R. Copeland, W.-G. Kim, J.C. Crittenden, C. Sievers, Structural Changes of γ-Al2O3-Supported Catalysts in Hot Liquid Water, Acs Catal, 1 (2011) 552-561.

[6] E. Kunkes, D. Simonetti, J. Dumesic, W. Pyrz, L. Murillo, J. Chen, D. Buttrey, The role of rhenium in the conversion of glycerol to synthesis gas over carbon supported platinum-rhenium catalysts, Journal of Catalysis, 260 (2008) 164-177.

[7] A. Tanksale, J.N. Beltramini, J.A. Dumesic, G.Q. Lu, Effect of Pt and Pd promoter on Ni supported catalysts - A TPR/TPO/TPD and microcalorimetry study, Journal of Catalysis, 258 (2008) 366-377.

[8] X.M. Wang, N. Li, L.D. Pfefferle, G.L. Haller, Pt-Co bimetallic catalyst supported on single walled carbon nanotube: XAS and aqueous phase reforming activity studies, Catal Today, 146 (2009) 160-165.

[9] P.J. Dietrich, M.C. Akatay, F.G. Sollberger, E.A. Stach, J.T. Miller, W.N. Delgass, F.H. Ribeiro, Effect of Co Loading on the Activity and Selectivity of PtCo Aqueous Phase Reforming Catalysts, Acs Catal, 4 (2013) 480-491.

[10] M. Chia, Y.J. Pagan-Torres, D. Hibbitts, Q.H. Tan, H.N. Pham, A.K. Datye, M. Neurock, R.J. Davis, J.A. Dumesic, Selective Hydrogenolysis of Polyols and Cyclic Ethers over Bifunctional Surface Sites on Rhodium-Rhenium Catalysts, J Am Chem Soc, 133 (2011) 12675-12689.

[11] J.W. Shabaker, G.W. Huber, R.R. Davda, R.D. Cortright, J.A. Dumesic, Aqueous-phase reforming of ethylene glycol over supported platinum catalysts, Catal Lett, 88 (2003) 1-8.

[12] A.V. Ruban, H.L. Skriver, J.K. Norskov, Surface segregation energies in transition-metal alloys, Phys Rev B, 59 (1999) 15990-16000.

[13] L.L. Wang, D.D. Johnson, Predicted Trends of Core-Shell Preferences for 132 Late Transition-Metal Binary-Alloy Nanoparticles, J Am Chem Soc, 131 (2009) 14023-14029.

[14] J. Greeley, M. Mavrikakis, Near-surface alloys for hydrogen fuel cell applications, Catal Today, 111 (2006) 52-58.

[15] M. Teliska, V.S. Murthi, S. Mukerjee, D.E. Ramaker, Correlation of water activation, surface properties, and oxygen reduction reactivity of supported Pt-M/C bimetallic electrocatalysts using XAS, J Electrochem Soc, 152 (2005) A2159-A2169.

[16] V.F. Kispersky, A.J. Kropf, F.H. Ribeiro, J.T. Miller, Low absorption vitreous carbon reactors for operando XAS: a case study on Cu/Zeolites for selective catalytic reduction of NOx by NH3, Phys Chem Chem Phys, 14 (2012) 2229-2238.

[17] L. Bollmann, J.L. Ratts, A.M. Joshi, W.D. Williams, J. Pazmino, Y.V. Joshi, J.T. Miller, A.J. Kropf, W.N. Delgass, F.H. Ribeiro, Effect of Zn addition on the water-gas shift reaction over supported palladium catalysts, Journal of Catalysis, 257 (2008) 43-54.

[18] A. Ciftci, S. Eren, D.A.J.M. Ligthart, E.J.M. Hensen, Platinum-Rhenium Synergy on Reducible Oxide Supports in Aqueous-Phase Glycerol Reforming, Chemcatchem, 6 (2014) 1260-1269.

[19] D.L. King, L.A. Zhang, G. Xia, A.M. Karim, D.J. Heldebrant, X.Q. Wang, T. Peterson, Y. Wang, Aqueous phase reforming of glycerol for hydrogen production over Pt-Re supported on carbon, Applied Catalysis B-Environmental, 99 (2010) 206-213.

[20] A.V. Kirilin, A.V. Tokarev, H. Manyar, C. Hardacre, T. Salmi, J.P. Mikkola, D.Y. Murzin, Aqueous phase reforming of xylitol over Pt-Re bimetallic catalyst: Effect of the Re addition, Catal Today, 223 (2014) 97-107.

[21] L. Zhang, A.M. Karim, M.H. Engelhard, Z.H. Wei, D.L. King, Y. Wang, Correlation of Pt-Re surface properties with reaction pathways for the aqueous-phase reforming of glycerol, Journal of Catalysis, 287 (2012) 37-43.

[22] D. Simonetti, E. Kunkes, J. Dumesic, Gas-phase conversion of glycerol to synthesis gas over carbon-supported platinum and platinum-rhenium catalysts, Journal of Catalysis, 247 (2007) 298-306.

[23] D. Hibbitts, Q. Tan, M. Neurock, Acid strength and bifunctional catalytic behavior of alloys comprised of noble metals and oxophilic metal promoters, Journal of Catalysis, 315 (2014) 48-58.

[24] P.J. Dietrich, R.J. Lobo-Lapidus, T.P. Wu, A. Sumer, M.C. Akatay, B.R. Fingland, N. Guo, J.A. Dumesic, C.L. Marshall, E. Stach, J. Jellinek, W.N. Delgass, F.H. Ribeiro, J.T. Miller, Aqueous Phase Glycerol Reforming by PtMo Bimetallic Nano-Particle Catalyst: Product Selectivity and Structural Characterization, Top Catal, 55 (2012) 53-69.

[25] E. Bus, J.A. van Bokhoven, Electronic and geometric structures of supported platinum, gold, and platinum - Gold catalysts, J Phys Chem C, 111 (2007) 9761-9768.

[26] Y. Lei, J. Jelic, L.C. Nitsche, R. Meyer, J. Miller, Effect of Particle Size and Adsorbates on the L-3, L-2 and L-1 X-ray Absorption Near Edge Structure of Supported Pt Nanoparticles, Top Catal, 54 (2011) 334-348.

[27] J.K. Norskov, J. Rossmeisl, A. Logadottir, L. Lindqvist, J.R. Kitchin, T. Bligaard, H. Jonsson, Origin of the overpotential for oxygen reduction at a fuel-cell cathode, J Phys Chem B, 108 (2004) 17886-17892.

[28] G.H. Via, K.F. Drake, G. Meitzner, F.W. Lytle, J.H. Sinfelt, Analysis of Exafs Data on Bimetallic Clusters, Catal Lett, 5 (1990) 25-33.

[29] E. Christoffersen, P. Liu, A. Ruban, H.L. Skriver, J.K. Norskov, Anode materials for low-temperature fuel cells: A density functional theory study, Journal of Catalysis, 199 (2001) 123-131.

[30] P.J. Dietrich, F.G. Sollberger, M.C. Akatay, E.A. Stach, W.N. Delgass, J.T. Miller, F.H. Ribeiro, Structural and catalytic differences in the effect of Co and Mo as promoters for Pt-based aqueous phase reforming catalysts, Applied Catalysis B: Environmental, 156–157 (2014) 236-248.

[31] P.J. Dietrich, T.P. Wu, A. Sumer, J.A. Dumesic, J. Jellinek, W.N. Delgass, F.H. Ribeiro, J.T. Miller, Aqueous Phase Glycerol Reforming with Pt and PtMo Bimetallic Nanoparticle Catalysts: The Role of the Mo Promoter, Top Catal, 56 (2013) 1814-1828.

[32] S. Wang, V. Petzold, V. Tripkovic, J. Kleis, J.G. Howalt, E. Skulason, E.M. Fernandez, B. Hvolbaek, G. Jones, A. Toftelund, H. Falsig, M. Bjorketun, F. Studt, F. Abild-Pedersen, J. Rossmeisl, J.K. Norskov, T. Bligaard, Universal transition state scaling relations for (de)hydrogenation over transition metals, Phys Chem Chem Phys, 13 (2011) 20760-20765.

[33] N.R. Singh, W.N. Delgass, F.H. Ribeiro, R. Agrawal, Estimation of liquid fuel yields from biomass, Environmental science & technology, 44 (2010) 5298-5305.

[34] J.N. Chheda, G.W. Huber, J.A. Dumesic, Liquid-phase catalytic processing of biomass-derived oxygenated hydrocarbons to fuels and chemicals, Angewandte Chemie, 46 (2007) 7164-7183.

[35] G.W. Huber, J.N. Chheda, C.J. Barrett, J.A. Dumesic, Production of liquid alkanes by aqueous-phase processing of biomass-derived carbohydrates, Science, 308 (2005) 1446-1450.

[36] J.Q. Bond, D.M. Alonso, D. Wang, R.M. West, J.A. Dumesic, Integrated catalytic conversion of gamma-valerolactone to liquid alkenes for transportation fuels, Science, 327 (2010) 1110-1114.

[37] X.M. Wang, N. Li, L.D. Pfefferle, G.L. Haller, Pt-Co Bimetallic Catalyst Supported on Single-Walled Carbon Nanotubes: Effect of Alloy Formation and Oxygen Containing Groups, J Phys Chem C, 114 (2010) 16996-17002.

[38] X.M. Wang, N. Li, J.A. Webb, L.D. Pfefferle, G.L. Haller, Effect of surface oxygen containing groups on the catalytic activity of multi-walled carbon nanotube supported Pt catalyst, Applied Catalysis B-Environmental, 101 (2010) 21-30.

[39] X. Wang, N. Li, L.D. Pfefferle, G.L. Haller, Metal nanoparticles inside multi-walled carbon nanotubes: A simple method of preparation and of microscopic image analysis, Microporous and Mesoporous Materials, 176 (2013) 139-144.

[40] J.T. Miller, A.J. Kropf, Y. Zha, J.R. Regalbuto, L. Delannoy, C. Louis, E. Bus, J.A. van Bokhoven, The effect of gold particle size on Au-Au bond length and reactivity toward oxygen in supported catalysts, Journal of Catalysis, 240 (2006) 222-234.

[41] G.W. Huber, J.A. Dumesic, An overview of aqueous-phase catalytic processes for production of hydrogen and alkanes in a biorefinery, Catal Today, 111 (2006) 119-132.

[42] A. Wawrzetz, B. Peng, A. Hrabar, A. Jentys, A.A. Lemonidou, J.A. Lercher, Towards understanding the bifunctional hydrodeoxygenation and aqueous phase reforming of glycerol, Journal of Catalysis, 269 (2010) 411-420.

[43] R. Lobo, C.L. Marshall, P.J. Dietrich, F.H. Ribeiro, C. Akatay, E.A. Stach, A. Mane, Y. Lei, J. Elam, J.T. Miller, Understanding the Chemistry of H2 Production for 1-Propanol Reforming: Pathway and Support Modification Effects, Acs Catal, 2 (2012) 2316-2326.

[44] T.G. Kelly, A.L. Stottlemyer, H. Ren, J.G. Chen, Comparison of O-H, C-H, and C-O Bond Scission Sequence of Methanol on Tungsten Carbide Surfaces Modified by Ni, Rh, and Au, J Phys Chem C, 115 (2011) 6644-6650.

[45] W. Yu, M.A. Barteau, J.G. Chen, Glycolaldehyde as a Probe Molecule for Biomass Derivatives: Reaction of C—OH and C═O Functional Groups on Monolayer Ni Surfaces, J Am Chem Soc, 133 (2011) 20528-20535.

[46] O. Skoplyak, M.A. Barteau, J.G.G. Chen, Comparison of H-2 production from ethanol and ethylene glycol on M/Pt(111) (M = Ni, Fe, Ti) bimetallic surfaces, Catal Today, 147 (2009) 150-157.

[47] P. Ferrin, D. Simonetti, S. Kandoi, E. Kunkes, J.A. Dumesic, J.K. Nørskov, M. Mavrikakis, Modeling Ethanol Decomposition on Transition Metals: A Combined Application of Scaling and Brønsted−Evans−Polanyi Relations, J Am Chem Soc, 131 (2009) 5809-5815.

[48] B. Liu, J. Greeley, Decomposition Pathways of Glycerol via C-H, O-H, and C-C Bond Scission on Pt(111): A Density Functional Theory Study, J Phys Chem C, 115 (2011) 19702-19709.

[49] B. Liu, J. Greeley, Density Functional Theory Study of Selectivity Considerations for C-C Versus C-O Bond Scission in Glycerol Decomposition on Pt(111), Top Catal, 55 (2012) 280-289.

APPENDICES

Appendix A Chapter 2 Supplementary Information

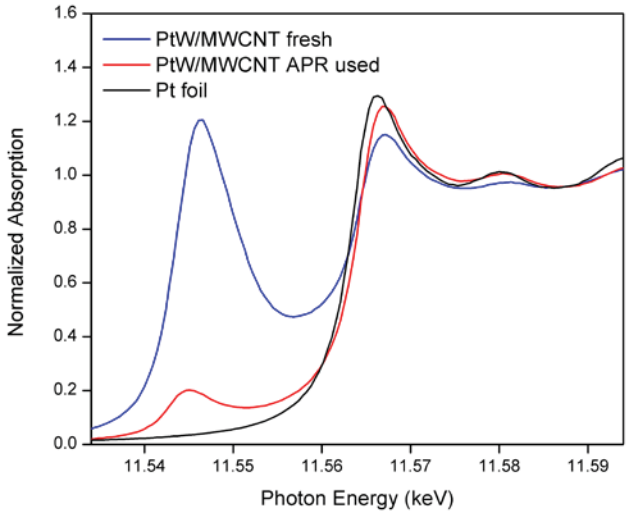

Figure A. 1 XANES spectra of the W L_{II} and Pt L_{III} edges for reduced PtW/MWCNT catalyst before (blue) and after (red) reaction as compared to reference Pt foil (black). This overlap in spectra necessitated using Pt L_{II} edge data for analysis.

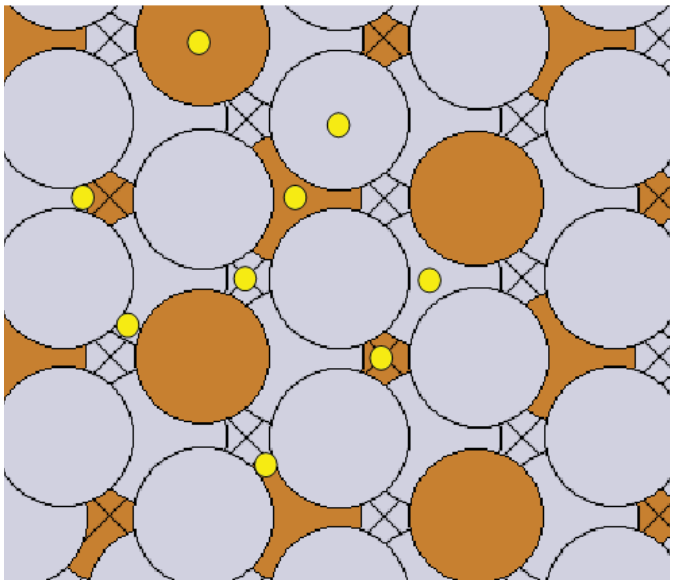

Figure A. 2 The locations of the 9 considered adsorption sites for OH species including on top, HCP, FCC, and bridge sites.

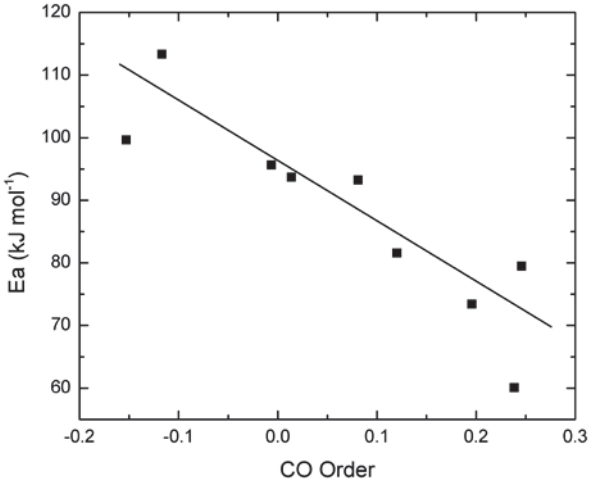

Figure A. 3 Apparent activation energy versus apparent CO order for WGS reaction for all bimetallic and monometallic catalysts

Table A. 1 Linear combination XANES fits of K edge of promoter metal for samples that have two or fewer oxidation states. Fits were obtained with foil and oxide referenced and fit over the range of -10 eV to +30 eV around the absorption edge.

Catalyst	M (%)	MO (%)
5% Pt, 1.4% Fe/MWCNT fresh	86	14
5% Pt, 1.4% Fe/MWCNT used	75	27
5% Pt, 1.5% Co/MWCNT fresh	86	14
5% Pt, 1.5% Co/MWCNT used	64	34
5% Pt, 1.5% Ni/MWCNT fresh	93	7
5% Pt, 1.5% Ni/MWCNT used	85	18
5% Pt, 1.6% Cu/MWCNT fresh	98	3
5% Pt, 1.6% Cu/MWCNT used	67	35

Table A. 2 Edge position of XANES for promoter metals of PtM/MWCNT catalysts and reference foils, oxides, and carbides. Edge position is determined as the first maximum of the first derivative of the normalized absorption spectrum.

Sample	Edge Energy (keV)	Sample	Edge Energy (keV)
Mn foil	6.5390	Mo foil	20.0000
MnO_2	6.5397	MoO_2	20.0132
Mn_2O_3	6.5404	MoO_3	20.0162
MnO_3	6.5395	Mo_2C	20.0226
5% Pt, 1.4% Mn/MWCNT fresh	6.5396	5% Pt, 2.5% Mo/MWCNT fresh	20.0014
5% Pt, 1.4% Mn/MWCNT used	6.5400	5% Pt, 2.5% Mo/MWCNT used	20.0119
Fe foil	7.1120	W foil	10.2070
FeO	7.1117	WO_2	10.2071
5% Pt, 1.4% Fe/MWCNT fresh	7.1120	WO_3	10.2091
5% Pt, 1.4% Fe/MWCNT used	7.1131	WC	10.2071
Co foil	7.7090	5% Pt, 4.7% W/MWCNT fresh	10.2087
CoO	7.7163	5% Pt, 4.7% W/MWCNT used	10.2077
5% Pt, 1.5% Co/MWCNT fresh	7.7091	Re foil	10.5350
5% Pt, 1.5% Co/MWCNT used	7.7091	ReO_2	10.5364
Ni foil	8.3330	ReO_3	10.5372
NiO	8.3408	5% Pt, 4.8% Re/MWCNT fresh	10.5361
5% Pt, 1.5% Ni/MWCNT fresh	8.3329	5% Pt, 4.8% Re/MWCNT used	10.5353
5% Pt, 1.5% Ni/MWCNT used	8.3330		
Cu foil	8.9790		
Cu_2O	8.9801		
CuO	8.9833		
5% Pt, 1.6% Cu/MWCNT fresh	8.9789		
5% Pt, 1.6% Cu/MWCNT used	8.9790		

Table A. 3 Edge position of XANES for Pt L_{III} edge for PtM/MWCNT catalysts (or Pt L_{II} for PtW) and reference Pt foil. Edge position is determined as the maximum of the first derivative of the normalized absorption spectrum.

Sample	Edge Energy (keV)	Sample	Edge Energy (keV)
Pt foil (L_{III} Edge)	11.5640	Pt foil (L_{II} Edge)	13.2730
5% Pt/MWCNT fresh	11.5637	5% Pt, 4.7% W/MWCNT fresh	13.2732
5% Pt, 1.4% Mn/MWCNT fresh	11.5640	5% Pt, 4.7% W/MWCNT used	13.2731
5% Pt, 1.4% Mn/MWCNT used	11.5640		
5% Pt, 1.4% Fe/MWCNT fresh	11.5640		
5% Pt, 1.4% Fe/MWCNT used	11.5639		
5% Pt, 1.5% Co/MWCNT fresh	11.5641		
5% Pt, 1.5% Co/MWCNT used	11.5639		
5% Pt, 1.5% Ni/MWCNT fresh	11.5638		
5% Pt, 1.5% Ni/MWCNT used	11.5639		
5% Pt, 1.6% Cu/MWCNT fresh	11.5641		
5% Pt, 1.6% Cu/MWCNT used	11.5640		
5% Pt, 2.5% Mo/MWCNT fresh	11.5642		
5% Pt, 2.5% Mo/MWCNT used	11.5642		
5% Pt, 4.8% Re/MWCNT fresh	11.5646		
5% Pt, 4.8% Re/MWCNT used	11.5640		

Table A. 4 EXAFS fitting parameters for PtM/MWCNT catalysts.

Catalyst	Absorber - Backscatter	N	R (Å)	$\Delta\sigma^2$ (10^{-3} Å^2)	E_0 shift (eV)	residual (%)
5% Pt/MWCNT fresh	Pt-Pt	7.8	2.74	0.002	-1.2	8.0
5% Pt, 1.4% Mn/MWCNT fresh	Pt-Pt	7.0	2.74	0.002	-1.7	5.5
	Pt-Mn	1.7	2.70	0.002	5.2	
	Mn-O	5.6	2.15	0.001	4.4	15.8
5% Pt, 1.4% Mn/MWCNT used	Pt-Pt	9.3	2.74	0.002	-1.9	5.3
	Pt-Mn	0.9	2.70	0.002	6.8	
	Mn-Pt	4.9	2.70	0.002	-6.9	25.4
	Mn-O	4.7	1.80	0.001	0.2	
5% Pt, 1.4% Fe/MWCNT fresh	Pt-Pt	8.1	2.76	0.001	-1.0	4.4
	Pt-Fe	1.7	2.62	0.001	5.7	
	Fe-Pt	1.0	2.63	0.002	-2.4	6.6
	Fe-Fe	6.0	2.48	0.002	-1.9	
5% Pt, 1.4% Fe/MWCNT used	Pt-Pt	9.7	2.76	0.001	0.3	6.0
	Pt-Fe	0.9	2.62	0.001	-1.5	
	Fe-Pt	4.1	2.62	0.002	-16.6	15.7
	Fe-O	2.4	1.87	0.002	8.7	
5% Pt, 1.5% Co/MWCNT fresh	Pt-Pt	5.5	2.70	0.002	-4.0	11.6
	Pt-Co	2.1	2.61	0.002	5.4	
	Co-Pt	3.8	2.61	0.002	9.3	18.0
	Co-Co	7.7	2.51	0.002	-2.4	
5% Pt, 1.5% Co/MWCNT used	Pt-Pt	8.4	2.73	0.002	-1.4	7.2
	Pt-Co	1.5	2.62	0.002	2.6	
	Co-Pt	4.5	2.62	0.002	-21.9	
	Co-Co	4.0	2.51	0.002	-3.9	17.9
	Co-O	2.3	1.95	0.002	7.3	
5% Pt, 1.5% Ni/MWCNT fresh	Pt-Pt	7.5	2.74	0.002	-1.6	9.4
	Pt-Ni	2.4	2.61	0.002	8.6	
	Ni-Pt	1.7	2.61	0.002	10.0	5.8
	Ni-Ni	8.4	2.49	0.002	-2.2	
5% Pt, 1.5% Ni/MWCNT used	Pt-Pt	9.3	2.74	0.002	-1.3	5.9
	Pt-Ni	1.6	2.62	0.002	3.9	
	Ni-Pt	2.3	2.62	0.002	-11.1	3.7
	Ni-Ni	5.9	2.49	0.002	-1.4	

Table A. 5 EXAFS fitting parameters for PtM/MWCNT catalysts. (continued)

Catalyst	Absorber - Backscatter	N	R (Å)	$\Delta\sigma^2$ (10^{-3} Å^2)	E0 shift (eV)	residual (%)
5% Pt, 1.6% Cu/MWCNT fresh	Pt-Pt	7.4	2.73	0.002	-1.9	5.3
	Pt-Cu	2.3	2.64	0.002	7.5	
	Cu-Pt	2.0	2.64	0.002	-10.3	2.6
	Cu-Cu	7.4	2.56	0.002	-1.3	
5% Pt, 1.6% Cu/MWCNT used	Pt-Pt	7.7	2.72	0.002	-1.7	4.6
	Pt-Cu	3.0	2.64	0.002	5.7	
	Cu-Pt	2.7	2.64	0.002	-14.8	
	Cu-Cu	4.9	2.55	0.002	-2.0	4.0
	Cu-O	1.4	1.95	0.002	8.1	
5% Pt, 2.5% Mo/MWCNT fresh	Pt-Pt	7.4	2.75	0.001	-2.1	15.9
	Pt-Mo	2.6	2.73	0.001	10.2	
	Mo-Pt	1.5	2.74	0.002	-11.9	
	Mo-Mo	1.3	2.80	0.002	-2.8	12.0
	Mo-O	2.0	2.08	0.002	6.8	
5% Pt, 2.5% Mo/MWCNT used	Pt-Pt	8.5	2.76	0.001	-1.5	8.3
	Pt-Mo	2.1	2.74	0.001	10.7	
	Mo-Pt	1.3	2.74	0.002	-9.8	
	Mo-Mo	2.0	2.80	0.002	0.2	14.0
	Mo-O	2.6	2.08	0.002	6.7	
5% Pt, 4.7% W/MWCNT fresh	Pt-M	8.7	2.74	0.002	-1.2	10.4
	W-M	0.9	2.70	0.002	-8.9	
	W-O	1.8	1.83	0.002	-5.8	13.6
	W-C	2.6	2.10	0.002	-0.4	
5% Pt, 4.7% W/MWCNT used	Pt-M	10.1	2.74	0.002	-1.2	11.9
	W-M	3.3	2.69	0.002	-5.3	
	W-O	1.3	1.84	0.002	-2.4	10.4
	W-C	2.4	2.36	0.002	-15.7	
5% Pt, 4.8% Re/MWCNT fresh	Pt-M	8.0	2.73	0.002	-0.2	6.8
	Re-M	7.4	2.71	0.002	-2.7	15.0
5% Pt, 4.8% Re/MWCNT used	Pt-M	10.5	2.75	0.002	-0.6	4.0
	Re-M	4.3	2.69	0.002	-6.0	18.8
	Re-O	1.7	1.75	0.002	1.0	

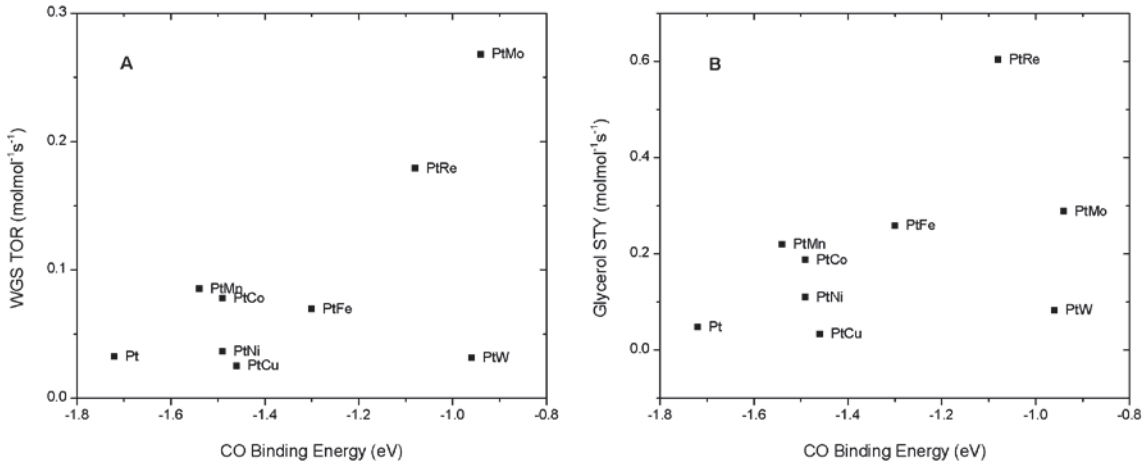

Figure A. 4 WGS TOR (A) and glycerol STY (B) versus CO binding energy for CO adsorbed on Pt top site of Pt_3M alloy.

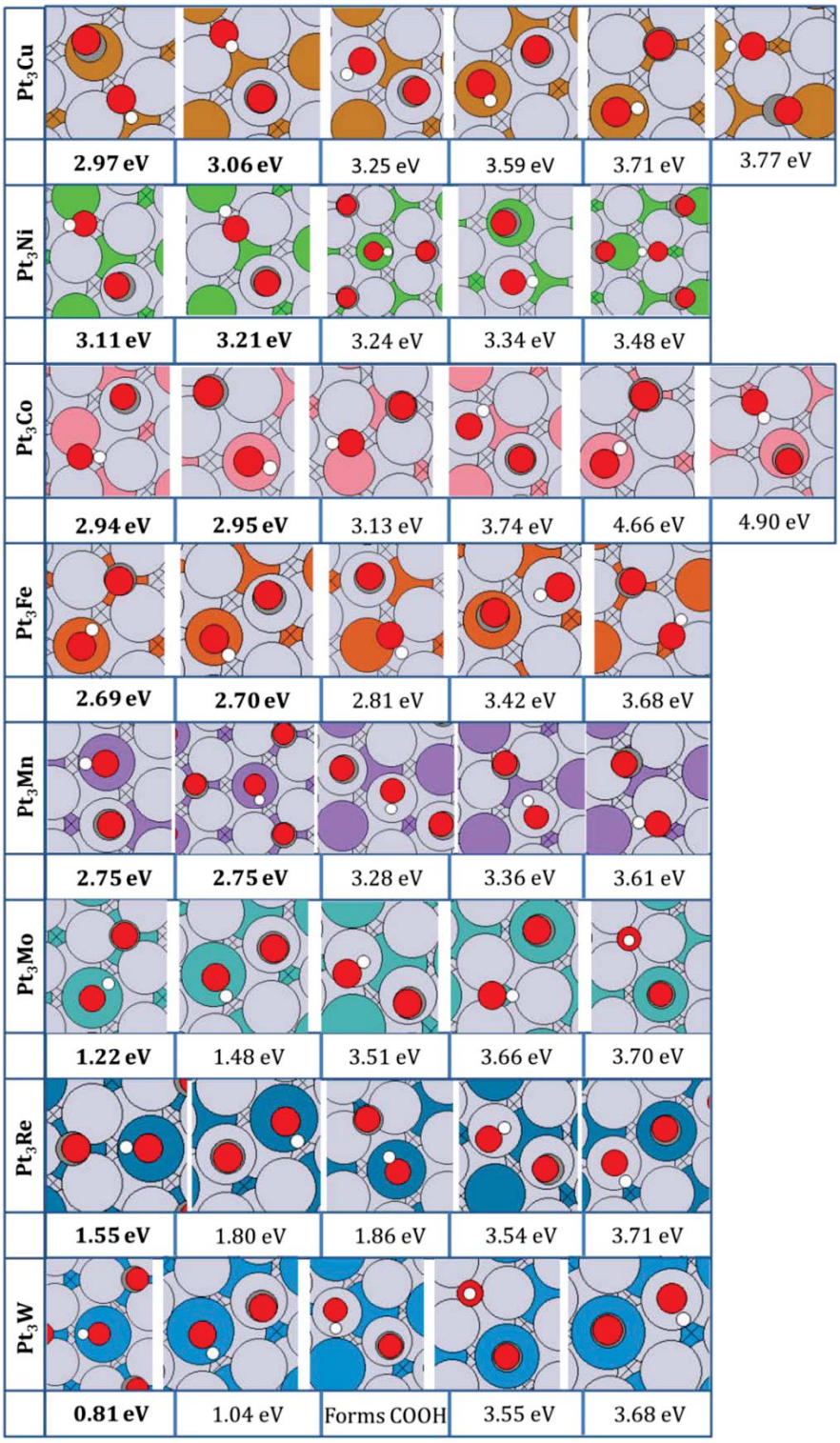

Figure A. 5 The lowest (left) to highest (right) energy configurations for OH adsobed on a Pt_3M (111) surface with CO coadsorbed as calculated by DFT. The lowest energy configurations within 0.1eV of each other are in bold.

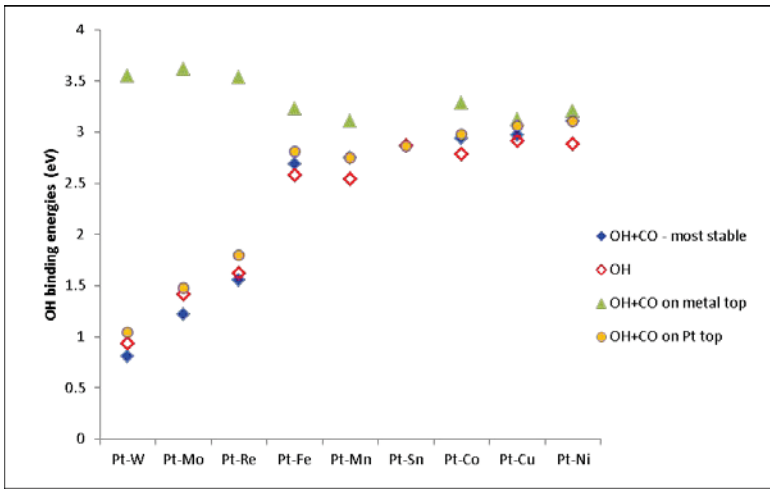

Figure A. 6 For the Pt_3M (111) surfaces, OH binding energy on the clean surface, OH binding energy on a surface preadsorbed CO on either the most stable binding site, the M top site, or the Pt top site.

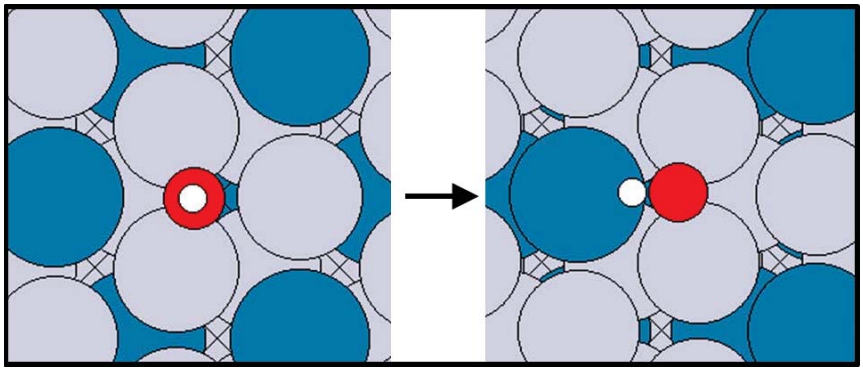

Figure A. 7 Sub-surface rearrangement induced by placing OH on Pt bridge site for Pt_3Re, Pt_3Mo, Pt_3W.

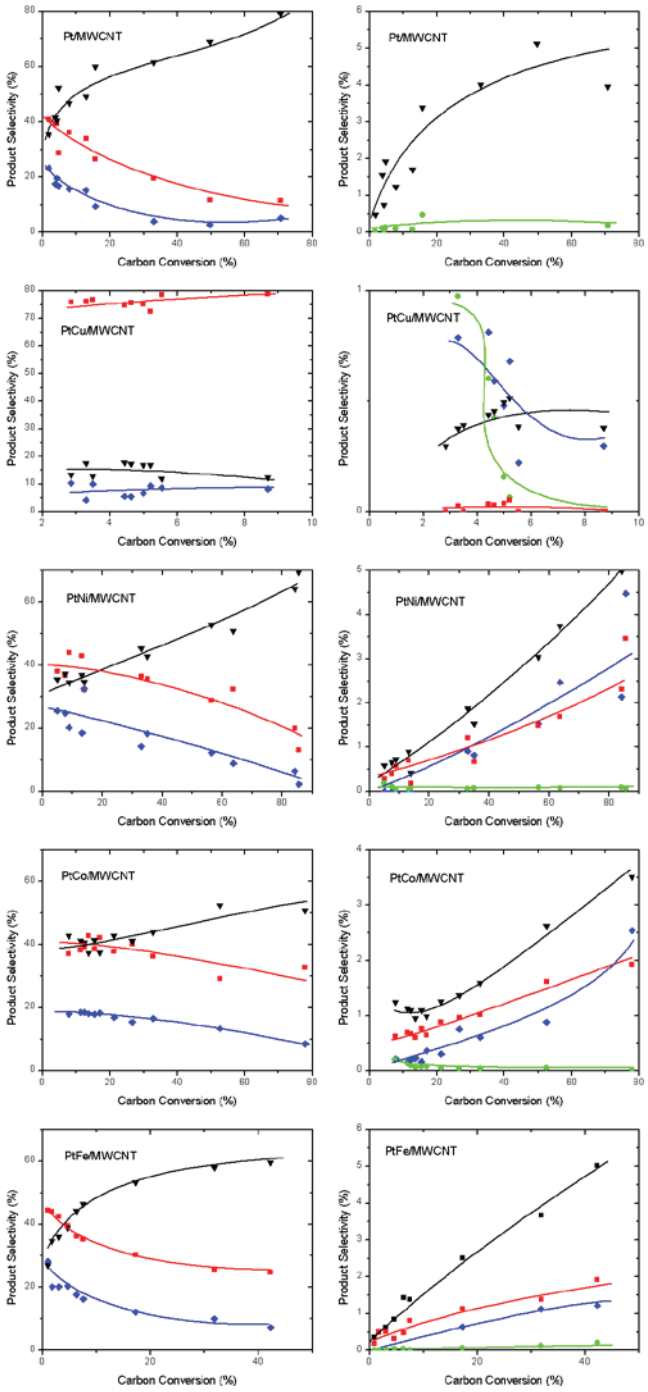

Figure A. 8 Carbon selectivity versus carbon conversion during glycerol APR. The left column contains plots of major products: CO_2 (black triangles), [C-O] scission liquid products (red squares), [C-C] scission liquid products (blue diamonds). The right column contains plots of minor products: CH_4 (black triangles), C_2H_6 (red squares), organic acids (blue diamonds), CO (green circles). Data obtained at 230 °C, 32 bar total pressure, 10 wt% glycerol feed.

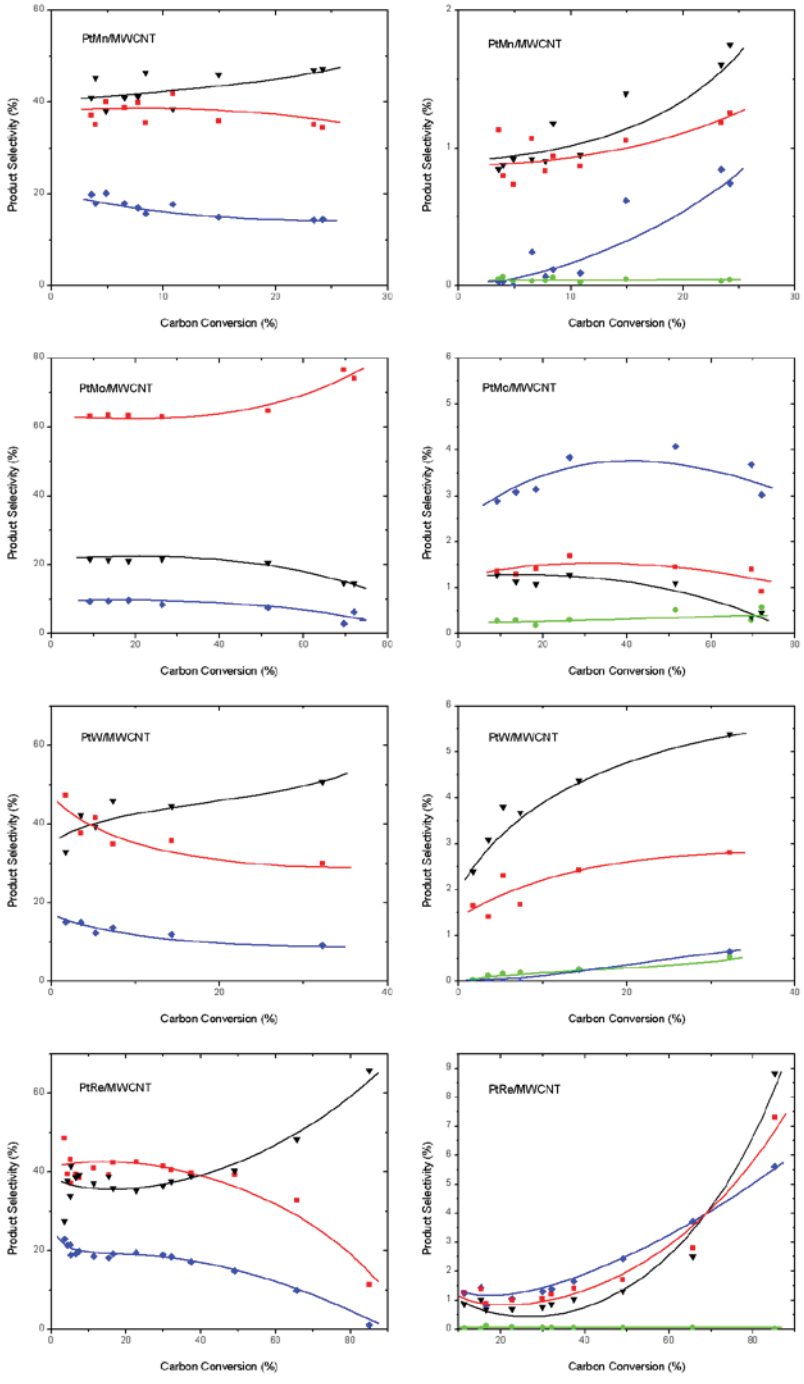

Figure A. 9 Carbon selectivity versus carbon conversion during glycerol APR. The left column contains plots of major products: CO_2 (black triangles), [C-O] scission liquid products (red squares), [C-C] scission liquid products (blue diamonds). The right column contains plots of minor products: CH_4 (black triangles), C_2H_6 (red squares), organic acids (blue diamonds), CO (green circles). Data obtained at 230 °C, 32 bar total pressure, 10 wt% glycerol feed.

TEM and Chemisorption

Carbon nanotubes provide a TEM-friendly support for counting all particles due to the thin transparent nature of the material, as compared to porous oxides or even activated carbon which contain some hidden metal nanoparticles. Transmission electron micrographs of the used samples showed a unimodal distribution for all used catalysts, which ranges from 1.6 nm for PtMo to 3.1 nm for PtNi in mean particle size according to Table A.6. It is of note that the two narrowest particle distributions corresponded to the bimetallic catalysts with the most oxophillic promoter metals PtMo and PtRe. In literature it has been argued that the strong interaction of rhenium with the support is responsible for preventing sintering of PtRe nanoparticles under APR conditions. Although the particle size is similar for PtMo and PtRe, CO uptake during chemisorption measurements is more than twice as high for PtRe as PtMo per mole of Pt. This would indicate that after reduction of the fresh catalyst, more of the Pt is covered by Mo or MoO_x species as compared to Re or ReO_x species.

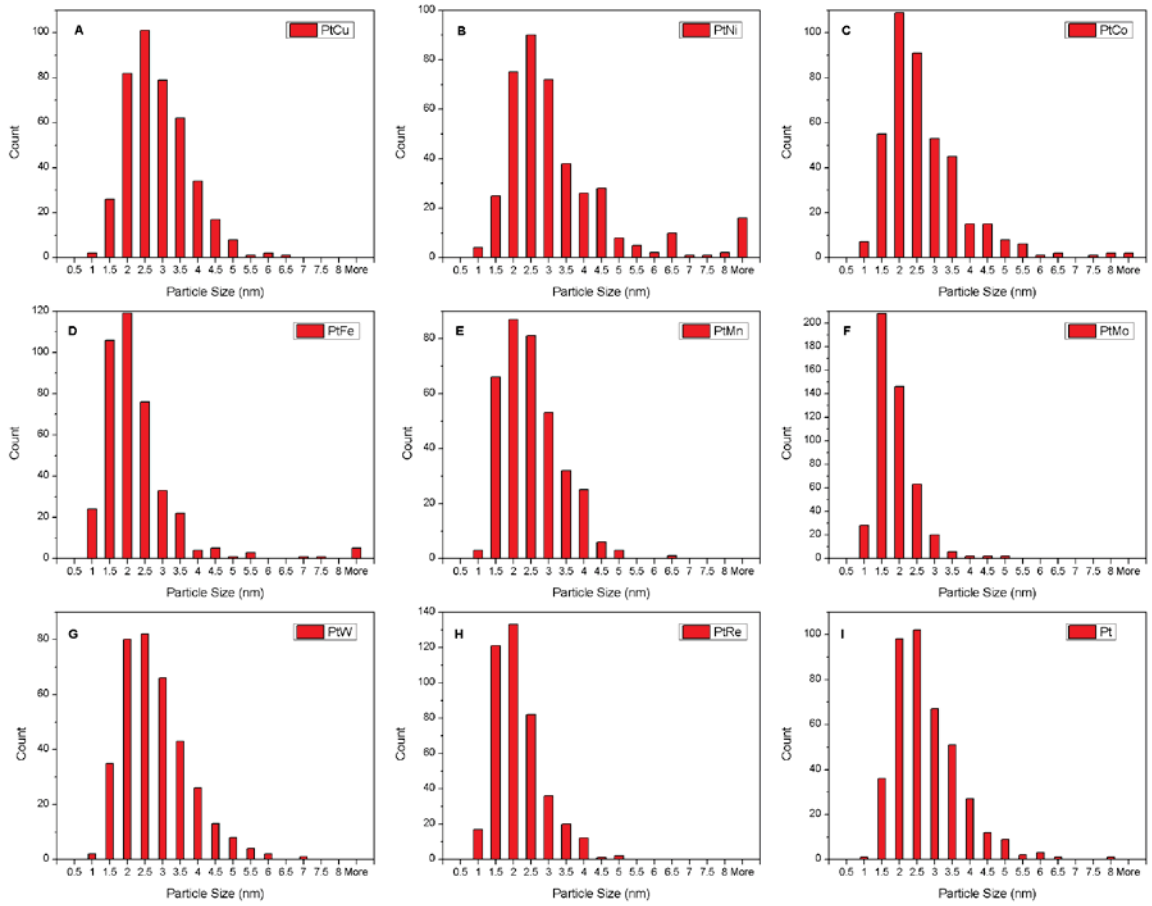

Figure A. 10 Particle size distributions for used catalysts from TEM images.

Table A. 6 Pt dispersion as calculated from CO chemisorption of the fresh reduced catalyst, and average particle size after APR from TEM.

Catalyst	Chemisorption (mol CO/mol Pt)	Number average particle size by TEM (nm)
5% Pt/MWCNT	0.215	
5% Pt, 1.4% Mn/MWCNT	0.164	2.3 ± 0.8
5% Pt, 1.4% Fe/MWCNT	0.109	2.0 ± 1.2
5% Pt, 1.5% Co/MWCNT	0.246	2.5 ± 1.1
5% Pt, 1.5% Ni/MWCNT	0.215	3.1 ± 2.2
5% Pt, 1.6% Cu/MWCNT	0.193	2.6 ± 0.9
5% Pt, 2.5% Mo/MWCNT	0.128	1.6 ± 0.6
5% Pt, 4.7% W/MWCNT	0.181	
5% Pt, 4.8% Re/MWCNT	0.279	1.9 ± 0.7

Appendix B Chapter 3 Supplementary Information

Table B. 1 Water-gas shift kinetics for all catalysts. WGS and methanation TORs were interpolated to 300 °C with standard gas feed composition of 6.8% CO, 21.9% H_2O, 8.5% CO_2, 37.4% H_2 and balance Ar.

			Apparent Reaction Order				WGS	Methanation
Catalyst	E_a (kJ mol^{-1})	Temp (°C)	H_2O	CO_2	CO	H_2	TOR / 10^{-2} s^{-1}	TOR / 10^{-3} s^{-1}
5% Pt/MWCNT	81.6	300	0.76	-0.06	0.12	-0.44	3.2	--
5% Re/MWCNT	110.3	270	0.47	-0.07	0.15	-0.40	2.5	4.8
5% Pt, 4.8% Re/MWCNT	99.6	240	0.87	-0.07	-0.15	-0.48	17.9	--
5% Pt, 4.8% Re/C	109.5	250	0.79	-0.02	-0.21	-0.72	8.8	--

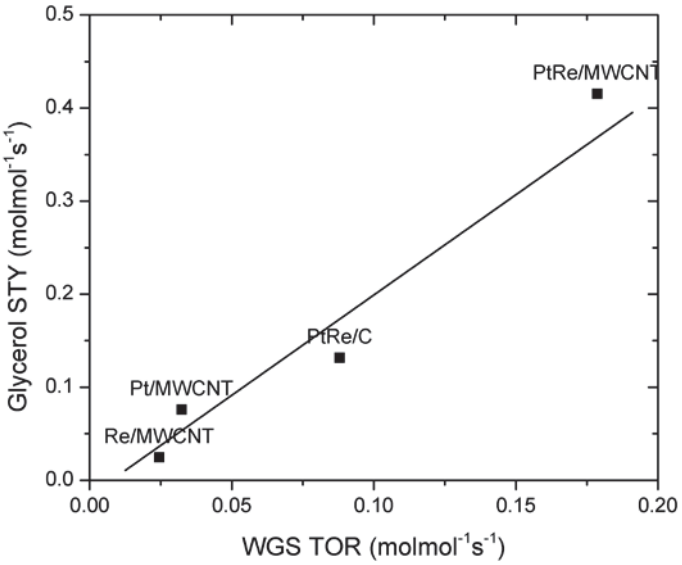

Figure B. 1 Glycerol STY during APR versus WGS TOR. WGS TORs were interpolated to 300 °C with standard gas feed composition of 6.8% CO, 21.9% H_2O, 8.5% CO_2, 37.4% H_2 and balance Ar. Glycerol APR STYs were obtained at 230 °C, 32 bar, 10 wt% glycerol.

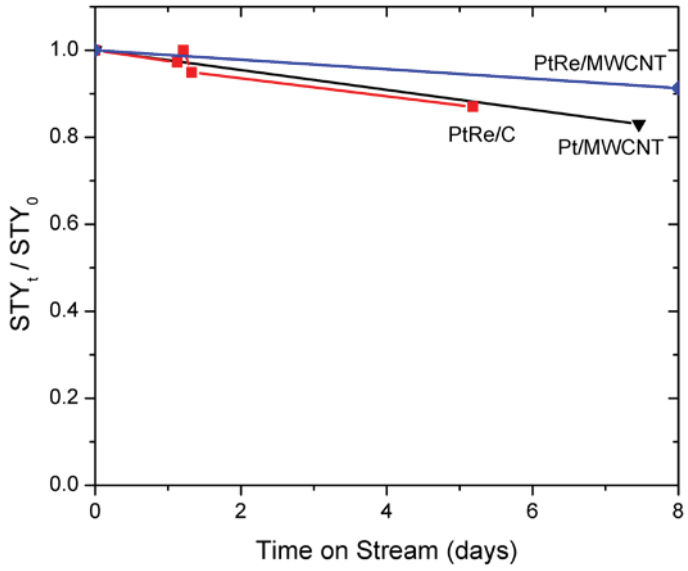

Figure B. 2 Deactivation for each catalyst displayed as a fraction of the initial STY during at least 5 days time-on-stream. Data obtained at 230 °C, 32 bar total pressure, 10 wt% glycerol feed, and 0.30 mL/min liquid flow rate.

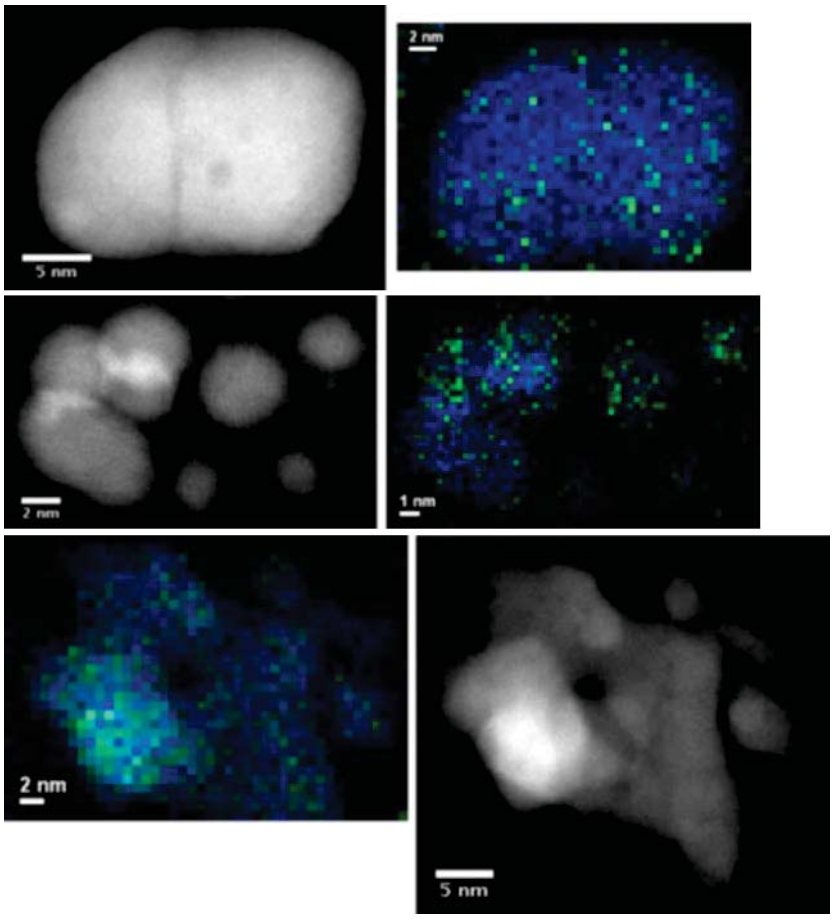

Figure B. 3 Additional STEM-EELS maps elemental maps at the Pt $M_{4,5}$ edges (green) and Re $M_{4,5}$ edges (blue) for nanoparticles on PtRe/MWCNT after glycerol APR for at least 5 days reaction time.

Appendix C Chapter 4 Supplementary Information

Table C. 1 Site time yields for all products measured at low conversion during APR. Data collected at 230 °C, 32 bar total pressure.

Reactant	Glycerol	Propylene Glycol	1,3-Propanediol	1-Propanol
Conversion	1.4%	1.8%	2%	3%
Feed Conv. Rate	3.0	3.7	4.7	3.5
H_2	9.6	6.1	2.4	15
CO	0.03	0.002	0.01	0.04
CO_2	4.0	1.3	2.4	2.4
CH_4	0.1	0.3	0.1	--
C_2H_6	0.04	0.1	1.0	2.8
Acetaldehyde	0.01	0.03	0.02	--
Propionaldehyde	0.001	0.01	0.1	0.5
Acetone	0.01	0.01	--	--
Methanol	0.2	--	0.1	0.2
2-Propanol	0.001	0.01	--	--
Ethanol	0.2	0.3	0.8	--
1-Propanol	0.1	0.05	1.5	Feed
Hydroxyacetone	0.5	2.8	--	--
Acetic Acid	--	--	--	--
Propionic Acid	--	0.03	0.3	0.3
Propylene Glycol	0.4	Feed	--	--
Ethylene Glycol	0.6	--	--	--
1,3-Propanediol	0.02	--	Feed	--

VITA

VITA

Fred G. Sollberger is a graduate of the University of Illinois-Urbana (2010) with a Bachelor's Degree in Chemical Engineering. During his time in college he spent time working a process modeling intern at Archer Daniels Midland researching the scalability of biomass conversion technologies being published in literature, and comparing to in-house generated kinetic data. After beginning the doctorate program at Purdue University under an Andrews Fellowship, Fred became a part of the catalysis research group of Prof. Fabio Ribeiro and Prof. W. Nicholas Delgass, focusing on fundamental catalytic studies of bimetallic catalysts used for reforming biomolecules into hydrogen or useful chemicals. His work included extensive use of x-ray absorption spectroscopy to perform *operando* experiments to study the working state of the catalyst. During his time at Purdue he was able to present his work as a keynote talk at the 2012 AIChE Annual Meeting and at the 23rd North American Meeting (NAM) of the Catalysis Society. Upon completion of the doctorate program, Fred plans to begin work as a Sr. Research Scientist at UOP, LLC in catalysis research.